

Phase Mixing and Separation in 2D Supramolecular Networks.

Alexander Robert Allen

A thesis presented to the University of Nottingham for the
degree of
Doctor of Philosophy

November 2020

Abstract

The study of molecular assemblies through the use of SPM is well documented. This thesis examines assemblies of bi-isonicotinic acid (*formally 4,4-dicarboxy-2,2-bipyridine*), which forms assemblies that appear to be hydrogen bonded. The interesting element inspiring the study of this molecule is its surface-induced chirality, which restricts certain bonding configurations and orientations.

Experiments were conducted under ultra high vacuum. Both STM and NC-AFM imaging of assemblies were made of the bi-isonicotinic acid molecules deposited on Au(111) and Ag(100). These assemblies were studied at room temperature and using cryogenics, specifically liquid nitrogen and liquid helium. Images showed that the molecules formed organised assemblies with hydrogen bonds locked in a fixed direction. Sub molecular resolution images were also obtained of the networks allowing it to be shown that key bonding site of molecules aligned in an organised manner.

The molecules were then modelled through a set of possible tiles with specific permitted bonding geometries. Monte Carlo simulations were then conducted using algorithms inspired by a heat bath algorithm, which gave considerations to simulated molecules and their translations and rotations with suitable probability weightings. The subsequent behaviour of the molecules was then allowed to evolve under different bond strengths, system temperatures and molecular concentrations. Final state lattices were formed showing different molecular configurations that followed predictable behaviours based on input parameters.

Finally, a study is conducted on the output of the molecular simulations investigating the suitability of machine learning in predicting both initial input parameters of a system, and also its ability to categorise final state configurations in both objective and subjective classifications. While results for objective classifications were almost definitively predicted, a correlation was also observed between the subjective classifications, particularly between those that are most similar to each other.

Acknowledgements

For all the progress that has been made in the writing and structuring of this thesis, it has been hard.

It is important that that sentence sit individually because this is my only chance to write anything resembling a preface to any document that I might put my name to in any meaningful sense. I would like to genuinely say to all struggling that no one can predict how a PhD will evolve, and I say this as one who has been really struck by the crisis of COVID-19. For many, there will be set-backs and problems. Academia is very competitive and even the most flawless progression through the experimental, or indeed theoretical, journey are not guaranteed as much as may be due to them. Remember that those who truly value knowledge are those who can make it a force for good in the world. Now to my acknowledgements.

The single most important acknowledgement I need to make is to my supervisor. Phil, you are my supervisor, my mentor in my academic journey, and my friend. This man is a huge presence in the world of academia, one who humbles me and makes me wish to be better at conveying the meaning behind science. I cannot thank you enough for our conversations and for the world you have shown me.

Thank you to the people who helped with the creation of data for this thesis. Abdur Rashid Monhammad and Oliver Gordon, I can't thank you enough for your work to help me

Equally I need to thank all of those who I have worked with in my group. Those who have worked with me and trained me. Thank you Adam, Philipp, Alex, Sam, Jeremy, Morten, and Simon. As well as those that I have worked with in the group. Thank you Filipe, Oli (again), Matt, Ellie, Chris, Joe, and Abby.

Thank you to my family, to whom acknowledgments cannot be directly calculated. My family has gone through hardship, joy and work, which I only intend

to emulate. Mum and Dad, I really want to put you front and foremost in my emotional support category. It's not easy for me to talk but it's incredibly important that you are lauded above many else from my support cycle. My sister must also feature in this because she has come very far. I am not one to proffer emotion very much but she has spent a long time finding her place. I hope that she is almost there in her journey to real success, triumph and happiness. By whatever name, Poppy or Charlie, I hope that this acknowledgement does justice to my thanks, in all the sad brevity it needs to be expressed in.

Thank you to my friends that have helped me. There are many people that matter in my ability to even write this and I'm not going to short-change. So (and I must insist) in no particular order... Danny you're my oldest friend where the friendship is the most deep, loving, and, dare I say, decrepit. Alex you are my treasure, my confidant in tragedy and partner in comedy. Simon you made me believe I could have a go at a PhD (not a barbed comment), you have strengthened by dismissing my tendency for negativity against myself. Francesca, well, we must make bunting together soon over a bottle of something absurd, while chatting the absurd framed as the sensible. Mr. Hayes, while I don't see you as much as I'd like, you have been one of the most fundamental presences of *good* in my life and let's just have a good beer tasting soon! Dan you made this possible through support in turbulence; a sounding-board and a grounding-board, your willingness to really put some time aside for a quick pint or chat has *literally* preserved my sanity. With that: Harry and Max, I hope we get back to quizzing soon. Esme, you're just a real stalwart of strength who has sat by me in wobbles and presented a strong path of achievement that many would envy and wish to follow; your word-count eclipses mine! Julian you've always given fierce opinions and have been a glorious communicator of information; I would have fallen to the pressures of the great-wide world if it weren't for you pulling me out of my insular self. Michael, your belief in people is astounding; you wish the best and truly listen to situations, which makes me truly indebted to you. Please

just answer me a query as I must know what one would be doing if performing litigation against 5 cent coins in America? Tamsin, the sonorous blasts of some rhythm that an ambulance does not regularly display will provide colour to a monochromatic lockdown; you're half Joe Camel and a third Fonzarelli. David, your belief in me is frankly too much; what you did for me in planning a dinner of exceptional circumstance that I would adore, well it shows me how much our trips to Scotland matter... To both of us and you are far too dear.

My undergrad housemates need a mention in their own right. There is no order here but understand my endless affection to all of you. Alex I hope I have managed to affect you positively in our joint-lives; you've excelled me in capacity but if I could have one iota of your wit or charm, I would be a very rich man. Rich/Jimbo you know I have enormous respect for you, you delight in the absurdity of the simple; may we dance one time a simple little interpretive number to Kate Bush or Neil Diamond; we needn't dance literally, in fact I'd prefer we didn't but rather cast angry glances across a room. Dave I don't think you realise how deeply you have affected me; your journey is one that every educator should undertake and you have taken steps that make want to be better as an teacher and you're a damn good person too. You made me reconsider a lot of negative introspection in a very formative period of my life and you still provide advice that is frank and constructive. Nikki, you don't escape this positive rant. You stopped me from falling into traps that make me devalue myself, I vaguely think I can make it.

Emma thank you so much for all the chats and support; I have many highlights of time with you and hope for many more. Ken you have provided levity in our cheese and wine evenings and thank you everything. Likewise, Andy, as my first supervisor and friend, thank you for everything. Will B., sorry we don't speak as much as we should; the moment you asked me to be an usher at your wedding was huge to me and thank you for letting me be a part of that great day. Chris, frankly, your success scares me a little; I am proud that someone I knew

made a real go of it. Hannah you're doing so well; thank you for our chats and I hope you smash it. A final cursory thank you to Gabriel Fauré, your requiem played as I wrote the final sentence; make of that what you will.

“I didn't run today, I ran yesterday, will hopefully run tomorrow”

Andy

Contents

Abstract	i
Acknowledgements	ii
Contents	vi
1 Introduction	1
1.1 Aims and Objectives	2
1.2 Chapter outline	3
2 Scanning Probe Techniques	5
2.1 Structure of the Scanning Probe Unit	5
2.2 Scanning Tunnelling Microscopy	9
2.3 Non-Contact Atomic Force Microscopy	21
2.4 Experimental Systems	28
2.5 Experimental Constraints	31
2.6 Etching Tips	36
2.7 Artefacts	37
2.8 Surface Preparation Techniques	42
3 Additional Theory	45
3.1 Motivation for the Choice of Bi-isonicotinic Acid	45
3.2 Surfaces of Study	55
3.3 Molecules of Study	57

3.4	AFM with a functionalised tip	58
3.5	Monte Carlo Simulations of Molecular Dynamics	59
3.6	Simulated NC-AFM Imaging	64
4	Hydrogen Bonded Molecular Assemblies	67
4.1	Discussion of Hydrogen Bonding in Supramolecular Assemblies . .	67
4.2	STM Imaging of Simple Hydrogen Bonded Assemblies	69
4.3	STM Imaging of Tetracarboxylic Acid Networks	72
4.4	NC-AFM Imaging of Hydrogen Bonded Assemblies	76
5	Supramolecular Assemblies of Bi-isonicotinic Acid	80
5.1	Motivation	80
5.2	Methodology	81
5.3	Network Formation After Deposition	84
5.4	Molecular Constraints After Deposition	87
5.5	The Role of Hydrogen Bonding in Formed Networks	91
5.6	Network Boundaries of Molecular Assemblies	96
5.7	Simulated AFM images	101
5.8	Spectroscopic Imaging of Bi-isonicotinic Acid Assemblies	104
5.9	Conclusion	106
6	Monte Carlo Simulations	108
6.1	Monte Carlo Methods	108
6.2	Tiling Regimes of Simulated Molecules	115
7	Categorisation of Assembly Regimes with Machine Learning	125
7.1	Motivation	125
7.2	Neural Networks Background	126
7.3	Architecture of a Neural Network	129
7.4	Training of a Neural Network	135
7.5	Predicting Input Parameters of Simulations	139

7.6	Categorisation of Simulated Results	143
8	Conclusion	149
Appendices		
Appendix A	Derivations	154
Appendix B	Initial Motivations of Experiments	157
References		165
List of Figures		170

Chapter 1

Introduction

The study of the nanoscale requires one to embrace the quantum nature of reality. Nanoscience forgoes the absolutes of the classical world of physics in favour of one governed by quantum energy potentials, wave-particle duality and a probabilistic interpretation that runs counter to a scientist's instinct to catalogue the minutiae of study.

The field of nanoscience exists to probe the intricacies of the overlap of physics and chemistry. The field, by definition, explores the physics of objects at that nanometre scale, that is, the physics of atoms and molecules and their roles in bonding [1]. Many experimental techniques have been designed to probe this scale, ranging from the intuitively abstract, techniques such as low energy electron diffraction (LEED), to the more visual techniques of microscopy. This thesis is concerned with experiments that involve Scanning Probe Microscopy (henceforth SPM).

SPM takes advantage of quantum effects such as tunnelling and the Pauli exclusion principle, which are not encountered as day-to-day phenomena in the classical regime that typifies the scale that humanity experiences. Nevertheless, advances in both understanding of physics and experimental techniques in the last century have allowed science to better understand the atom and the nature of the chemical bond.

While the details of the experimental techniques are given more thoroughly in Section 2, the development and foundation of them, is useful to consider. The origin of SPM can arguably be considered as the point at which scanning tunnelling microscopy became a practical experimental technique, where Binnig *et al.* demonstrated the application of tunnelling electrons through a vacuum barrier [2, 3]. Additional advancements in atomic imaging took place through the development of the atomic force microscope, again due to the work of Binnig *et al.* [4]

The development of these techniques revolutionised our understanding of the physical world in a way that may not always be truly appreciated. Many progressions in nanoscience predate these inventions. Intricate understanding of the atomic regime has been unpicked and developed since the initial conceptions of quantum physics [5], whether through diffraction experiments, or spectroscopy. These understandings provide a grounded, scientific knowledge of the inner workings of the solids, both in terms of bulk and surface, and of the general chemistry. It is through the development of imaging, however, that a more intuitive exploration of the atomic regime can be taken. Through imaging, aspects of this world can begin to be *seen*, providing further interpretations and evidence that deepens scientific understanding and broadens scientific inquiry.

1.1 Aims and Objectives

The investigation in this thesis is primarily concerned with that of the bi-isonicotinic acid (*formally 4,4-dicarboxy-2,2-bipyridine*) molecule deposited on transition metal surfaces. The objective is to observe its construction of molecular networks formed with its restrictive geometry. In its *trans* conformerisation, the molecule has a degree of rotational symmetry but no axis reflective symmetry. The driving orientations are to be explored along with the potential forces that govern them.

An analysis is made into the simulation of the formation of networks using Monte Carlo methods. An objective is to model the bi-isonicotinic acid molecule through a set of tiles to be moved throughout a network.

A final objective is to create a machine learning environment that sets out to predict factors that govern the evolution of final arrangements of molecular network given simply information only on the final state. It is also to be investigated whether a similar network has the ability to classify final state networks based on human-defined categories.

1.2 Chapter outline

Chapter 2 of this thesis is an explanation of the equipment used to conduct the experiments with explanations of the scientific principles involved. This is presented alongside the specific equipment and the experimental techniques.

Chapter 3 presents additional theory pertaining to the inspiration behind the experiments conducted along with the further theory behind the molecules and surfaces of study. It also presents the theory behind Monte Carlo simulations to provide a basis on which simulated models were developed.

Chapter 4 explores the theory behind the hydrogen bond as well as its relevance to the studied molecular assemblies. Examples of relevant, hydrogen bonded networks are presented as well as a brief analysis of the possible imaging of hydrogen bonds within molecular networks.

Chapter 5 presents the results of molecular assemblies, particularly a study on the deposition of the bi-isonicotinic acid molecule and the assemblies that it forms. Both scanning tunneling microscopy and atomic force microscopy are used to understand the arrangements of the molecules in their networks and present sub-molecular resolution examples of these network. Spectroscopic data of the molecules were also collected in order to further understand bonding that structures the molecules.

Chapter 6 presents the results of conducted Monte Carlo simulations. The chapter focuses on the modification of the existing models to better represent the bonding geometry of molecules as well as permitted and forbidden bonding due to the specific molecular symmetries.

Chapter 7 takes the results of the Monte Carlo simulations and explores the potential of machine learning in the recognition of attributes of molecular assemblies such as its ability to predict system parameters such as temperature and concentration. It also explores the potential for machine learning to categorise assemblies based on human defined classifications.

Chapter 2

Scanning Probe Techniques

This chapter is concerned with the explanation of the equipment and methodology involved with experiments that were conducted. A number of experimental tools and techniques were used.

2.1 Structure of the Scanning Probe Unit

The first technical area to be covered is that of the scanning probe unit itself as its structure and utilisation is the foundation of all experiments. Before discussing the more specialised physics involved with experimental techniques, the control unit and scanning principles of the scanning probe microscope will be examined.

All experimental results produced in this thesis utilised SPM units that functioned with a piezoelectric tube scanner. The operation of this unit is both simple and elegant. Piezoelectric material responds to an applied voltage by elongating in one axis and contracting in another, as shown in Figure 2.1.

A piezoelectric material can then be constructed in the shape of a tube, as shown in Figure 2.2a. This image shows a cross section of a cylinder of piezoelectric material with four electrodes attached, dividing the tube into quadrants or sectors labelled x , \bar{x} , y , and \bar{y} . If a bias voltage is applied to all four electrodes, the whole tube will either elongate or contract, depending on whether the bias is

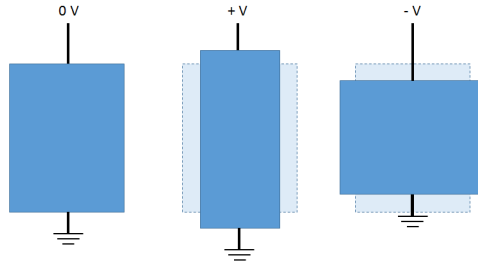


Figure 2.1: An illustration of a piezoelectric material and its specific deformation under an applied bias voltage.

positive or negative. This allows for fine control on approach in the z direction. Control of the tube in the plane parallel to the surface can be achieved by applying voltages to individual sectors of the tube, for example, applying a voltage to the x sector while applying a voltage of the opposite polarity in the \bar{x} sector will cause the tube to move in the x axis. Figure 2.2b shows an example of the response of the tube in the x and z directions.

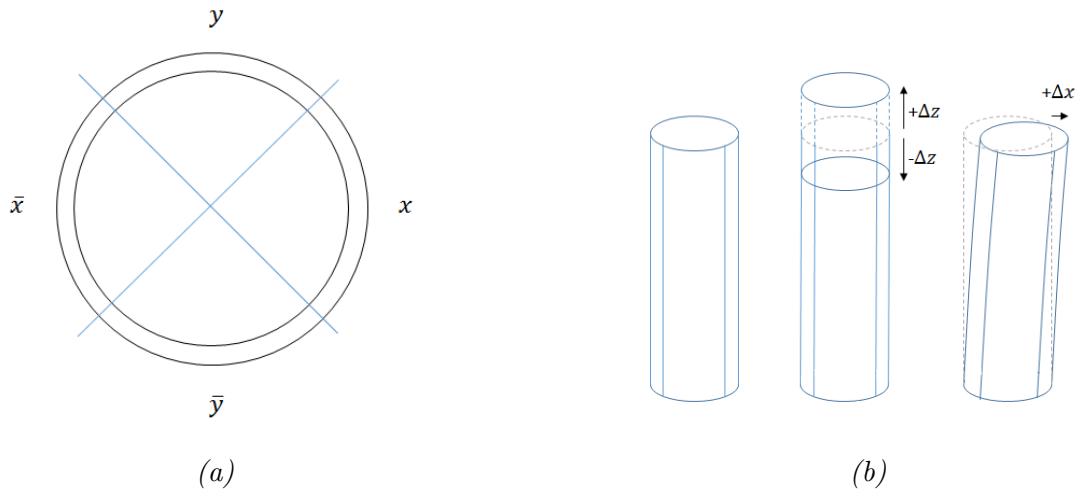


Figure 2.2: The schematic design of a tube scanning unit. (a) Shows cross-section of the unit with its labelled sectors. (b) Shows the use of an applied bias to manipulate the shape of the tube in order to control imaging.

Before discussing the control of a scanning unit, a convention must be established. Henceforth, the Cartesian coordinates (x , y , and z) will be defined so that x and y exist in the plane of the sample, whereas z refers to the axis of approach toward (or retraction from) the sample.

In order to manipulate the tube scanning unit, different biases can be applied to the four quarters of the tube. Δz motion, as illustrated in Figure 2.2b, is achieved by applying an equal bias voltage to all four quadrants, causing the length of the tube to extend or contract proportional to the bias. Lateral motion, that is motion in the x-y plane, is achieved by applying opposite bias voltages to opposite sectors. To achieve the Δx motion shown in Figure 2.2b, a negative bias is applied to the piezoelectric tube in the sector labelled x , and a positive bias in the sector labelled \bar{x} . The application of bias voltages of opposite polarisation will cause the tube to bend toward the desired direction. Under the best conditions, the values of Δx , Δy , and Δz can be of the order of picometres and this allows for control of scanning in the nano-regime.

With this ability to distort the tube, the imaging of a surface can be conducted. A scanning probe is attached to the piezoelectric tube. The probe itself is in the form of a tip, which ideally terminates with a single atom or molecule at its apex. This allows for incredibly localised interactions between the tip and sample to be interpreted as images which reveal the topography and electronic structure of the surface in study. The techniques and the role of probe in the scanning process will be further discussed in Sections 2.2 and 2.3.

In order to produce an image of a surface on this scale, data relating to the tip-sample separation is taken at a single point above the surface. The tip is then scanned back and forth across the surface and data above every point is recorded. A line of data points allows for a continuous view of changes in surface features and by compiling multiple single line scans, a three dimensional image of a surface can be inferred from scan data. Additionally, this leads to two scan directions, fast and slow, as shown in Figure 2.3. An understanding of the

scanning procedure is important to further understand the presence of artifacts within scans such as thermal drift and piezoelectric creep, which can obfuscate experimental data.

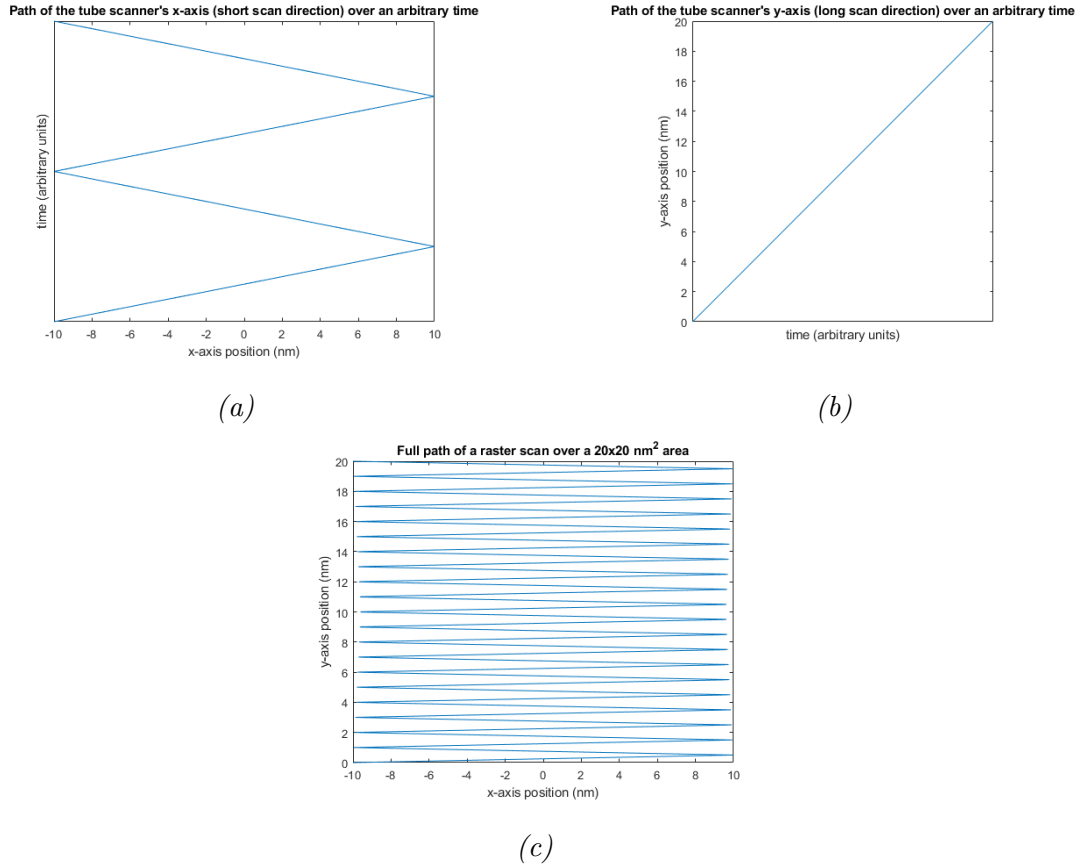


Figure 2.3: Three graphs showing the path of a hypothetical tip in a given scan direction. (a) Shows the fast scan direction and the progression back and forth over time. (b) Shows the same idea in the slow scan direction. These graphs are placed together for contrast. (c) Shows the progression of the tip over a hypothetical area, showing the path taken by the tip.

The piezoelectric tube allows for fine control of the tip with respect to the sample. For coarse control, that is, approaching or retracting the tip on a visible scale, the tube itself needs to be moved within the scan head. The most straightforward mechanism used was the use of slip-stick motors, which apply

slow motion in one direction and then quick motion in the opposite. This causes the tube to move along a defined track. This motion is also utilised in the Besocke design of the STM scan head used throughout the experiments detailed in this thesis.

Besocke design

The Besocke design [6–8] employs a central piezoelectric tube that holds the tip and is used for scanning. This tube is attached to a plate that contains a sloped surface. Three further tubes rest on a base plate spaced equally with 120° separation, as shown in Figure 2.4. These additional tubes function as supports for the stage. Each of the supports is attached to a glass or sapphire ball, which supports the plate above. A sawtooth voltage wave form is applied to each support. This has the effect of causing the plate held by the supports to move slowly in one direction and quickly in the opposite direction, resulting in a slip-stick effect that allows the entire stage to translate or rotate. The tip-to-sample approach is achieved by rotating the stage. The plate to which the tip is attached is a helical ramp [7]. Thus, the tip can be lowered or raised with respect to the sample by rotating the helical plate that rests on top.

2.2 Scanning Tunnelling Microscopy

The basic operating principle of scanning tunnelling microscopy (henceforth STM) involves bringing a conducting tip into close proximity with a conducting surface. In order to take an image of a surface the tip should preferably terminate with a single atom. This is because STM produces an image based on the electronic configuration of both the surface and the tip, further explained in Section 2.2.2. The termination of the tip by a single atom means that any tunnel current recorded will be dominated by the interactions between a single atom and the surface. Importantly, this means that any data extracted, typically

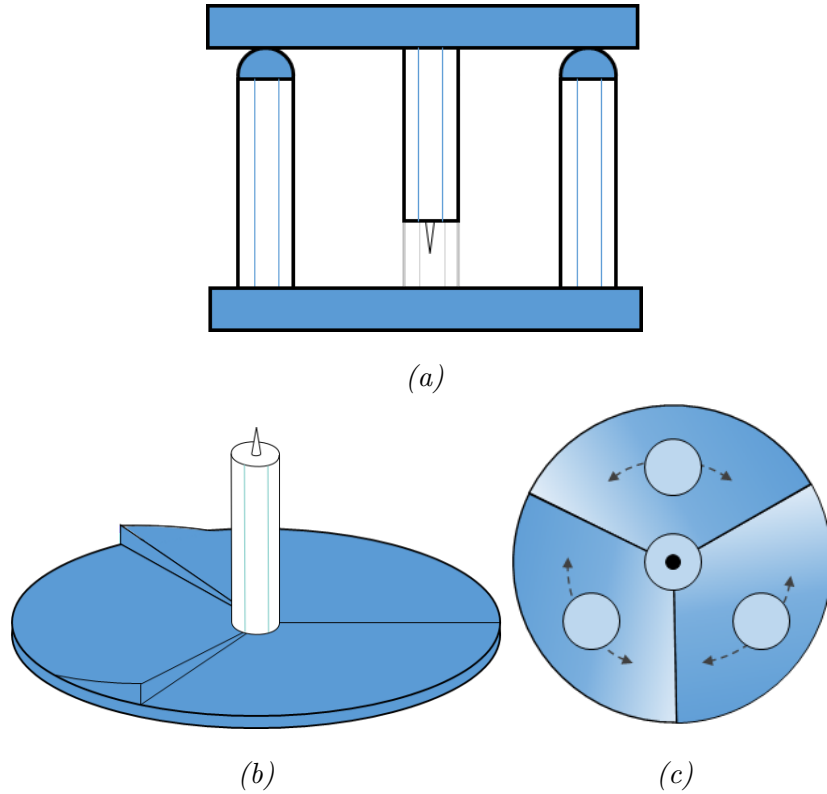


Figure 2.4: A schematic of the Besocke microscope design. (a) A side view of the tripod. The tip extends down from the upper plate and can be approached to the sample in the middle. (b) Shows the design of the plate, to which the tip is attached. The supported plate also shows the helical ramps in each sector to allow the tip to be approached or retracted with respect to the sample. (c) Shows a plan view of the Besocke design, highlighting the motion of the legs

viewed as a convolution between the electronic structure of the surface and the tip, will be highly localised and therefore allow for maximum spatial resolution of the imaged surface.

2.2.1 1-Dimensional Tunnelling

Figure 2.5 shows a one dimensional potential barrier that arises between a tip and sample with the wave function of a single electron tunnelling through the po-

tential barrier. The wave function is determined by solving the time independent Schrödinger equation:

$$\left(-\frac{\hbar^2}{2m} \frac{d^2}{dz^2} + V\right) \psi = E\psi, \quad (2.1)$$

where V represents the potential energy and E represents the energy of a given electron, m is the mass of the electron and ψ is the wave function of the electron. Inside the barrier, the potential energy is taken as the vacuum energy, then Equation 2.1 can be rearranged:

$$\frac{d\psi^2}{dz^2} = \frac{2m}{\hbar^2} (E_{vac} - E) \psi. \quad (2.2)$$

Inside the barrier, where $E_{vac} > E$ the solution to the equation is:

$$\psi = Ce^{\kappa z} + De^{-\kappa z}, \quad (2.3)$$

where C and D are unknown constants and

$$\kappa = \sqrt{\frac{2m}{\hbar^2} (E_{vac} - E)}. \quad (2.4)$$

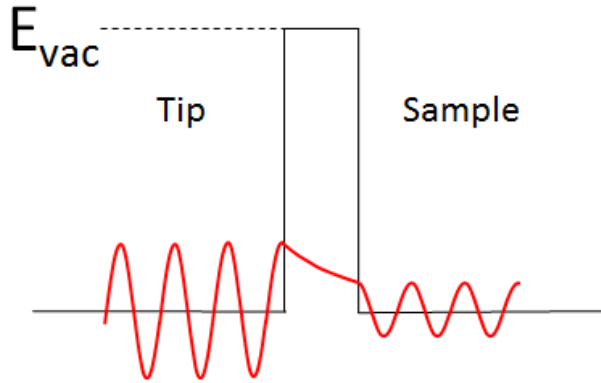


Figure 2.5: A one dimensional analogue of the potential barrier of a vacuum, E_{vac} , separating a sample and tip. The red line represents the wave function of an electron incident from the left tunnelling from the tip to the sample.

Inside the barrier $\kappa^2 > 0$, leading to an exponentially shaped wave function. Outside of the barrier:

$$\kappa = \sqrt{\frac{2m}{\hbar^2} (-E)}, \quad (2.5)$$

leading to a sinusoidal behaviour.

The general solution given corresponds to the tunnelling of an electron in either direction of the potential barrier. For the case of an electron incident from the left, displayed in Figure 2.5, and defining the direction of z increasing is to the right, the equation can be further simplified to:

$$\psi = De^{-\kappa z}. \quad (2.6)$$

Thus the tunnelling probability can be given by squaring the wave function:

$$|\psi|^2 = D^2 e^{-2\kappa z}. \quad (2.7)$$

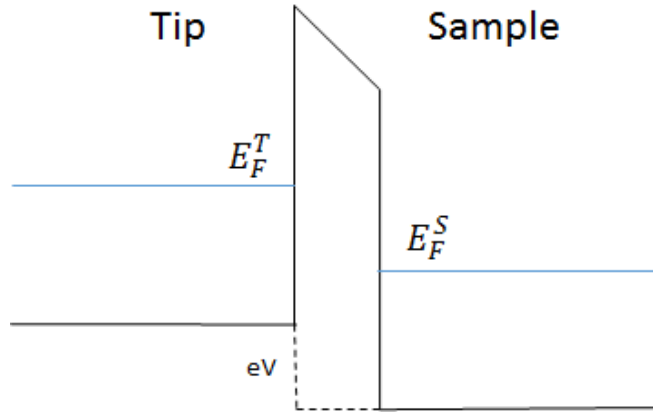


Figure 2.6: An illustration of the different energy levels that result from the application of a bias voltage between the tip and the sample. E_F^T is the Fermi level of the tip and E_F^S is the Fermi level of the sample.

By applying a bias voltage as shown in Figure 2.6, a preferred direction of flow of electrons is specified and thus, a current can be measured. The current

will be a function of the transmission probability of a tunnelling electron, given in Equation 2.6 [9]:

$$I_t \propto e^{-2\kappa z}, \quad (2.8)$$

where I_t is the current due to electrons tunnelling.

Equation 2.8 shows a relationship between the tip-sample separation and the related tunnel current measured between the tip and sample. A value of κ can be determined by examining Equation 2.4. $(E_{vac} - E)$ represents the energy required to liberate an electron from a surface to free space, that is, the work function of the material. Most materials have a work function of between 4 – 6 eV [10] and this can be substituted into Equation 2.4 to determine $\kappa \sim 1\text{\AA}^{-1}$ [9]. This means that the measured current between tip and sample will differ by roughly a factor of e^2 for every change of an angstrom in separation.

2.2.2 More Advanced Approaches to STM

While the one dimensional barrier approach is a good starting approximation, it is obviously a very limited model. To better understand the science of STM, a more physically rigorous model should be considered.

The Bardeen Approach

J. Bardeen is responsible for introducing the tunnelling model used for the standard interpretation of STM imaging [11]. The model considers an electron tunnelling from the sample to the tip and considers the time-independent Schrödinger equation for the wave function of an electron at both the sample and the tip:

$$\begin{aligned} \hat{\mathcal{H}}_S \psi_S &= (\hat{T} + \hat{U}_S) \psi_S = \epsilon_S \psi_S & \text{— Sample} \\ \hat{\mathcal{H}}_T \psi_T &= (\hat{T} + \hat{U}_T) \psi_T = \epsilon_T \psi_T & \text{— Tip,} \end{aligned}$$

here \hat{T} is a kinetic energy operator and \hat{U}_S and \hat{U}_T are the potential energy operators of the sample and tip respectively. Thus a Hamiltonian operator can be constructed:

$$\hat{\mathcal{H}} = \left(\hat{T} + \hat{U}_S + \hat{U}_T \right). \quad (2.9)$$

It is also considered that ψ_S^μ and ψ_T^ν are the eigenfunction wave functions of the sample and tip respectively.

To then consider the tunnelling of an electron from the sample to the tip, the probability can be extracted from the overlap of the time-dependent wave function of the sample with the tip wave function. The time dependent Schrödinger equation is:

$$i\hbar \frac{\partial}{\partial t} |\psi(t)\rangle = \hat{\mathcal{H}} |\psi(t)\rangle. \quad (2.10)$$

This equation can be multiplied from the left with the wave function of the tip and solving Equation 2.10 for the tip state, the following is given:

$$\begin{aligned} \langle \psi_T^\nu | \left(i\hbar \frac{\partial}{\partial t} |\psi(t)\rangle \right) &= \langle \psi_T^\nu | \hat{\mathcal{H}} |\psi\rangle - \langle \psi_T^\nu | \hat{\mathcal{H}}_T |\psi\rangle \\ i\hbar \frac{\partial}{\partial t} \langle \psi_T^\nu | \psi \rangle &= \langle \psi_T^\nu | \hat{\mathcal{H}}_S |\psi\rangle. \end{aligned} \quad (2.11)$$

The model can be critiqued due to the theory requiring the two states to be orthonormal; this is not strictly the case. The approximation is sufficiently applicable, however, in situations when the tip-sample overlap is small [12, 13]. Equally, the use of perturbation theory is appropriate due to the fact that the sample potential U_S is taken to be only weakly modified in the presence of the tip.

Solving the theory with these approximations leads to a tunnelling probability:

$$P_{\mu\nu}^{ST} = \frac{2\pi}{\hbar} \delta(\epsilon_\nu - \epsilon_\mu) |M_{\mu\nu}^{ST}|^2, \quad (2.12)$$

where $P_{\mu\nu}^{ST}$ represents the tunnelling probability per time interval, the $\delta(\epsilon_\nu - \epsilon_\mu)$ is simply the Kronecker delta function guaranteeing an elastic tunnelling event, and $M_{\mu\nu}^{ST}$ is the stationary-state matrix element of the potential:

$$M_{\mu\nu}^{ST} = \langle \Psi_T^\nu | U_S | \Psi_S^\mu \rangle. \quad (2.13)$$

It can be shown that this matrix element can be written in the form:

$$M_{\mu\nu}^{ST} = -\frac{\hbar^2}{2m} \int_{\text{sample}} \{ \Psi_S^\mu(\mathbf{r}) \nabla^2 \Psi_T^\nu(\mathbf{r})^* - \Psi_T^\nu(\mathbf{r})^* \nabla^2 \Psi_S^\mu(\mathbf{r}) \} dV. \quad (2.14)$$

Necessarily, the probability of tunnel current given in Equation 2.12 needs to be modified to incorporate the voltage bias that is applied, for example, to the tip relative to the sample:

$$P_{\mu\nu}^{ST} = \frac{2\pi}{\hbar} \delta(\epsilon_\nu^T + eV - \epsilon_\mu^S) |M_{\mu\nu}^{ST}|^2, \quad (2.15)$$

where e is the elementary unit of charge and V is the applied bias voltage. Using this, the ultimate expression of the tunnel current can be produced by considering this modified probability. The expression for tunnel current needs to sum all possible states of tunnelling events from the tip into the sample but equally those that occur in the opposite direction, that is,

$$I = I^{T \rightarrow S} - I^{S \rightarrow T}. \quad (2.16)$$

The tunnelling probability, without bias, should be assumed to be symmetric whether from sample to tip or vice versa. From first-order perturbation theory, the current can be expressed [9]:

$$I = \frac{2\pi e}{\hbar} \sum_{\mu, \nu} \{ f(\epsilon_\nu)[1 - f(\epsilon_\mu)] - f(\epsilon_\mu)[1 - f(\epsilon_\nu)] \} |M_{\mu\nu}^{ST}|^2 \delta(\epsilon_\nu + eV - \epsilon_\mu), \quad (2.17)$$

where $f(\epsilon)$ is the Fermi distribution function. This can then be condensed using the equations above:

$$I = 2e \sum_{\mu, \nu} (f(\epsilon_\nu) - f(\epsilon_\mu)) P_{\mu\nu}^{ST}. \quad (2.18)$$

The Tersoff-Harmann Approach

The Tersoff-Harmann approach aims to calculate the matrix element, that is $|M_{\mu\nu}^{ST}|^2$, from Bardeen's approach [14]. Some assumptions need to be made. Firstly, there is an assumption of an atomically sharp tip and that the electronic wave function of the outermost atom is an s-state. Furthermore, as the wave function decays exponentially into the vacuum, only the orbitals of the outermost tip atom are considered important for tunnelling.

The model begins with a modification of the tip wave function that is not set in one dimension. The modified wave function has the following form:

$$\psi_{\nu}^T(\mathbf{r} - \mathbf{r}_0) = \frac{C}{\kappa_{\nu}|\mathbf{r} - \mathbf{r}_0|} e^{-\kappa_{\nu}|\mathbf{r} - \mathbf{r}_0|}. \quad (2.19)$$

It should also be noted that for the model's assumption, the sample wave function should also be a solution in the region of the tip. Thus, the decay constant to be considered, κ , can be assumed to be:

$$\kappa_{\nu} = \kappa_{\mu} = \kappa. \quad (2.20)$$

Using Green's theorem, the expression for $M_{\mu\nu}^{ST}$ can be modified:

$$M_{\mu\nu}^{ST} = -\frac{\hbar^2}{2m} \int_{\text{tip}} \{ \Psi_T^{\nu}(\mathbf{r})^* \nabla^2 \Psi_S^{\mu}(\mathbf{r}) - \Psi_S^{\mu}(\mathbf{r}) \nabla^2 \Psi_T^{\nu}(\mathbf{r})^* \} dV. \quad (2.21)$$

It can then be shown that through substitution into Equation 2.18 and modifying the sum of energy eigenstates in that equation for an integral over all energy, the following is obtained:

$$I \propto \int_{-\infty}^{\infty} (f(\epsilon) - f(\epsilon + eV)) n_T(\epsilon + eV) n_S(\epsilon, \mathbf{r}_0) d\epsilon. \quad (2.22)$$

. If a consideration is taken over energy states relevant for experimentation. The limits of the integral can be narrowed, that is:

$$I \propto \int_{\epsilon_F}^{\epsilon_F + V} (f(\epsilon) - f(\epsilon + eV)) n_T(\epsilon + eV) n_S(\epsilon, \mathbf{r}_0) d\epsilon. \quad (2.23)$$

Here ϵ_F is the Fermi energy, V is the bias voltage, n_T denotes the density of states of the tip, which is modelled as constant, though in practical terms, this only applies for an ideal tip. Variations in tip structures will be discussed in Section 2.7. n_S denotes the local density of states (henceforth LDOS) of the sample, that is:

$$n_S(\epsilon, \mathbf{r}_0) = \sum_{\mu} |\Psi_{\mu}^S(\mathbf{r}_0)|^2 \delta(\epsilon - \epsilon_{\mu}). \quad (2.24)$$

The conclusion to be drawn from this interpretation is that the imaged quantity, in an ideal experimental set-up, is a map of the local density of states of the sample. This more detailed analysis is subject to some limitations, primarily that the approximation is limited to small voltages. High voltages create different decay constants for the vacuum wave function of the tip and sample and this leads to a breakdown of Equation 2.20. Nevertheless, for biases in the millivolt range, those suitable for obtaining atomic resolution on metallic surfaces, the model holds. Therefore the tunnel current is proportional to the density of states of the sample rather than just a simple topographical map. Figure 2.7 (adapted from [15]) shows scan of Cu(111) taken at a low voltage ($V = 100\text{mV}$), with atomic resolution.

2.2.3 Scanning Modes

There are two primary modes of scanning with an STM, which involve either a constant current or constant height scan. A feedback loop is utilised to maintain a relationship between current and tip-sample separation. As the current is a function of the separation a feedback loop allows the STM to control itself by increasing the tip-sample separation if the current increases and decreasing the separation if the current decreases.

Keeping a constant current was the default option for the experiments conducted for this thesis. In order to image, a set point current was specified to the feedback loop. The tip, when scanned, would aim to preserve this current

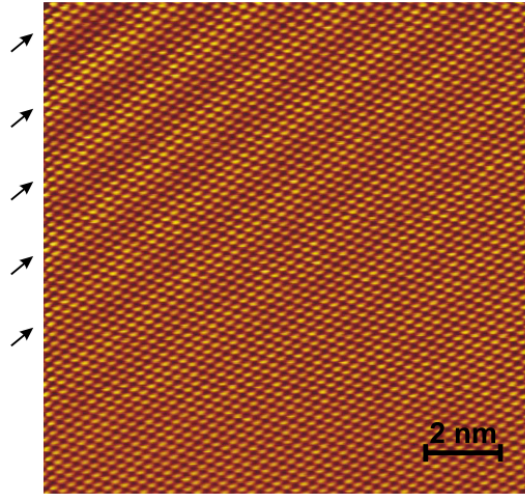


Figure 2.7: An image of low voltage atomic resolution scan of a metal, adapted from [15] along with its caption:

STM image (raw data) of Cu(111) ($I = 50 \text{ pA}$, $V = +100\text{mV}$, $T = 5\text{K}$, scan speed of 13 nm/s , image size: $13 \times 13 \text{ nm}^2$). An electronic surface charge wave, caused by a step edge located just outside the scanned area next to the upper left corner, runs diagonally from upper left to lower right. The arrows on the left indicate the position and orientation of the individual wave fronts. [15]

by making alterations to the height above the surface. This height was then recorded and a three dimensional scan could be produced by creating a composite of the height above all points scanned. A constant height scan is produced by first applying this control relationship to specify a reasonable relationship between tip-sample separation and the tunnel current. Once this relationship is established, the feedback loop is disabled. The tip is then kept at the specified height as changes in current due to the topography or conductance of the surface are then recorded.

2.2.4 Scanning Tunneling Spectroscopy

Although STM imaging is a valuable tool for studying the nanoscale, it is by no means the only technique afforded by STM. Equation 2.22 can be reinterpreted through a differentiation with respect to energy, that is:

$$\frac{dI}{dV} \propto n_S(\epsilon, \mathbf{r}_0). \quad (2.25)$$

It can be seen then that while all states located from E_F to $E_F + V_T$ contribute to the current, the differential of the current with respect to voltage, dI/dV , shows the states at the corresponding energy. This relationship reveals information of surfaces and molecules deposited on them. Energy levels of molecules will include the highest occupied molecular orbital (henceforth HOMO) and the lowest unoccupied molecular orbital (henceforth LUMO). Understanding of molecules can then be interpreted from examining different bias voltages. [16]

Experiments in this thesis specifically involve dI/dV spectroscopy. The method of this is to hold the tip-sample separation constant and altering the bias voltage between the two. The current is then recorded as the bias is swept and the current-voltage relationship can then be graphed. The derivative of this graph is a measure of the LDOS of both the sample and the tip at different bias voltages.

While it is possible to take the derivative of the $I(V)$ curve numerically, it is more prudent to do so through the use of a lock-in amplifier. A lock-in amplifier is used to extract a signal from a noisy environment. It does so by adding a small varying voltage with a known frequency and a small amplitude ($\sim 10\text{mV}$) to the tip-sample bias. Thus, the measured current also contains the modulation. Consider the two signals, V_{ref} , an internal reference signal, and V_{out} , the response signal. These are defined as follows:

$$V_{\text{ref}} = A_r \sin(\omega_r t + \theta_r) \quad (2.26)$$

$$V_{\text{out}} = A_o \sin(\omega_o t + \theta_o) \quad (2.27)$$

The lock-in amplifier takes the measured signal and multiplies it with a sinusoidal reference signal at the modulation frequency:

$$V = A_r A_o \sin(\omega_r t + \theta_r) \sin(\omega_o t + \theta_o), \quad (2.28)$$

which can be rewritten:

$$V = \underbrace{\frac{A_r A_o}{2} \cos(\omega_1 t + \theta_1)}_{\text{Low Frequency}} + \underbrace{\frac{A_r A_o}{2} \cos(\omega_2 t + \theta_2)}_{\text{High Frequency}}, \quad (2.29)$$

where $\omega_1 = \omega_r - \omega_o$, $\omega_2 = \omega_r + \omega_o$, $\theta_1 = \theta_r - \theta_o$, and $\theta_2 = \theta_r + \theta_o$.

Equation 2.29 highlights the modified signal V can be considered the sum of two cosine waves, the first using the difference of the two input frequencies and the second the sum of the two. The signal V is then passed through a low pass filter thereby leaving only the low frequency term:

$$V_{\text{filtered}} = \frac{A_r A_o}{2} \cos(\omega_1 t + \theta_1). \quad (2.30)$$

This is further simplified in the case that, $\omega_1 = 0$, as it is when the reference signal and the response signal are of the same frequency:

$$V_{\text{filtered}} = \frac{A_r A_o}{2} \cos(\theta_1), \quad (2.31)$$

which is a D.C. signal proportional to the amplitude of the input signal.

The phase of the signal can be determined by the lock-in amplifier and the spectrum can be taken by sweeping the voltage, as discussed, noting that the time taken to acquire data at each bias point must be greater than the time interval of integration set on the amplifier.

It should be noted that the dI/dV spectrum acquired will be of arbitrary scaling and while the signal measured is detected in volts, the only meaningful information to be taken is the position of features in the spectrum and the relative sizes of these features.

2.3 Non-Contact Atomic Force Microscopy

As with STM, atomic force microscopy (henceforth AFM), requires the approach of a probe into close proximity with a surface. AFM relies on important forces present at the nanometre scale including the van der Waals force, electrostatic and magnetic forces, and the repulsive effect of the Pauli exclusion principle [1]. The mechanisms of AFM require an understanding of the large range of contributing forces arising between the tip and sample. In STM, small deviations in the separation of the tip and sample has a large change in the measured tunnel current. In AFM, however, the relevant distances can range from hundreds of nanometres, in the case of electromagnetic contributions, to short range chemical forces that are a fraction of a nanometre [1].

Long range electrostatic forces that will exist between a spherical tip, of radius R , and surface can be modelled [1]:

$$F = -\frac{\pi\varepsilon_0RU^2}{z}, \quad (2.32)$$

where ε_0 is the permittivity of free space, z is the tip-sample separation, and U is the potential between the sample and tip. For short-range chemical forces, models such as the Lennard-Jones potential or Morse potential can be considered.

The Lennard-Jones potential, V_{LJ} is given by:

$$V_{LJ} = E_0 \left[\left(\frac{r_0}{r}\right)^{12} - 2 \left(\frac{r_0}{r}\right)^6 \right], \quad (2.33)$$

where E_0 is the depth of the potential well due to the combination of forces, r is the separation of particles and r_0 is the equilibrium position due to the shape of the potential well. The equation shows the combination of short range attractive and repulsive forces. The r^{-12} term is a representation of the repulsive Pauli exclusion principle and the r^{-6} term refers to short range attractive forces such as van der Waals interactions. The shape of the potential well leads to two regimes, an attractive regime, where the separation of two particles is greater than the equilibrium position, and a repulsive regime, where the separation is

less than the equilibrium position. The Lennard-Jones potential is shown in Figure 2.8.

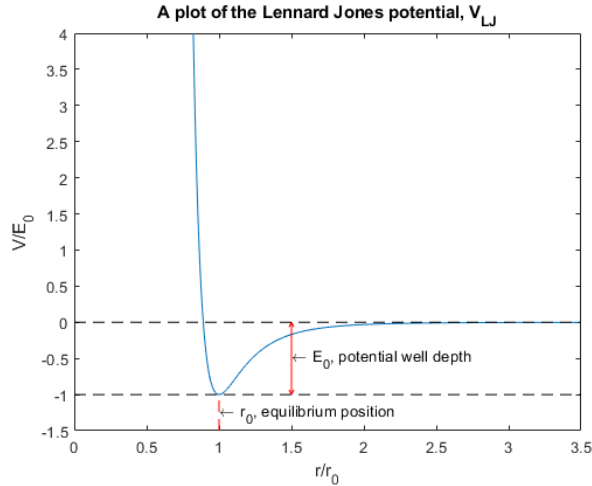


Figure 2.8: A plot of the Lennard-Jones potential showing the potential well, depth E_0 , set at equilibrium position, r_0 .

The Morse potential model is analogous to that of the Lennard-Jones potential. It is modelled with the equation:

$$V = -E_0 \left[2e^{-a(r-r_0)} - e^{-2a(r-r_0)} \right], \quad (2.34)$$

where E_0 , r , and r_0 are once again the depth of the potential well, the separation, and the equilibrium position respectively, and a represents the decay length.

The short range models can both be examined at very small distances away from the equilibrium separation and this allows for a simplification via a Taylor series expansion of both in the same way, that is:

$$V = Cr^2 - E_0 + \mathcal{O}((r - r_0)^3), \quad (2.35)$$

where C is simply a constant of proportionality and r is, as ever, a separation. Thus both potentials at very small distances from the equilibrium separation can be modelled as potential that behaves with the square of the separation. This

means that for small variations around the equilibrium tip-sample separation, the potential can be considered as equivalent to that of a simple harmonic oscillator.

Whereas STM requires the use of a conductive surface, AFM merely requires a sufficiently low level of roughness of the imaged sample. As with STM, it is required that the tip is atomically sharp. The use of AFM then requires that the tip is mounted on the end of a microscopic cantilever, capable of oscillation. In non-contact AFM (henceforth NC-AFM), the cantilever undergoes a driven simple harmonic motion, whose motion is altered due to the microscopic forces modelled by the discussed potentials.

The combination of forces in a driven simple harmonic oscillator can be written as follows:

$$F_{\text{net}} = F_{\text{driving}} - F_{\text{spring}} - F_{\text{damping}} \quad (2.36)$$

and can be expressed more quantitatively as a second order differential equation:

$$m \frac{d^2 z}{dt^2} + b \frac{dz}{dt} + kz = F(t), \quad (2.37)$$

where z is the tip-sample separation, t is time, m is the mass of the oscillator, b is the damping coefficient, k is the effective spring constant of the cantilever and $F(t)$ represents a driving force as a function of time, a constant oscillation of the form $F(t) = F_0 e^{i\omega t}$, with F_0 representing a constant magnitude of force, ω representing the frequency of the driving force, and i is the imaginary unit. The solution of this differential equation is the routine solution of an ordinary second order differential equation. The full derivation is given in Appendix A. The relevant solution of the equation is the steady state of a driven case:

$$z = A e^{i(\omega t + \phi)}, \quad (2.38)$$

where ϕ is an unknown phase, and A is the amplitude of oscillation and which, when substituted into the original differential equation, leads to the definition of the amplitude, A , being defined as:

$$A = \frac{F_0/m}{((\omega_0^2 - \omega^2) + \frac{b}{m}i\omega)}, \quad (2.39)$$

where ω_0 represents the natural oscillation frequency of the system. In order to find the magnitude of the oscillation amplitude, the standard method is used:

$$|A| = \sqrt{AA^*} \quad (2.40)$$

$$|A| = \frac{F_0/m}{\sqrt{\left((\omega_0^2 - \omega^2)^2 + \left(\frac{b^2}{m^2}\omega^2\right)\right)}} \quad (2.41)$$

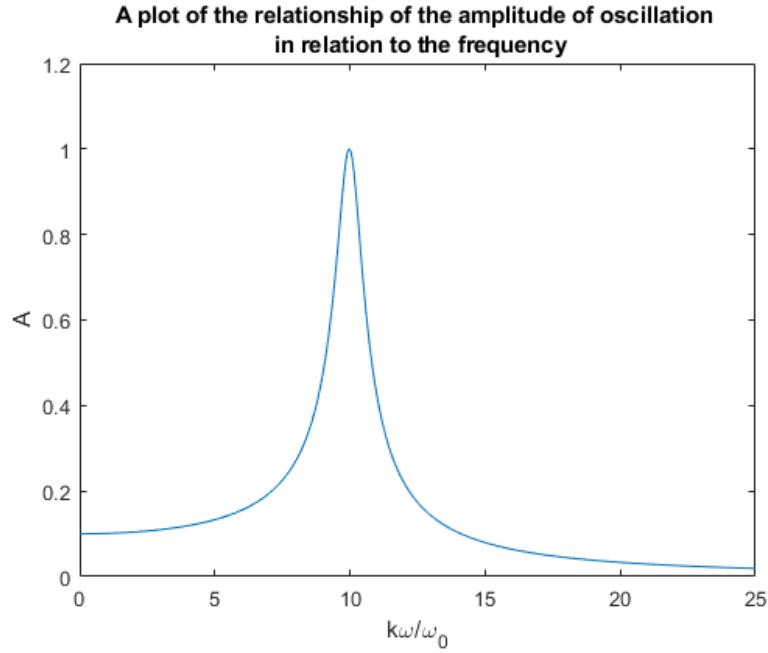


Figure 2.9: A graph of the relationship of the oscillation amplitude as a function of the driving frequency as given in Equation 2.41. A peak is shown as the driving frequency reaches the natural oscillation frequency of the system, that is, the point of resonance. In this graph, k represents an arbitrary constant.

The contribution of forces modelled in the Lennard-Jones potential can influence the oscillation, through the natural static position of the cantilever. By considering the position of the tip as a function of time, oscillations will take place around a static position, that is:

$$z_t = z_0 + z_{ac}(t), \quad (2.42)$$

which leads to

$$\frac{dz_t}{dt} = \frac{dz_{ac}(t)}{dt}. \quad (2.43)$$

Importantly, this leads to the modification of Equation 2.37, which can be rewritten:

$$m \frac{d^2 z}{dt^2} + b \frac{dz}{dt} + kz_{ac} - \left. \frac{dF}{dz} \right|_{z_0} z_{ac} = F(t) \quad (2.44)$$

$$m \frac{d^2 z}{dt^2} + b \frac{dz}{dt} + \left(k - \left. \frac{dF}{dz} \right|_{z_0} \right) z_{ac} = F(t). \quad (2.45)$$

This means that the system with surface interactions can be modified to that of an oscillator with an alternate effective spring constant:

$$k_{\text{eff}} = k - \left. \frac{dF}{dz} \right|_{z_0}, \quad (2.46)$$

and this modifies the effective frequency of the system

$$\omega_{\text{eff}} = \sqrt{\frac{k_{\text{eff}}}{m}} \implies \omega_{\text{eff}} = \omega_0 + \Delta\omega. \quad (2.47)$$

The frequency shift can then be determined:

$$\omega_{\text{eff}}^2 = \frac{k - \frac{dF}{dz}}{m} \quad (2.48)$$

$$= \omega_0^2 + 2\omega_0\Delta\omega + (\Delta\omega)^2, \quad (2.49)$$

and as $(\Delta\omega)^2$ is very small, it can be assumed to be negligible:

$$\omega^2 + 2\omega_0\Delta\omega = \frac{k - \frac{dF}{dz}}{m} \quad (2.50)$$

$$2\omega_0\Delta\omega = -\frac{\frac{dF}{dz}}{m} \quad (2.51)$$

$$\Delta\omega = -\frac{dF}{dz} \frac{1}{2\omega_0 m} \quad (2.52)$$

It is with this frequency shift that a topographic map of a surface can be taken. At a given point in an NC-AFM scan, the shift in frequency will be measured, which will be shifted in one direction in the attractive potential regimes and the other way in repulsive potential regimes.

2.3.1 Tip Functionalisation and Intramolecular Imaging

The principle of intramolecular imaging has revolutionised the field of SPM. Intramolecular imaging probes beyond the structure of molecular networks and focuses on resolving the internal chemical architecture of a molecule. In 2009, Gross *et al.* [17] published experiments pioneering the technique of tip passivation in order to image the intramolecular structure of the pentacene molecule.

The technique involves the use of a functionalised NC-AFM tip. This is a tip apex with an atomically well defined termination, such as a CO molecule [17]. The terminating atom or molecule serves to alter the reactivity of the tip and that with which it is interacting. The method on which intramolecular imaging relies depends on several physiochemical principles. Firstly, the tip apex, when terminated with a suitable molecule, has its reactivity with the imaged system reduced, which allows for a closer approach to a surface or molecule, without directly affecting it, and subsequently manipulating that which is being imaged. With a reduced tip sample separation, imaging of both an attractive and repulsive regime is taken with much finer resolution. The enhanced resolution is produced as the repulsive forces contributed by the Pauli exclusion principle contribute more significantly to the quantum forces experienced by the imaged molecule [18]. It should, however, be noted that the enhanced resolution should be interpreted not solely as a consequence of passivation but rather it is a question of a different balance of interaction energies and even with a reactive tip, submolecular resolution imaging is still possible [19].

There are additional factors that contribute to the enhanced resolution offered through the passivation of the tip. One of these factors is the termination of the tip. A molecule that terminates the tip, while not being of the same material as the tip, is capable of being moved or distorted further enhancing the resolution of the tip. This is certainly true of CO, which is capable of additional bending at the tip apex [18].

To conduct imaging of this kind then, it is necessary to terminate the tip with such an apex. For experiments conducted in Chapter 5, NC-AFM was conducted with a CO terminated tip.

Figure 2.10 shows an STM scan of CO deposited on a surface of Au(111). The appearance of the molecule changes in STM when a CO molecule is present on the tip. This is then a good indicator of tip functionalisation and therefore a signal to switch to NC-AFM to obtain high resolution intramolecular scans. When a tip is metallic, that is, not functionalised, CO molecules tend to appear as a dark region and this indicates a region with a reduced LDOS. When the tip is functionalised, however, the CO molecule appears with a bright region in the centre.

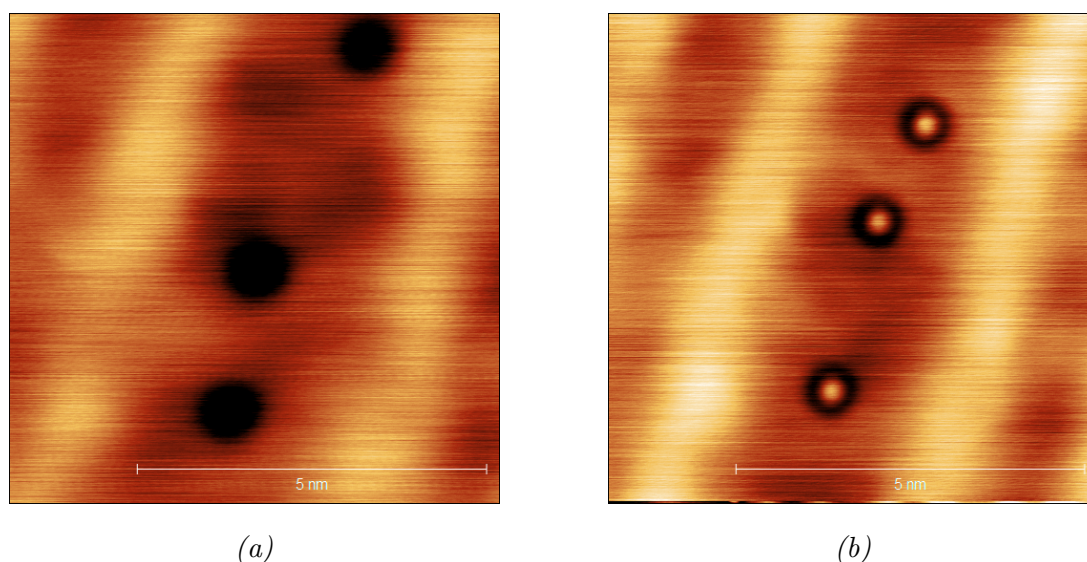


Figure 2.10: A comparison of an STM scan taken (a) before picking up a CO molecule on the tip apex, and (b) after picking up a CO molecule, $V = 3V$, $I = 50pA$, $7 \times 7nm^2$

2.4 Experimental Systems

This section provides a brief outline of the SPM systems utilised for experiments conducted in this thesis.

2.4.1 Omicron VT System

The Omicron variable temperature (henceforth VT) system utilised consists of a single chamber that is comprised of both a sample preparation section and a scanning section. Samples are introduced into the system through the use of a load lock and prepared using a manipulator arm. Transfer within the specific system is primarily managed through the use of a wobble-stick. Figure 2.11 shows an image of the system.

The system was used for room temperature experiments conducted on Au(111) and for the preparation of various silicon samples. A standard base pressure for the system was in the region of $P \sim 1 \times 10^{-11}$ mbar.

2.4.2 Omicron LT System

The Omicron low temperature (henceforth LT) system is separated into two distinct chambers, a preparation chamber and a scanning chamber, separated through a gate valve. The scanning chamber is cooled through the use of a cryostat, which is filled with a cryogenic liquid, reducing the temperature of the scanning chamber. The chamber can then be cooled to the boiling point of the cryogenic liquid. With liquid nitrogen, the temperature can be reduced to temperatures of 77K. Liquid helium, at its boiling point of 4.2K, can also be used, however, due to the limitations of the scanning equipment, the true temperature of the sample will be a little higher ~ 6 K. Manipulation of samples within the system are identical to those used in the VT system. Figure 2.12 shows an image of the LT system. For this thesis, the system was used for the NC-AFM experiments of bi-isonicotinic acid on Au(111). A standard base pressure for the

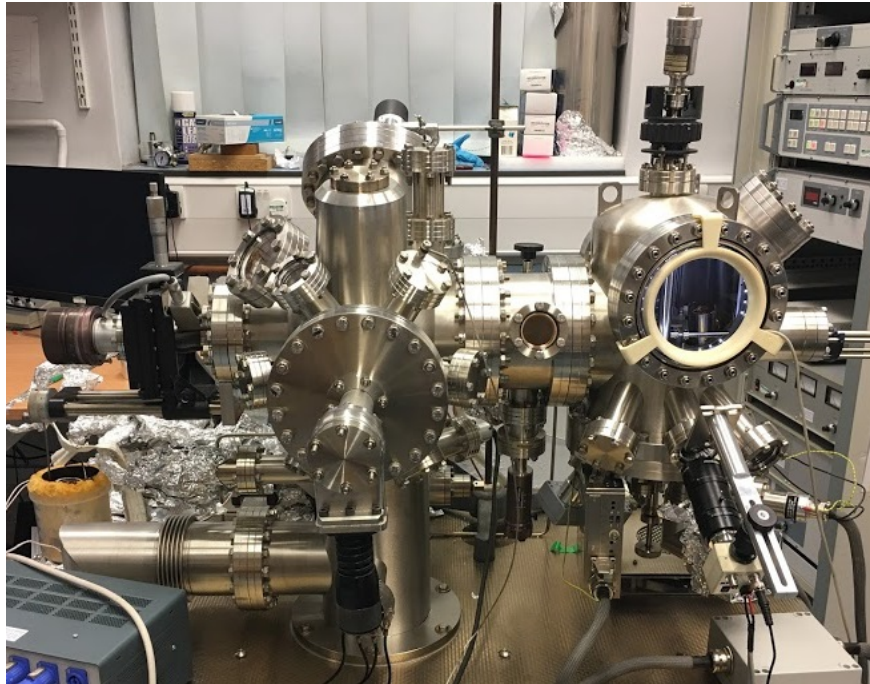


Figure 2.11: An image of the Omicron VT system at the University of Nottingham

system would be measured lower than that of the VT system due to the lower temperature. It measured in the region of $P \sim 10^{-12}$ mbar by an ion gauge.

2.4.3 Createc System

The Createc system is another LT SPM, utilising a cryostat similar to that on the Omicron LT system for sample cooling. Like the Omicron system, it is separated into two parts: a prep chamber and a scanning chamber. Samples are introduced into the system through the use of a load lock and prepared on the manipulator arm in a similar manner to those of the Omicron system. Transference within the system, however, did not utilise a wobble stick, rather, the manipulator arm would clamp and release samples to manoeuvre them into the appropriate position. Figure 2.13 shows an image of the the Createc system.

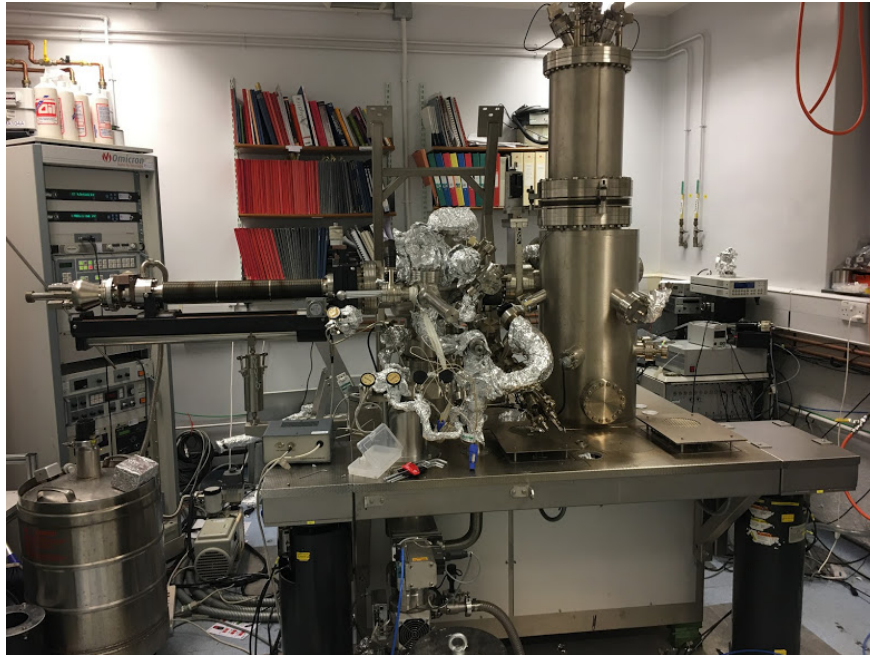


Figure 2.12: An image of the Omicron LT system at the University of Nottingham

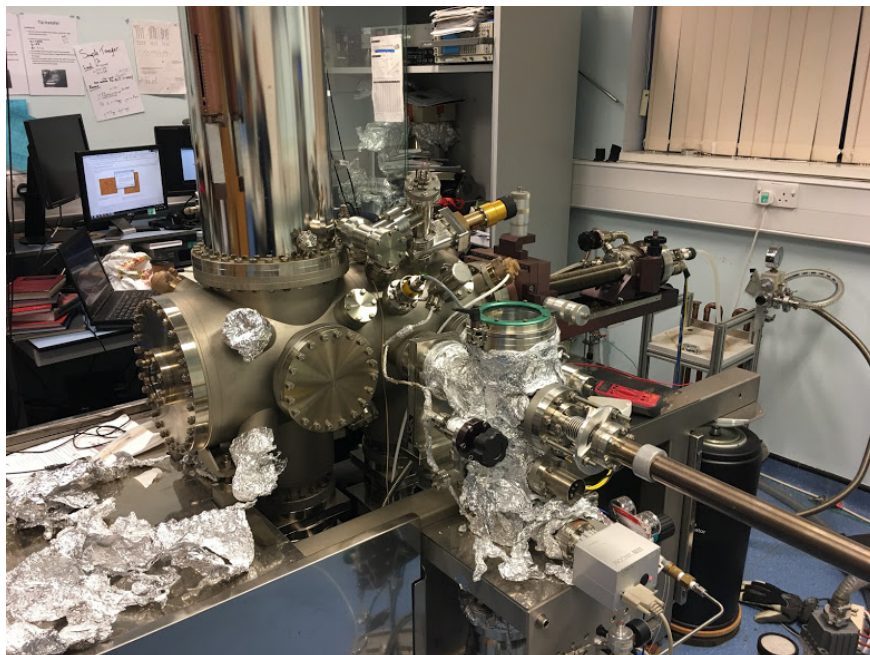


Figure 2.13: An image of the Createc LT system at the University of Nottingham

2.5 Experimental Constraints

The core principles of SPM have been outlined in the previous sections, however, additional considerations are necessary when considering the implementation of experimental SPM, as well as the inclusion of techniques that can further enhance the imaging process such as imaging in vacuum or at low temperatures.

2.5.1 Vibrational Damping

The tip-sample separation required for SPM is typically on the order of angstroms, which complicates the process of imaging at the nanoscale. Typical day-to-day disturbances caused by human motion, human voices and the mechanical vibration of equipment in the lab are of the order of micrometres, and these disturbances must therefore be isolated so as to avoid disturbing the maintained tip-sample separation.

The primary method of vibrational isolation is mounting the scan head on a heavy block that is suspended from springs. The springs are designed so as not to vibrate in sympathy with every day disturbances. Although this method of isolation improves the scanning capability of the SPM system, it can be further improved through the use of eddy current damping. The scan head is surrounded by copper fins, between which, magnets are fixed. When a conductor moves relative to a magnetic field, current loops are induced within the conductor. These current loops induce their own magnetic fields which act in opposition to the magnetic fields of the fixed magnets and thus any movement of the stage is damped away. An eddy current damping system is shown in Figure 2.14.

A further method of vibrational isolation is the use of air legs. The entire SPM system is set on a table under which a number of inflatable legs can be set. When inflated the legs balance the system so it is not in contact with the floor and vibrations can be absorbed by the inflated leg.



Figure 2.14: Photograph of the scan head including the copper fins

2.5.2 Ultra High Vacuum

The first SPM systems designed operated at ultra high vacuum (henceforth UHV). It was found subsequently that systems could operate in ambient conditions. For the materials studied in this thesis, however, UHV was required.

UHV has many benefits that enhance the scope of SPM. Silicon is a reactive material and in normal ambient conditions its surface would be subject to immediate oxidation. Removal of atmosphere with which to react allows the surface of silicon to stay contaminant free for extended periods of time. Additionally, contaminants from the air can degrade surfaces or delicate assemblies of molecules that have been deposited. Thus, even relatively inert surfaces such as gold were studied in UHV conditions in order to preserve molecular structures on them.

Table 2.1 gives a typical labelling convention for levels of vacuum. The regimes are not wholly fixed but rather serve to highlight the approximate level of vacuum associated with each term.

When considering an experimental vacuum it is useful to examine the relationship between the atomic or molecular mean free path and the pressure of the

Level of Vacuum	Pressure
Rough Vacuum	1atm. – 10^{-3} mbar
Intermediate Vacuum	10^{-3} – 10^{-6} mbar
High Vacuum	10^{-6} – 10^{-9} mbar
Ultra High Vacuum	10^{-9} – 10^{-12} mbar
Extreme High Vacuum	$< 10^{-12}$ mbar

Table 2.1: Examples of the definitions of levels of vacuum.

system [20]:

$$L = \frac{RT}{\sqrt{2}\pi d^2 N_A P}, \quad (2.53)$$

where L is the mean free path, P is the pressure, T is the temperature, R and N_A are the gas and Avogadro constants respectively, and d is the diameter gas particles. Using a typical value for room temperature, $T = 300\text{K}$ and an average gas particle diameter of $d = 3 \times 10^{-10}\text{m}$ a graph of mean free path as a function of pressure is given in Figure 2.15. Thus, at UHV pressures, behaviour of gases becomes more akin to the behaviour of ballistic particles.

In order to create a vacuum of this type, several different pumping techniques are utilised. Firstly the UHV system is pumped on with a roughing pump, so called as it creates a rough vacuum in the system. A turbo pump is then used to reduce the system pressure further. Finally an ion pump is used; this ionises gas molecules and attracts them onto an electrode, removing them from the system. The combination of these pumps can preserve a pressure regime of 10^{-11} mbar.

Furthermore, in order to reach these pressures, a further requirement is to bake the system. Molecules of water are a chief contaminant in UHV systems and the removal of these molecules requires raising the temperature of the entire system to above 100°C for days in order for the water molecules to exist in a gas phase and therefore be acted on by the pumping mechanisms.

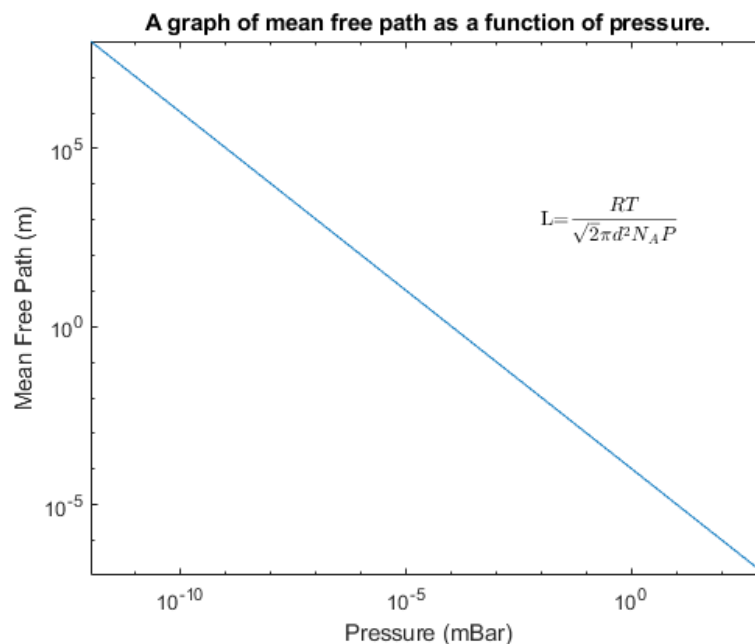


Figure 2.15: A graph showing the relationship of the mean free path of a gas molecule in relation to pressure.

Finally, when working at UHV, all samples and tools must be cleaned so as not to contaminate the vacuum and limiting the pressures. As well as water, organic molecules, particularly the oils that can be present in human skin, can limit the effectiveness of vacuum. As such all samples as tools for handling UHV materials should be cleaned with at least a combination of acetone and isopropyl alcohol. Gloves should also be worn to prevent contamination from human skin.

In order to preserve knowledge and encourage good practice, sample preparation techniques and practices were recorded in a group wiki. This allows an easy access to all standard methods in a written step-by-step format in addition to advice on potential problems. This allows for a high standard and level of consistency when preparing samples. The wiki can be found at the following URL:

<https://www.nottingham.ac.uk/~ppzstm/wiki>

2.5.3 Low Temperature Operation

Atoms and molecules on surfaces are prone to rearranging themselves through translation and rotation due to the thermal energy available at ambient temperature conditions. This can be particularly problematic for imaging, especially in NC-AFM mode. A raster scan may last for as long as an hour while the period of stability for small molecular networks may be of a considerably shorter time scale. The hopping rate of a particle on a surface is given using the equation:

$$\Gamma = n\nu e^{-E_{\text{diff}}/k_B T}, \quad (2.54)$$

where n is a representation of the number of possible directions in which the particle can move, ν is the attempt frequency of hopping, E_{diff} is the potential barrier to hopping, k_B is the Boltzmann constant, T is the temperature and Γ is the hopping rate. This equation is incredibly fundamental in an understanding of physical chemistry and is a representation of reaction rates. The exponential in the equation is the Boltzmann weight, or the probability of a particle occupying a given state. The inclusion of ν in this equation as the number of attempts can also be thought of as the vibrational frequency of the molecule [21], in a broad capacity it is a measure of how mobile the particle is.

Equation 2.54 shows the temperature dependence of the hopping of a particle. In order to produce long time stability of surface structures, it is desirable to reduce the temperature of the studied sample. The equation shows that this temperature reduction has multiple effects. Firstly, the lower temperature corresponds to a lower probability of making a successful hop on the sample. Additionally, as a particle's kinetic energy is a function of temperature, that is $\nu(T)$, with a reduced temperature, fewer attempts at moving along the surface's potential landscape will be made.

In addition to the motion of molecules or atoms on a surface, the tip is also subject to rearrangement at room temperature. The atoms that make up the tip

can change position due to the complicated potential landscape of the tip and that of the combination of tip and sample. Thus cooling the entire system limits the changability of the tip and therefore is a favourable option.

To cool samples, the STM scan head is attached to a cryostat filled with cryogens. With the systems relevant to this thesis, two cryostats were used, an inner and an outer. The outer cryostat is designed to preserve the longevity of cryogens in the inner cryostat. It is filled with liquid nitrogen, cooling the system to 77K. The inner cryostat is in thermal contact with the STM head in order to cool the sample. This can be filled with liquid nitrogen to image at temperatures of 77K, or liquid helium to image at temperatures of 4.2K.

2.6 Etching Tips

As previously mentioned, it is important for tips that are suitable for imaging to terminate with a single atom. This requires a certain level of manufacturing before successful installation into the SPM system. Although several materials are used for the fabrication of SPM tips, those used throughout this thesis were made of tungsten, so chosen because it is a hard metal and not subject to large deformation.

A tip is etched by submerging it partially into a highly concentrated solution of sodium hydroxide at 2 moles/litre, produced by mixing 2g of NaOH crystals in 25ml of deionised water. A current is then passed through a circuit passing through the sodium hydroxide which performs electrolysis on the tip etching it down to a very sharp apex. This tip needs to then be washed in deionised water very thoroughly. The tip is inspected under an optical microscope to make sure it has the characteristic tapered apex.

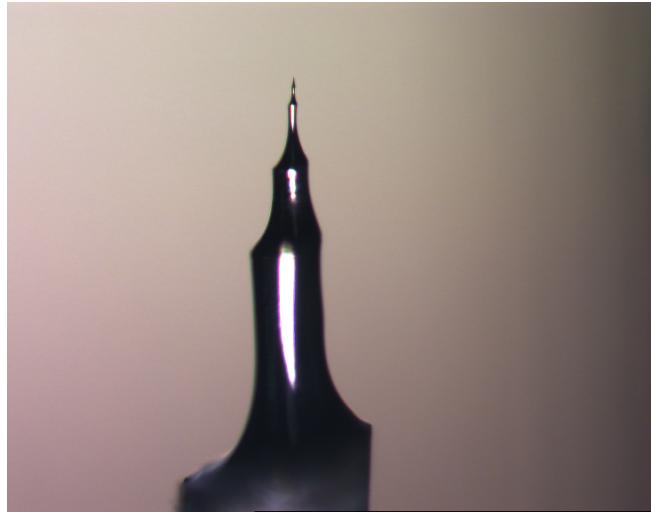


Figure 2.16: A close up of an etched STM tip with the characteristic tapered apex.

2.7 Artefacts

2.7.1 Drift and Creep

Piezoelectric Creep

One of the most rudimentary image artefacts that affects imaging is that of piezoelectric creep. Creep is an artefact that originates from the core aspect of SPM design. From a theoretical point of view, the application of a voltage to a tube scanner results in an immediate adjustment to scan parameters; practically, this is not the case. The fine adjustment of a scan frame typically takes place over a timescale of the order of a few minutes. If a scan is immediately started after a change of position, piezoelectric creep will be observed. The cause is an additional adjustment of position in relation to the scan frame of the desired raster scan. Thus, creep manifests as either a smearing or warping effect within an image. Figure 2.17 presents an example of this effect where a scan frame has been readjusted to the right. The initial lines of the scan show a smearing effect,

that is the step edges present appear artificially curved as the centre of the fast scan direction adjusts.

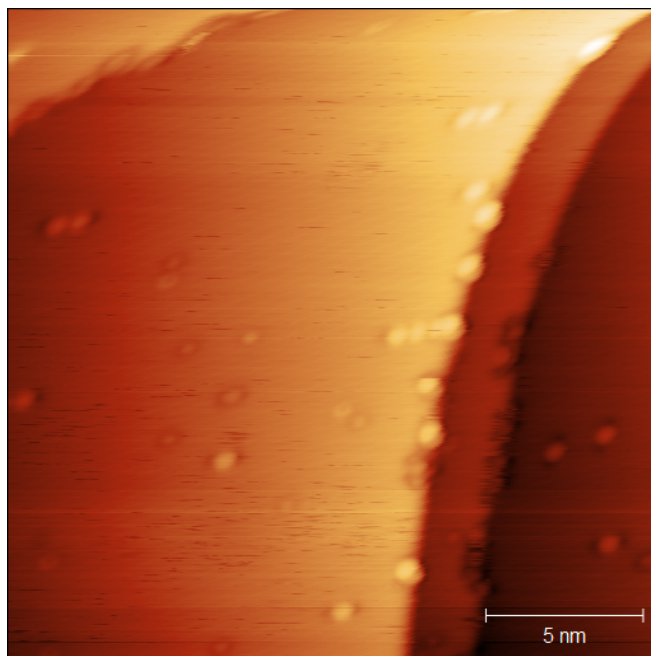


Figure 2.17: An STM scan of Ag(100) showing creep at the top of the image.

Creep is a consequence of the experimental set up but is not an artefact that can be resolved through experimental readjustment, rather, creep is expected when adjusting parameters such as the size or position of the scan frame. Creep will disappear over time as a scan area is repeatedly imaged. While an image with creep may not be truly representative of a scanned surface, it is, of course, not a useless result, still showing key features such as tip sharpness or roughness of surface.

2.7.2 Thermal Drift

The effects of thermal drift are very similar to those seen with piezoelectric creep, namely an unwanted, uncontrolled movement of the tip with respect to the sample. The difference is that creep is an effect that decays over time as a

tube scanner settles in its new position. Drift occurs due to the slow thermal expansion or contraction of different materials in the sample and microscope due to small changes in temperature over the course of a scan [22]. This means that drift is a consequence of temperature differences and therefore may represent a continuous problem.

Unlike resolving creep, drift cannot be resolved by waiting for a scan to settle, however, two experimental practices can address it. Firstly, the underlying temperature difference must be addressed directly. Section 2.5.3 described the effect of temperature on the mobility of adsorbates on a surface, but the use of cryogens to cool a system does have a secondary effect. When cooled, the tip and sample are both put into thermal contact with the cryostat allowing everything to be brought into thermal equilibrium. Although thermal contact is removed when scanning, to allow for vibrational isolation, the temperatures are maintained providing nothing is exposed to a source of additional thermal energy. For this reason, lights that shine directly on the stage to facilitate an approach must be switched off once this approach is concluded or part of the system will be heated and drift will be reintroduced into a system.

A second method of countering drift is through the use of atom-tracking. Atom-tracking can establish the drift velocity of the tip with respect to the sample and then apply the velocity in reverse, thereby keeping the tip stationary with respect to the sample. The velocity is determined by dithering the tip over a feature of the surface and recording how much the feature moves over the time.

2.7.3 Tip Artefacts and Tip Conditioning

It has been repeatedly remarked that for ideal scanning conditions, the scanning probe apex should terminate with a single metal atom. In reality, etching techniques produce a wide variety of far-from perfect tips. It may be that a tip is too blunt, terminates with multiple apexes, or is contaminated. When this tip is

employed to image a surface, these imperfections need to be addressed. Multiple diagnoses and treatments must be considered.

When imaging at the nanoscale it is important to consider that tip may be subject to changes due to the forces and energies that exist in this regime. It is possible that loosely bound surface features may move between the tip and sample. It is also possible that the configuration of atoms that constitute the tip may rearrange or that small adjustments to scan parameters may induce longer-term effects within images. This section considers the diagnosis and treatment of an unsuitable tip.

When an SPM tip is imperfect, that is when it does not taper to terminate with a single atom, a number of image artefacts arise. If a tip is blunt, for example, STM scans will be produced showing a convolution of the structure of the sample with that of the tip at multiple different points. Single features of a surface will be badly blurred leading to a very obfuscated interpretation of the surface. This is shown in Figure 2.18a. Similar effects may occur when the tip is of the right configuration but where adsorbates are present. Tip adsorbates are undesired atoms or molecules which serve to change or obscure the energy landscape of the tip. Even loosely bound adsorbates can be problematic as they may continue to adhere to the tip but move around constantly, meaning the tip is constantly changing shape while scanning.

Another common artefact is that a tip can terminate in multiple apexes. The combination of data from the different apexes leads to the same surface features being imaged multiple times with various levels of contribution. It is most common to see two relatively similar contributions from two tip apexes, referred to as a double tip, though additional tip terminations may also contribute. The effect is similar to multiple exposures seen in a photograph. An example of a double tip is shown in Figure 2.18b.

An imperfect tip can be conditioned in multiple ways, the most common of which is a bias pulse. The principle of a bias pulse is to give the tip a large burst

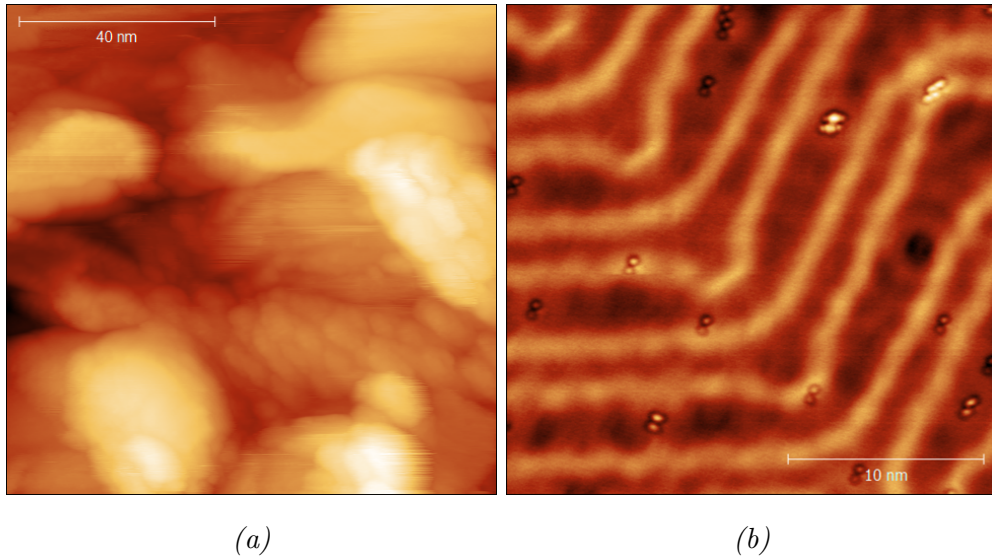


Figure 2.18: Common tip artefacts in SPM. (a) Shows a blunt tip with large blurred features present throughout the scan. These features can be produced from relatively fine features on the scanned surface and subtle detail can be lost. (b) shows a surface with a tip double where surface features reproduced twice. This image also highlights the key feature of a tip double that each feature appears as two features separated by exactly the same separation distance and angle.

of energy allowing the atoms of the tip apex the energy to rearrange. This is achieved by quickly changing the bias applied to the tip to a value different from the scanning bias before quickly returning to this. As well as changing the tip configuration, this may also allow loosely bound adsorbates on the tip enough energy to separate entirely and adhere to the sample.

Another technique is a z-ramp, named for the z axis conventionally being the distance of the tip-sample separation. In a z-ramp the tip is pushed closer to the surface, again allowing top adsorbates to find a more energetically favourable position on the sample rather than the tip. Larger z-ramps will push the tip into the surface of the sample allowing for a more drastic reconfiguration of the tip structure.

A first goal of both of these operations is to remove undesired adsorbates from the tip that could obfuscate imaging. By pulsing or ramping in-front of the tip's trajectory, the appearance of new features on the surface can signify the removal of adsorbates from the tip and onto the surface. It is then good practice to move the scan area away from these features to avoid them re-adhering to the tip. When undesired adsorbates are removed, however, the image may still be unclear due to an undesired tip configuration.

Both bias pulses and z-ramps cause a reconfiguration of the tip structure, however, the fine control over this reconfiguration is limited. The goal is to create the correct tip shape but techniques only change the tip shape with its new shape being unknown without further experimental measurements. Multiple attempts at tip conditioning are usually required with the perfect tip being achieved with a level of luck in that the random change happens to lead to the desired shape.

Practically, this reliance on luck can be reduced to a certain extent by following a general principle. For very bad tips, large z-ramps and pulses may be required to bring the tip closer to its desired state but if an improvement is seen the size of the pulse or ramp can be reduced. The reduction allows for a less drastic reconfiguration of tip structure and the required shape can be approached by tuning in a finer and finer sense.

2.8 Surface Preparation Techniques

Upon mounting a sample onto a sample plate, the first consideration is to degas the sample once in UHV. Despite cleaning samples in solvents before their introduction into UHV, there is likely to be some surface contamination due to adsorbates on the sample and the plate upon which it is mounted. In order to remove these adsorbates, the sample must be heated in order to provide the contaminants with enough energy to dissociate from the surface. This temporarily raises the pressure in the system as the sample degasses.

2.8.1 Sputter-Anneal Cycles

Sputtering

It may be the case for some substrates that nanoscale contaminants may require a more robust treatment to remove. Sputtering is the process through which a surface is bombarded with energetic particles. There are many particles of choice that can be used for sputtering, but for the sake of experiments conducted in this thesis, both argon and neon were used.

The procedure involves leaking a continuous supply of the chosen gas into the system, typically to pressures of around $P \sim 10^{-6}$ mbar. The sample is then placed in front of the sputter gun. The sputter gun ionises an atom in its beam, which then gains kinetic energy and bombards the surface removing contaminants (and also the top several layers of the surface). The effect of sputtering on a surface of Ag(100) can be seen in Figure 2.19a.

Annealing

Following the sputtering of a surface it is generally too rough for study of large deposited molecular networks. Annealing is thus the next step in surface preparation. Annealing generally refers to the heating of a sample and, in a sputter anneal cycle, allows for the movement of atoms on a surface to rearrange into larger ordered terraces, removing the crater-like structures caused from sputtering.

In order to anneal in the STM labs, a current is passed directly across the sample raising the temperature of the sample to $T \sim 600^\circ\text{C}$. The sample is exposed to this temperature for length of time somewhere between ten minutes to an hour. When an anneal is over, the temperature of the sample is reduced and then the sample is further allowed to cool in the scan head, where the pressure is lower, to prevent any contaminants within the system adsorbing on the sample.

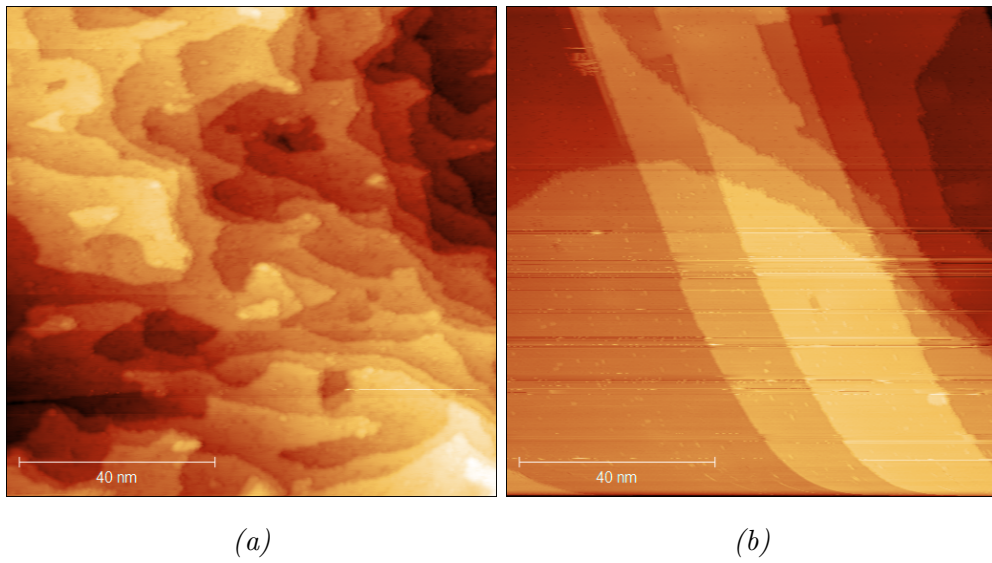


Figure 2.19: STM scans showing the process of a sputter anneal cycle. (a) An example of a sputtered surface of Ag(100). The surface shows a set of crater-like structures where silver has been bombarded by incident argon atoms. (b) An example of the same Ag(100) surface following an anneal. The surface shows a number of step edges but the terrace structure is much larger on this surface.

Chapter 3

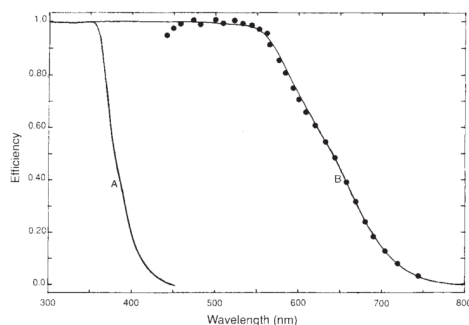
Additional Theory

3.1 Motivation for the Choice of Bi-isonicotinic Acid

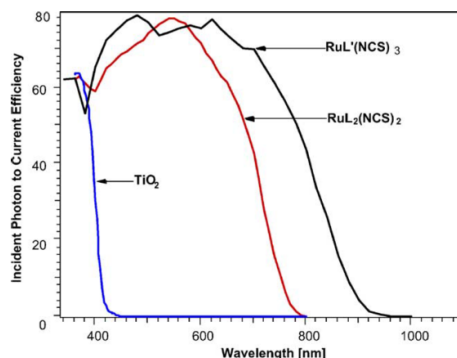
3.1.1 Dye-sensitised cells

O'Regan and Grätzel published, in 1991, a paper exploring the use of dye molecules on a colloidal TiO₂ surface [23]. A colloidal surface was used in order to maximise the available surface area both for photon absorption and dye molecule adsorption. The results are highlighted in Figure 3.1a.

This is further reviewed in another paper by Grätzel, presented in 2001 [24]. He discusses the evolution of photoelectrochemical cells in general and its application in water splitting.



(a) O'Regan and Grätzel, 1991 [23].



(b) Grätzel, 2004 [25].

Figure 3.1: Graphs showing efficiencies of absorption on a TiO_2 surface with and without dye adsorption. 3.1a shows the modification in efficiency against wavelength of light of an untreated surface, 'A', versus one with an adsorbed dye 'B'.

3.1b shows a similar result using different dye complexes, discussed in section 3.1.2.

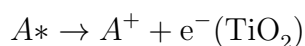
Grätzel cell process

The Grätzel mechanism runs as follows; [referenced from [26], adapted from [23] [25] [24]]:

1. Incident visible light passes through the transparent conductive support and a photon is absorbed by the dye molecule.
2. The photons energy is used to promote an electron from an occupied valence orbital to an unoccupied level. The molecule is now in its excited state.



3. If the excited electrons orbital overlaps energetically with the semiconductor conduction band the electron can potentially transfer into the substrate.



4. The electron will then pass through a network of TiO₂ nanoparticles until it reaches the anode of the circuit.
5. The electron travels through the circuit and its energy can be used to power an electrical item.
6. When it reaches the cathode the electron reduces the electrolyte solution, in this case three iodide ions form a triiodide molecule upon reduction.
7. The reduced electrolyte molecule can then be oxidised to replace the lost electron in the dye molecule. This allows for subsequent electron transfer cycles using this molecule.

Here, A represents the dye complex.

3.1.2 Ruthenium-based dye complexes

In section 3.1.1, dye complexes were introduced on semiconductor surfaces. Grätzel refers to a number of ruthenium based dyes [23] [26]. Figure 3.2 shows the molecule colloquially known as N3, an example of one of the dye structures. This section will focus on the different molecules adsorbed onto a TiO₂ surface for the purpose of water splitting, as well as a brief glance at the chemistry of the complexes.

Coordination Chemistry

The chemistry detailed is referenced from *Descriptive Organic Chemistry* by James and Kathleen House [27]. The dye molecules studied in this review are examples of coordination complexes, containing coordinate bonds. A coordination bond is one in which both of the electrons used to form the bond come from one of the atoms, rather than each atom contributing an electron to the bonding pair [27]. The coordination complex centres on an individual metal atom, ruthe-

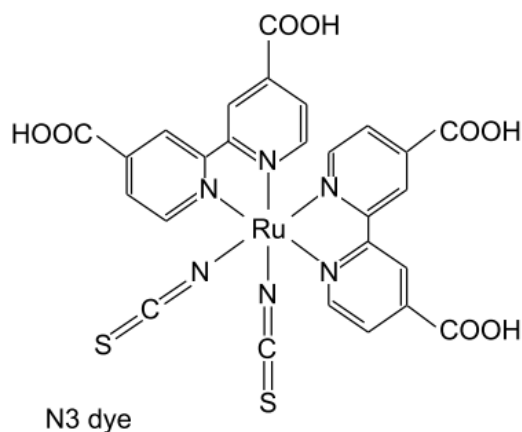


Figure 3.2: The N3 molecule, known formally as *cis-bis(isothiocyanato)bis(2,2'-bipyridyl-4,4'-dicarboxylato)-ruthenium(II)*.

nium in this example, bonded to a number of neutral atoms or molecules which donate electrons to the complex, these are known as ligands.

A feature of the bi-isonicotinic acid ligands, specifically the carboxyl groups allow the molecule to attach itself to a TiO_2 surface [28]. Apart from the use of carboxyl groups, and it can also function as a catalyst in the water splitting reaction, discussed in section 3.1.2. A final useful nature of the discussed dye structures are their long term stabilities, where the molecule stays intact through the catalysation and electron transfer.

Ruthenium Dye Complex Structures

Grätzel states that the best photovoltaic performance in terms of conversion-yield and long-term stability has so far been achieved with polypyridyl complexes of ruthenium and osmium. The most promising sensitisers have the general structure $\text{ML}_2(\text{X})_2$ [25]. Here L represents 2,2'-bipyridyl-4,4'-dicarboxylic acid, M represents the central metal atom (Ru or Os, as mentioned), and X represents a halide, cyanide, thiocyanate, acetyl acetonate, thiocarbamate or water substituent. Grätzel reports the N3 dye as unmatched in solar to power conversion until 2001, when the “Black dye” (tri(cyanato)-2,2'2"-terpyridyl-4,4'4"-

tricarboxylate)Ru(II) achieved a record of 10.4%; this molecule is shown in Figure 3.3.

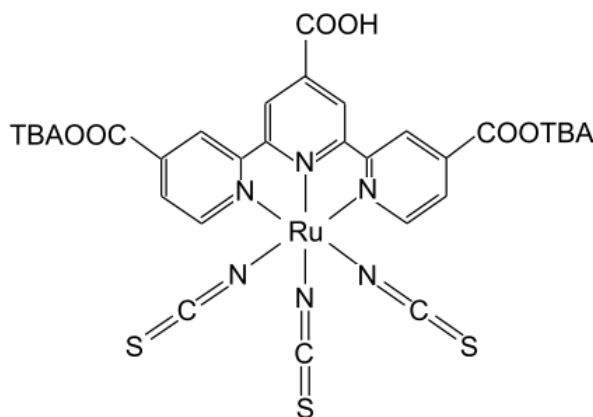


Figure 3.3: The “Black” dye developed by the Grätzel group. In this image, TBA refers to a tetrabutylammonium cation.

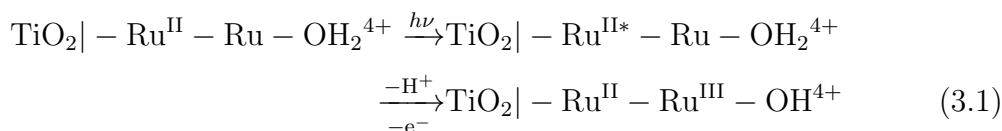
It is worth noting that so far single stage dye complexes have been discussed. This is down to the discussion of theory and the mechanisms that take place at the different stages. There has also been substantial research into multistage complexes, those with multiple ruthenium centres, where electron transfer takes place through each centre before transferring to the TiO_2 surface. This will be discussed further in section B.0.1.

Catalytic Use of Ruthenium Dyes

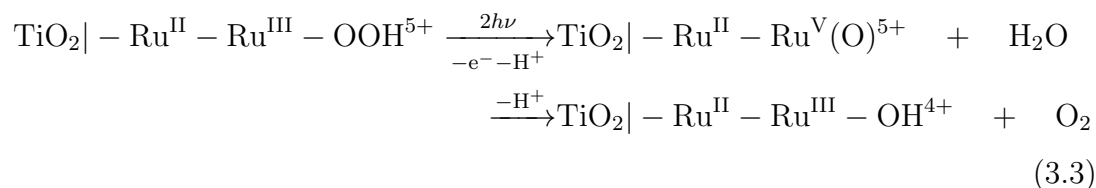
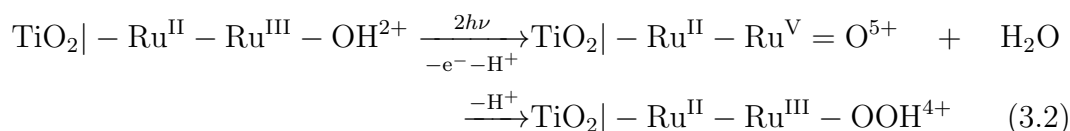
As well as providing the means for efficient electron transfer under illumination, the dye complexes have a secondary function, which is useful for the purpose of photocatalytic water splitting; the complex can also function as a catalyst for the water splitting reaction. This is achieved by allowing a water molecule to become a ligand in the ruthenium coordination complex. From here the electron transfer alters the nature of the water molecule, facilitating oxygen evolution, while the ruthenium complex remains unaltered other than its oxidation state. An example of this mechanism has been adapted from Concepcion et al. in the

2009 paper [29]. Using a multi stage dye complex, an example of the progression of this reaction can be seen.

Catalytic Cycle — Initiation



Catalytic Cycle — Cycle



A multistage complex can be constructed with two metal centres; these are labelled the charge transfer centre and the reaction centre [26] and this is illustrated in Figure 3.4.

This molecule is the culmination of the theory written in this section. The molecule shown in Figure 3.4 is made of two ruthenium complexes. The reaction centre allows the bonding of a water molecule and allows the catalytic reaction to take place.

3.1.3 Charge Transfer Dynamics

Examining in more detail, Weston *et al.* researched in the 2011 paper the mechanism of charge transfer from dye molecule to substrate [30]. The molecules contain one or more bi-isonicotinic acid ligands, simply the pyridine ligands,

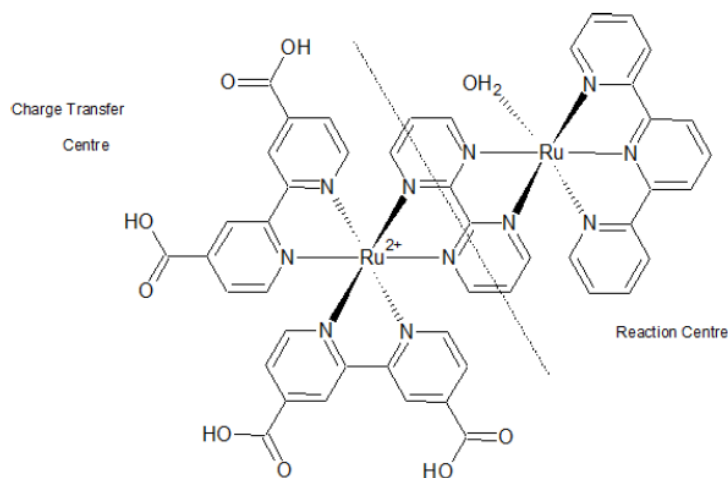


Figure 3.4: A multi-centre dye complex containing the labelled charge transfer centre and reaction centre.

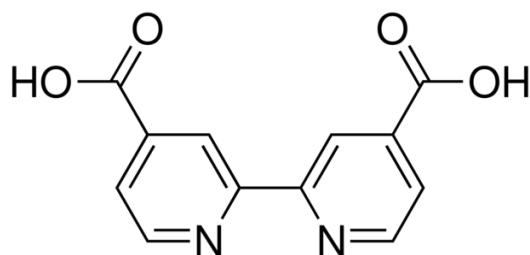


Figure 3.5: The bi-isonicotinic acid ligand.

previously shown with a carboxylic group attached as shown in Figure 3.5 and as discussed in Section 3.3.1.

The carboxylic group allows bonding with the TiO_2 substrate. This coupling allows efficient charge transfer of the LUMO and the conduction band of the substrate. After successful charge transfer, the adsorbed dye molecule would be left with a hole in its HOMO. In photo-voltaic DSCs the hole can be filled by electrons coming from either a liquid electrolyte or an adsorbed layer of gold on the substrate. In a water splitting photoelectrochemical cell the hole is replaced by electrons from the water molecule during the reaction. This process competes with other electron replenishment channels and therefore back transfer of elec-

trons would need to be minimized for an efficient water splitting dye complex. The ability of gold surfaces to transfer electrons to adsorbed molecules would suggest that gold is not a suitable substrate for a water splitting device [30].

Weston *et al.* report results conducted on the undulator beamline I311 at MAX-lab in Sweden. Spectra were collected on three examined molecules, shown in Figure 3.6.

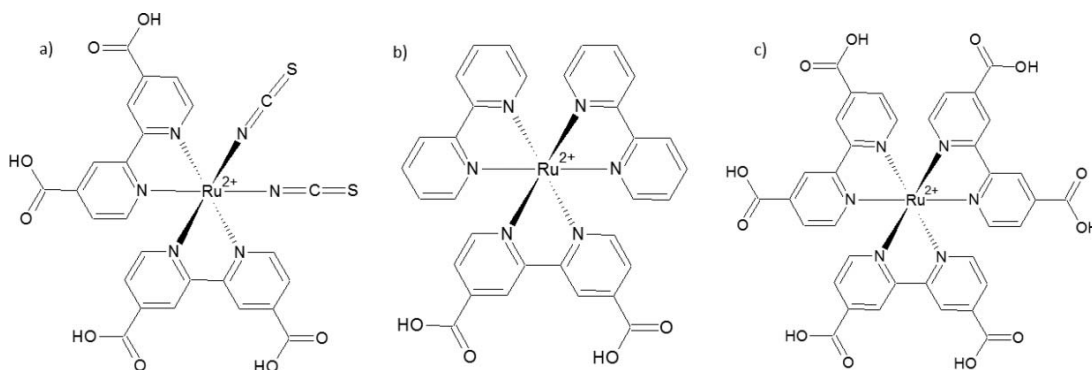


Figure 3.6: **a** is the previously referenced N3 molecule with **b** (Ru 455) and **c** (Ru 470) being based on similar structures [30].

O 1s XPS spectra were taken for the three molecules in monolayer and multilayer, though results are only discussed briefly in this review. Examination was done both in monolayer and multilayer.

In the monolayer sample, peaks were dominant for the TiO₂ surface with two secondary peaks: one showing the carbonyl and carboxylate oxygen atoms and one for the hydroxyl oxygen atom. This peak was not present with molecule **b**, due to deprotonation of the bi-isonicotinic acid ligands. All three molecules bond to the surface with two carboxylic acid groups; these may be present on the same bi-isonicotinic acid ligand or use one group from each separate ligand. In the case of **b**, only one ligand is available.

In the multilayer example the TiO₂ and hydroxyl peaks are at a 1:1 ratio for molecules **a** and **c** in agreement with previous results, though molecule **b** shows

evidence of deprotonation from the surface layer of molecules. Further analyses were made for the N 1s and C 1s peaks [30].

The signature of charge transfer within the complex must be competing with the deexcitation of the excited state via resonant photoemission or resonant Auger. This time represents the lifetime of the N 1s core hole [30]. The intensities of peaks representing the LUMO +2 and LUMO +3 are measured to determine the charge transfer times using equation 3.4.

$$\tau_{\text{EI}} = \tau_{\text{CH}} \frac{I_{\text{RPES}}^{\text{mono}}/I_{\text{NEXAFS}}^{\text{mono}}}{I_{\text{RPES}}^{\text{multi}}/I_{\text{NEXAFS}}^{\text{multi}} - I_{\text{RPES}}^{\text{mono}}/I_{\text{NEXAFS}}^{\text{mono}}}. \quad (3.4)$$

Here τ_{EI} is the electron injection time, τ_{CH} is the average N 1s core-hole lifetime (measured at 6 fs), and $I_{\text{RPES}}^{\text{mono}}$ and $I_{\text{RPES}}^{\text{multi}}$ represent the intensities of the unoccupied peaks being studied in monolayers and multilayers respectively. The ratios on the top and bottom of the fraction provide a normalisation as the intensities are determined relatively, in arbitrary units. For the orbitals studied, timescales of electron injection from the dye complex were found to occur in the 12 - 21 fs range.

Sub-femtosecond range charge transfer

The 2012 Weston *et al.* study investigates two molecules that, once again are based on similar multipyridine based ruthenium molecules [31]. This time the molecule examined was the reaction centre of figure 3.4, referred to as the water splitting dye complex (WSC). For comparison, a second molecule (CISC) was examined with a chlorine ion in the place of the water molecule; this was studied in order to identify any specific interactions caused by the water molecule.

Once again, the intensities of peaks were analysed using the corehole clock method, using equation 3.4. The LUMO +2 and LUMO +3 peaks were again studied, though not the LUMO +1 peak as this cannot be separated from the LUMO itself [31] [30]. Figure 3.7 shows an example of the results. Peaks d and e are the LUMO +2 and LUMO +3 respectively, b and c are the LUMO

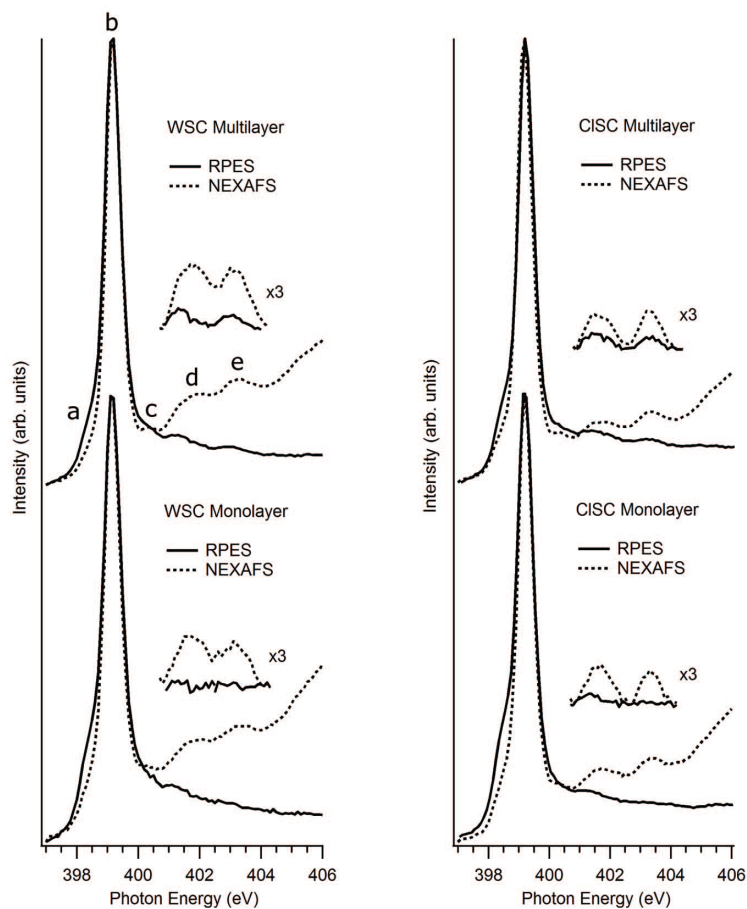


Figure 3.7: Monolayer and Multilayer spectroscopy with the WSC and CISC molecules taken from Weston *et al.* [31].

and LUMO +1 respectively, and peak a is an additional feature that appears in the RPES spectra but is less clearly visible in the NEXAFS. As peak a is also difficult to distinguish from b, it cannot effectively be used for analysis. Results produced by Weston *et al.* give a clear indication that subfemtosecond timescales are possible for ruthenium complexes, though not directly for the WSC itself. Nevertheless this is promising progress.

3.2 Surfaces of Study

3.2.1 Au(111)

Gold serves as a sensible choice of surface for experiments pertaining to this thesis. It is a metal and as such conducting, making it suitable for STM. Furthermore, the inert nature of the surface allows for the observation of deposited molecules with limited interaction with the surface. This also means that interaction between deposited molecules will be the dominant interaction and hence it presents an ideal surface for the study of molecular networks, whether the network is constructed with a single molecule type or multiple different types.

The gold crystal is a face-centred cubic (FCC) structure and thus when cutting the crystal in the (111) plane the unreconstructed bulk structure is shown in Figure 3.8. The reconstruction of gold in the (111) plane is interesting where

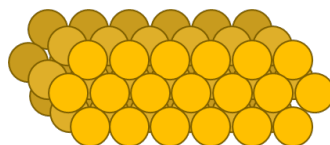


Figure 3.8: The bulk structure of an unreconstructed gold crystal cut in the (111) plane.

for every 44 atoms in the bulk crystal, 46 exist on the surface, this involves a uniaxial compression of the surface atoms [32]. The theoretical view of this is displayed in Figure 3.9. The offset of surface and bulk atoms gives rise to a moving of alignment between the two. This means that a large proportion of surface atoms can be associated with FCC top-layer alignment, while a smaller fraction aligns mostly with hexagonal-close-packed (HCP) surface sites [32]. The top gold layer is then subject to buckling between the FCC and HCP areas leading to the characteristic herringbone surface features.

Preparing Au(111) in UHV is a simple procedure and consists of cycles of sputtering and annealing as described in Section 2.8.1.

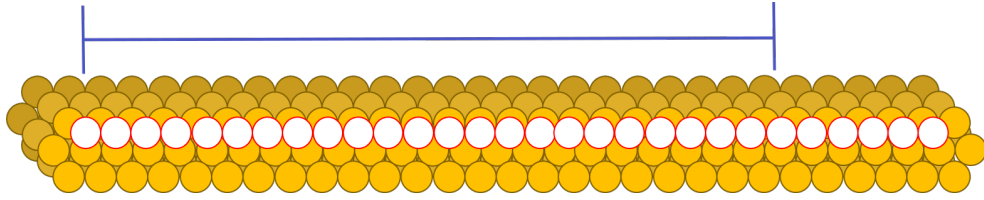


Figure 3.9: Model showing the bulk gold structure in filled gold circles. The overlaid surface atoms are white circles highlighted in red. The blue bar at the top highlights the 22 bulk atoms and the compressed 23 surface atoms that align along this length.

3.2.2 Ag(100)

Silver shares many of the same properties as gold in that they are both FCC structured noble metals with limited interaction with deposited molecules allowing for the study of islands. For experiments discussed in this thesis Ag(100) was used. The (100) surface is illustrated in Figure 3.10. Studies have been conducted of both gold and silver in the (100) to determine the surface reconstruction. Both metals have an inclination for the surface to rearrange into the more compact close-packed configuration. In the case of gold the inclination is strong enough to overcome the energy loss caused from losing affiliation with the bulk substrate below. In the case of silver, however, the energy gained from the modified close-packed surface is not sufficient enough to overcome the energy lost in losing registry with the bulk crystal. [33]

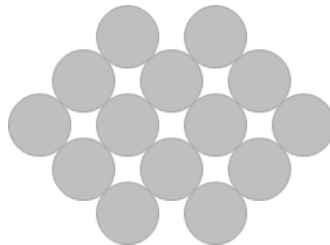


Figure 3.10: The atomic arrangement of the (100) cut of silver.

As with gold, Ag(100) is prepared with sputter anneal cycles described in Section 2.8.1.

3.3 Molecules of Study

3.3.1 Bi-isonicotinic Acid

All of the experiments with molecular deposition conducted within this thesis use the molecule bi-isonicotinic acid (*4,4-dicarboxy-2,2-bipyridine*). This molecule is a component of the larger dye molecules, previously discussed and is shown in Figure 3.11.

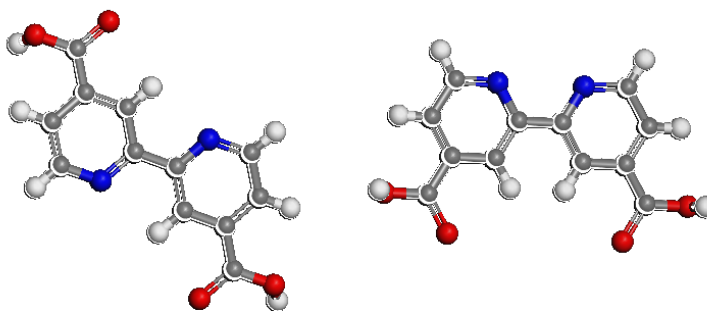


Figure 3.11: The two orientations of bi-isonicotinic acid; the trans form is shown on the left and the cis form on the right. Here, the grey atoms represent carbon, the red are oxygen, the blue are nitrogen and the white are hydrogen.

This molecule interacts differently with different surfaces. On TiO_2 , the molecule will stand with a small tilt angle, less than 25° , considered an upright geometry. On gold, however, the molecule is expected to lie relatively flat with an angle of $70^\circ \pm 5^\circ$ to the normal of the surface. [34].

Upon deposition, the molecule exists in one of two states of conformational isomerism (conformers), a trans conformer and a cis conformer, again shown in

Figure 3.11. This is due to the pure sigma bond connecting the two pyridine rings, allowing for the two halves to rotate, while in gaseous state.

3.4 AFM with a functionalised tip

Both AFM and STM rely on a tip, ideally atomically sharp. In theory the sharper the tip, the better the image resolution. In practice, however, tip preparation techniques are required to give this ideal circumstance. Preparation of a tip while scanning can change the tip's structure with techniques such as voltage pulses or crashing. Even with a very sharp tip, the resolution will be limited. This has led to research into terminating a tip with different molecules or atoms such as CO or Xe [18] [35].

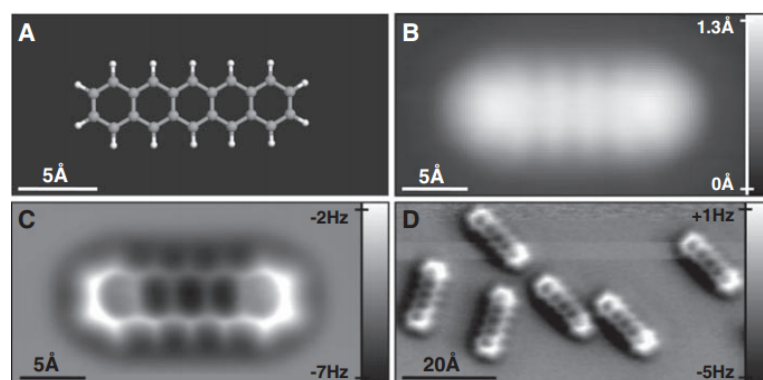


Figure 3.12: Image taken directly from [17]. STM and AFM imaging of pentacene on Cu(111). (A) Ball-and-stick model of the pentacene molecule. (B) Constant-current STM and (C and D) constant-height AFM images of pentacene acquired with a CO-modified tip.

The main reason for using a CO terminated tip is the ability to resolve intramolecular structure, further probing the arrangements of atoms and bonds within a molecule; this is illustrated in Figure 3.12. In order to successfully image at this scale two prerequisites need to be met: (1) the tip must be chemically passivated, such that it weakly interacts with the surface-adsorbed molecule; and

(2) the tip must be “sharp” such that its radius is sufficiently small to resolve atomic features. These two requirements enable the scanning probe to be placed extremely close to the surface-adsorbed molecule, such that a repulsive force is felt between the scanning probe and the molecule arising from Pauli repulsion. Due to the strong localisation of the electronic density directly above the atomic positions of the molecule, the repulsion is strongest when the probe is positioned directly over the atoms and bonds. Therefore, a sufficiently sharp atomic probe can trace the corrugations of repulsion with atomic resolution, thus producing such exceptional images [36].

3.5 Monte Carlo Simulations of Molecular Dynamics

3.5.1 Model

Monte Carlo methods are computational algorithms that simulate physical or mathematical systems. The core principle is to use random sampling methods in order to quantify the evolution of a given system and is of specific use in systems whose long term behaviour is driven by statistical methods [37].

Specific experiments conducted within this thesis model a surface of investigation and splitting this surface into a number of lattice sites. This model is based on the Ising square lattice gas model [38]. In order to explain the specific Monte Carlo methods used, this model will be briefly discussed and then its interpretation and subsequent utilisation for simulating molecules on a surface will be explored.

A square lattice, whose side length is given by L , is constructed of a plane of sites labelled with coordinates (i, j) . The lattice, therefore, contains L^2 sites that are considered randomly and subsequently modified. These sites can be considered either occupied or unoccupied, represented by the parameter n_i , which

is evaluated as $n_i = 1$ if the site is occupied and $n_i = 0$ if it is unoccupied. The energy of a total lattice is then given by the a Hamiltonian [39]:

$$E = -\epsilon \sum_{\langle ij \rangle} n_i n_j + \mu \sum_i n_i, \quad (3.5)$$

where ϵ represents the relative strength of interactivity between neighbouring sites and μ represents the chemical potential of the site itself. The Hamiltonian can be understood as a combination of the attractive nature of neighbouring sites that are occupied and the energy cost associated with physically occupying the site.

This specific model can be utilised in many Monte Carlo simulations but the simulations conducted within this thesis are based on those conducted by Stanard *et al.* [40] describing an ultrathin liquid film. This simulation describes a surface covered with a solution of dissolved molecules. The molecules within the solution have a chance of adsorbing on the surface and this chance is dependent on local properties of a given considered lattice site, that is, given by a combination of the relative repulsive chemical potential of the surface and the attractive potential of molecules that are present on neighbouring sites.

In the most basic model, the evolution of the lattice is governed by transitions between occupied and unoccupied states. To consider the likelihood of a transition between states, the Boltzmann weight of a state must be considered as the Boltzmann weight is proportional to the probability of occupying a given state. The Boltzmann weight is defined:

$$S = e^{-E_s/k_B T}, \quad (3.6)$$

where S is the Boltzmann weight, E_s is the energy of the state, k_B is the Boltzmann constant and T is the temperature of the system.

3.5.2 Rhombus Tiling on a Triangular Lattice

Modelling a set of occupied and unoccupied sites of a square lattice is straightforward in that it can be represented by a square matrix of zeros and ones. This

model is simple but is limited due to the fact that there may be multiple ways of a state being occupied. Initially, it is also limited that nearest neighbours are defined to be those occupied sites directly above or below, and those directly to the left or right.

A more sophisticated model can be made by considering that states can be defined by more than simply being occupied or unoccupied. Stannard *et al.* define that a molecule that is adsorbed can exist on a surface in multiple orientations and, for this, a more sophisticated model is necessary. This model utilises a triangular lattice rather than a square one and its visual interpretation is given in Figure 3.13. The interpretation is incredibly suited to modelling rhombi as it can be seen from Figure 3.13c that the construction of any rhombus will require the use of both an up-facing and a down-facing triangle.

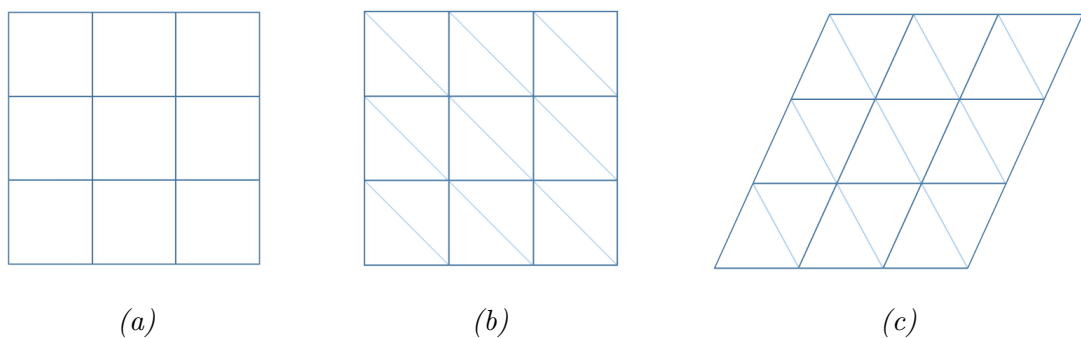


Figure 3.13: The formulation of a triangular lattice by dividing (a) a square lattice into (b) two triangular sections and (c) skewing the lattice.

The interpretation of the new lattice into the form of a matrix can be achieved in a number of ways. The first is the consideration of a rectangular matrix with a 2×1 scale and the consideration of up and down lattice sites separately. The more elegant solution, however, is to take advantage of the necessary condition that the rhombus be constructed of neighbouring up-facing and down-facing triangles. Only half of the lattice sites need to be considered if their occupation can be inferred. An L^2 sized matrix can be constructed comprised of only up-facing triangles. If a matrix is constructed using numbers signifying the orientation of

an occupied site then different rotations of a molecule can be represented through different numbers, as shown in Figure 3.14.

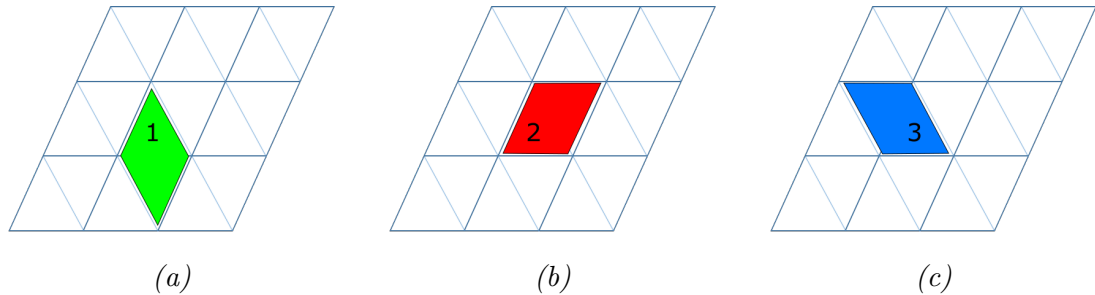


Figure 3.14: The different orientations of molecules with the associated label in the up-facing triangle. Orientation of rhombus is defined by a number.

A matrix can then be populated with numbers between 0 and 3, which correspond to an empty site and the three orientations of rhombi as shown in Figure 3.15. Although this model allows for the representation of differently orientated molecules in an L^2 sized matrix, there is a small caveat. As the second triangle of a rhombus is inferred, there is the potential for two rhombi to utilise the same second triangle. Any algorithm that places tiles into the lattice, therefore, must forbid certain tiles from existing in certain combinations that would overlap each other.

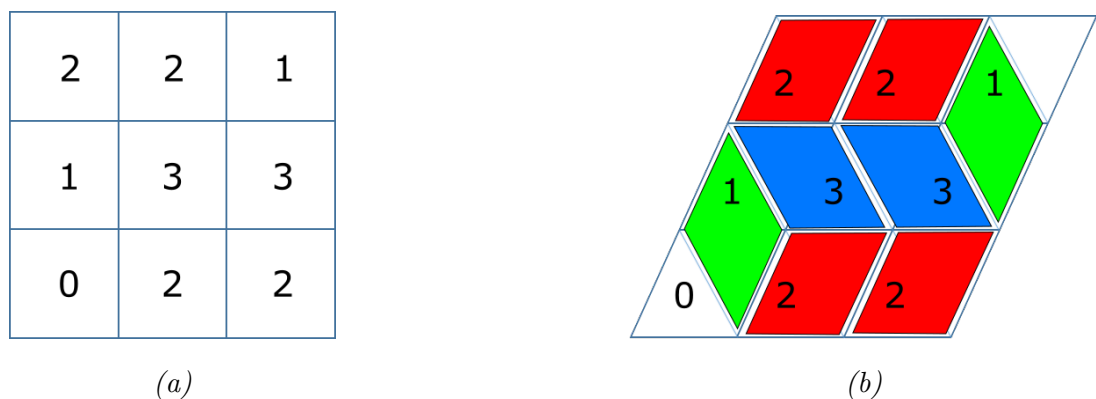


Figure 3.15: A matrix of different states and its interpretation into the tiling model.

3.5.3 The Heat Bath Algorithm

While there are various Monte Carlo algorithms that can be used to evolve a lattice of the form discussed, the one of most relevance to this thesis is the heat bath algorithm. As the probability of a lattice site existing in a given state is proportional to its Boltzmann weight then its true probability can be determined with a consideration of the system's partition function:

$$Z = \sum_i S_i, \quad (3.7)$$

where Z is the partition function and S_i is the Boltzmann weight of state index i . The probability of existing in a given state, $P(i)$, is then given as:

$$P(i) = \frac{S_i}{Z}. \quad (3.8)$$

The heat bath algorithm relies on these probabilities. The routine is as follows:

1. A random matrix site (i,j) is considered.
2. The Hamiltonians for all possible energy states are calculated.
3. The Boltzmann weights and partition function are calculated. If a certain orientation is forbidden from being placed due to overlap, the Boltzmann weight is set to zero.
4. A random number, R , is generated between 0 and 1 and a matrix site, $M(i, j)$, is assigned:

$$M(i, j) = \begin{cases} 0 & \text{if } R < (P_0) \\ 1 & \text{if } (P_0) \leq R < (P_0 + P_1) \\ 2 & \text{if } (P_0 + P_1) \leq R < (P_0 + P_1 + P_2) \\ 2 & \text{if } (P_0 + P_1 + P_2) \leq R \end{cases} \quad (3.9)$$

This is illustrated in Figure 3.16.

- The process is repeated from step one for a preassigned number of Monte Carlo sweeps.

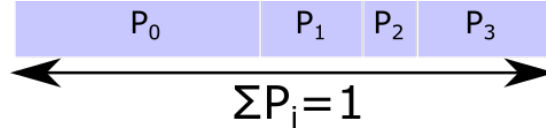


Figure 3.16: Illustration of possible relative sizes of probabilities of states, also remarking that all probabilities sum to 1.

3.6 Simulated NC-AFM Imaging

Advances in SPM imaging techniques have given rise to further need for understanding of how images should be interpreted. An STM or AFM image is not a true spatial representation of the direct topography of a surface along with its features and adsorbates, rather the images should be recognised as a combination of features of the tip, the probe and the energy regime being utilised for imaging. Based on this understanding, it can be very useful to simulate a known surface topography and create an image built through the understanding of the nano-scale interactions between a tip and sample.

Hapala *et al.* presented such a simulation technique which would create a scan based on nano-scale forces experienced by a functionalised NC-AFM tip, while modelling the imaged object as a set of fixed features. In this model, an NC-AFM tip is modelled as the outermost atom of a tip apex and the probe particle that decorates it [41].

Three forces define the imaging in the model proposed by Hapala *et al.* and are illustrated in Figure 3.17. Firstly, the force between the surface and the probe particle, F_{surf} , which is calculated as the sum of all pairwise Lennard-Jones forces acting between the probe particle and the atoms that represent the molecule. Secondly, a radial force, $F_{\text{Tip,R}}$, which exists between the probe particle and

the tip, keeping the probe particle attached to the tip at a particular distance. Finally, a lateral harmonic force, $F_{\text{Tip},xy}$, which arises due to the cylindrically attractive potential of the tip base [41].

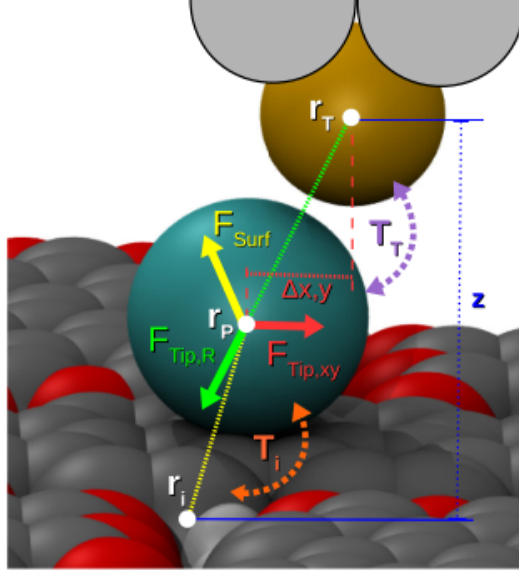


Figure 3.17: An image illustrating the model used for simulations. This image is taken directly from Hapala et al. [41]

By considering the forces experienced by the tip, an appropriate frequency shift can be determined through the use of the Sader formula [41, 42]:

$$\frac{\Delta\omega}{\omega_{\text{res}}} = -\frac{1}{\pi ak} \int_{-1}^1 F(z + a(1+u)) \frac{u}{\sqrt{1-u^2}} du, \quad (3.10)$$

where k is the spring constant of the cantilever, F is the interaction force between tip and sample, ω_{res} is its unperturbed resonant frequency, $\Delta\omega$ is the change in resonant frequency, a is the amplitude of oscillation, and z is the distance of closest approach between tip and sample.

The frequency shift at each point can then be compiled into an image that would model a surface in the same way as NC-AFM. The crucial factor of the model is that it takes into account only the forces acting on the probe due to the presence of physical atoms on a surface and has no interpretation of the underlying electronic structure. This is important as features seen in both

STM and NC-AFM scans need to be understood with their underlying context. Applications of the model proposed by Hapala *et al.* are discussed in more detail in Sections 4.4 and 5.7, which highlight potential interpretations. Section 4.4 gives literary understanding of the model and its application for critiquing images in previous experiments. Section 5.7 shows direct comparison between the Hapala *et al.* model applied with experimental data from this thesis.

Chapter 4

Hydrogen Bonded Molecular Assemblies

4.1 Discussion of Hydrogen Bonding in Supramolecular Assemblies

Hydrogen bonding is of high importance within the experiments conducted within this thesis and, as such, a level of theory of hydrogen bonding has need of discussion. The explanation of a hydrogen bond is not fully explicit but refers to a set of common characteristics and definitions that typify the bond [43]. The hydrogen bond was first proposed by Moore and Winnill in 1912 [44] as a way of accounting for the weakness of trimethylammonium hydroxide as a base [45].

4.1.1 The Hydrogen Bonding Mechanism

A hydrogen atom bonds chemically with a single atom, however, this bond creates a polarisation, leaving the hydrogen atom itself a level of electropositivity. Similarly, polarisation may be formed on other molecules, or elsewhere on the same molecule, in which certain atoms develop a level of electronegativity. Molecules with these associated localised charge polarities show a tendency of mild attrac-

tion and so, while not truly chemically bonded, can interact sufficiently as to be considered in a form of bond; this is a hydrogen bond and is illustrated in Figure 4.1.

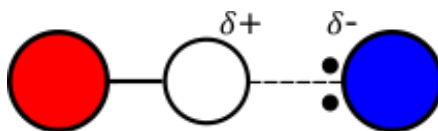


Figure 4.1: A simplified illustration of a hydrogen bond showing the three atoms involved in a hydrogen bond. The red atom is covalently bonded to a hydrogen atom, coloured in white. The hydrogen atom displays a slight positive charge, $\delta+$, which is attracted to the electronegative, $\delta-$, presence of the lone valence pair of the blue atom,

Hydrogen bonding can occur both intermolecularly, that is between atoms of multiple molecules, and intramolecularly, that is between atoms within a single molecule. When forming intermolecular bonds, large networks can be constructed of many molecules bound into networks. Through this mechanism, many complex structures can form with varied chemical properties. Indeed, hydrogen bonding is responsible for the formation of structures in polymers, DNA and proteins.

It is important to understand certain subtleties of the hydrogen bond itself, namely the strength and nature of the bond. Hydrogen bonds can be categorised into strong ($\sim 60\text{--}170\text{kJ mol}^{-1}$), moderate ($\sim 20\text{--}60\text{kJ mol}^{-1}$), and weak ($\sim 0\text{--}10\text{kJ mol}^{-1}$) [46]. While these strengths do vary, they lie below the strengths of typical covalent bonds, which can range from $200\text{--}1000\text{kJ mol}^{-1}$ and the hydrogen bond strengths relevant to molecules such as bi-isonicotinic acid are around $20\text{--}30\text{kJ mol}^{-1}$, an order of magnitude below the weakest covalent bond. Of its nature, the bond is formed by an electrostatic interaction rather than the sharing of electron pairs and, while this distinction has already been made, it is important to take note of this when discussing the imaging of structures in SPM.

There are a number of different ways that molecules can form a hydrogen bond that depend on the structure of the molecules involved. The simplest form of bond between molecules to understand is a single interaction between two electronegative atoms, one of which covalently bonded to a hydrogen atom. In practice, certain molecular structures or the structures of some functional groups can lead to the formation of multiple hydrogen bonds, such as in the case of one carboxyl group bonding with another, as shown in Figure 4.2.

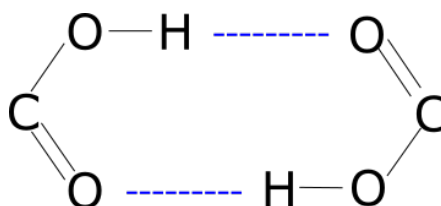


Figure 4.2: A double hydrogen bond, illustrated in blue, formed between two carboxyl groups.

4.2 STM Imaging of Simple Hydrogen Bonded Assemblies

Supramolecular chemistry is defined by one of the pioneers of the field Jean-Marie Lehn as “chemistry of molecular assemblies and of the intermolecular bond” [47]. The scope of supramolecular chemistry is broad but of specific interest are those systems that undergo self assembly through non-covalent bonds, that is here, through hydrogen bonding.

Molecular assemblies have been the subject of a many imaging experiments due to the understanding that can be obtained through the visualisation of these networks. An early example is the work of Griessl *et al.* in the STM imaging of a network of trimesic acid (TMA) on a graphite surface [48]. TMA is constructed of a benzene ring with three carboxyl groups as shown in Figure 4.3a. When deposited on graphite, two different arrangements of TMA molecules were found,

shown in Figures 4.3b and c. The figures show the likely molecular arrangements proposed in the work of Griessl *et al.*, with molecular models produced in Avogadro. The first of these structures is formed when each carboxyl group

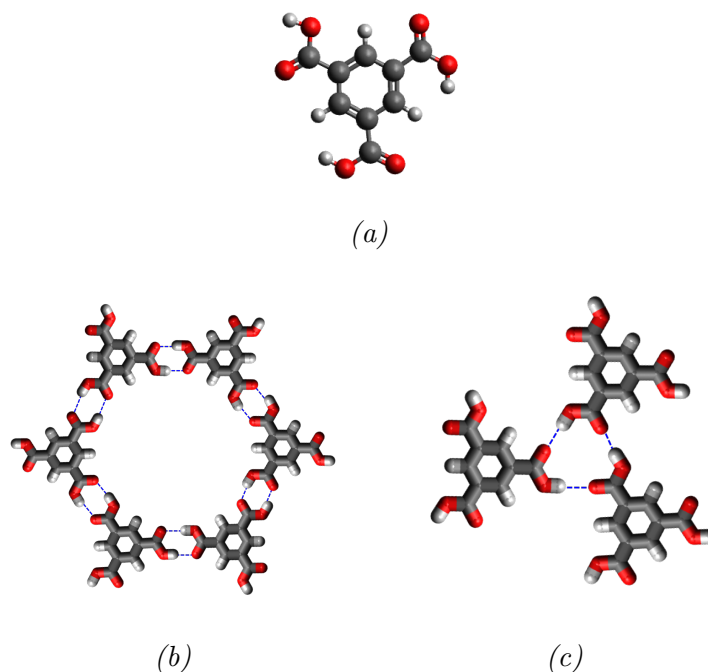


Figure 4.3: Representations on observations of Griessl et al. of the assemblies formed by TMA on graphite. (a) Is the TMA molecule with carbon atoms in grey, oxygen in red and hydrogen in white. (b) and (c) show arrangements that the molecule make due to hydrogen bonding.

bonds directly to a single carboxyl group with the resulting structure showing large rings made of six molecules. The second structure is formed when three molecules join to form hydrogen bonds between the three molecules. This is not a direct bond between two carboxyl groups but rather the shared interaction between three carboxyl groups leading to a different observed structure.

In the case of the former tiling structure, the authors note the presence of bright patches imaged within the ring structure created in the first of the two observed structures. The observation was explained by the presence of a molecule confined within the greater structure of the network, that is, additional hydrogen

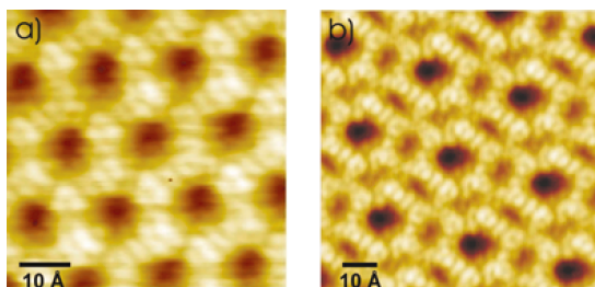


Figure 4.4: The STM images of the two different arrangements of TMA deposited on graphite. Taken directly from Griessl et al. [48].

bonding within the ring structure, this is shown in Figure 4.5. Additionally, this

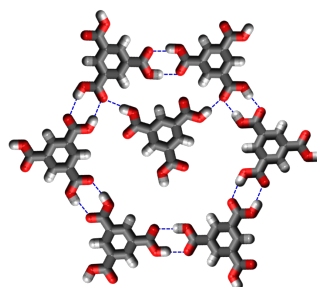


Figure 4.5: An additional TMA molecule confined through hydrogen bonding within the regular ring structure of the TMA assembly.

particular observation can be understood to be a host-guest situation [47].

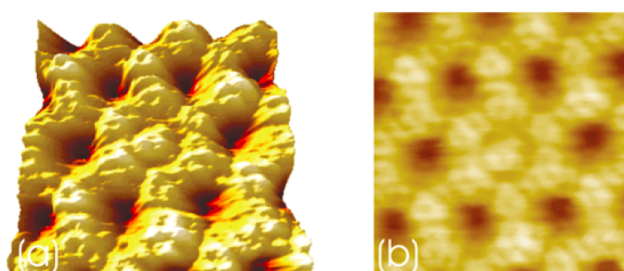


Figure 4.6: The STM images of the host-guest situation. Taken directly from Griessl et al. [48].

Host-guest chemistry can be understood in the most basic sense as a molecular “host” that binds a “guest” molecule and, in the context of the work discussed, the additional TMA molecule can be considered as a guest within the larger complex. It is bound by hydrogen bonding, interacting with two of the already hydrogen bonded carboxyl groups due to electrostatic interactions.

4.3 STM Imaging of Tetracarboxylic Acid Networks

Molecules such as TMA belong to a family of molecules known as tectons. Tectons are molecules with a well-defined shape and multiple sites that engage in strong directional interactions [49]. Tectons are molecules that are considered the building blocks of supramolecular networks, analogous to the way atoms are the building blocks of molecules [47].

Following experiments of TMA deposited on graphite, subsequent studies have been made into molecules with analogous bonding regimes [50]. Figure 4.7 shows the isophthalic acid group, a key component of the TMA molecule. If two isophthalic acid groups are joined to linear connectors, a tetracarboxylic

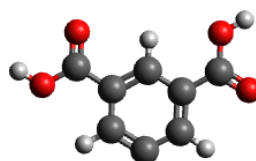


Figure 4.7: The isophthalic acid group with carbon atoms in grey, oxygen in red and hydrogen in white.

acid molecule is formed, that is a molecule with four carboxylic acid groups, and hence four sites with which to bond to an assembly.

Initial studies into these tetracarboxylic acid tectons were conducted by Wuest *et al.* who deposited them onto a graphite surface [49, 50] and further studies conducted by Blunt *et al.* [51, 52].

Figure 4.8 provides a simple illustration of some of the key points in the work on the discussed tectons. Figure 4.8a represents the key common structure between all tetracarboxylic acid tectons, that is, the intermediate linear connection between the two isophthalic groups needs only to be considered as a single backbone, illustrated in black, and the position of the four carboxyl groups are illustrated in red, highlighting the direction and position of possible hydrogen bonds between molecules.

Figures 4.8b and c show the two arrangements observed by Wuest *et al.*, (b) is a parallel arrangement with all molecules in the same orientation and (c) is a Kagomé like arrangement with molecules orientated in flower-like structures.

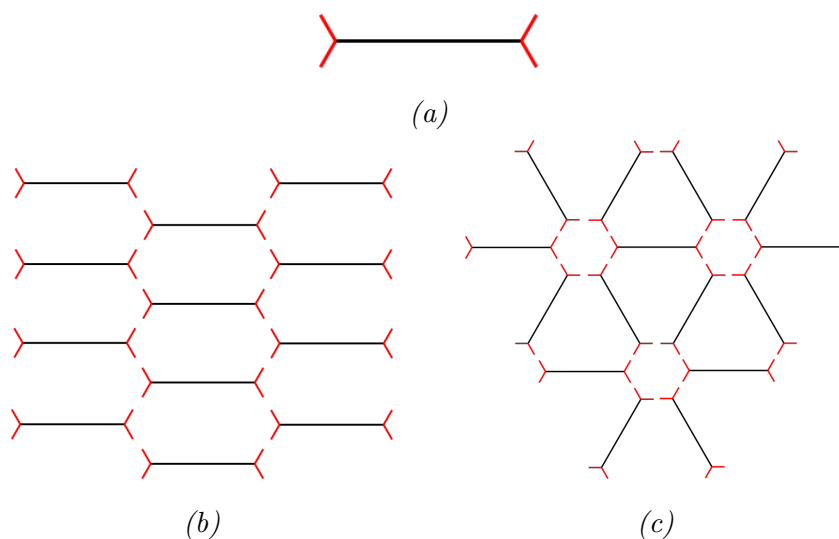


Figure 4.8: Arrangements of tetracarboxylic acid tectons. (a) The structural model. (b) The parallel arrangement. (c) The non-parallel, Kagomé-like arrangement.

The assembly motif observed depends on the specific choice of tecton. Slater *et al.*, in their review of tiling motifs, describe a number of tetracarboxylic acid

tectons with different backbones and their subsequent arrangements based on observations from Wuest *et al.* and Beton *et al.* [50].

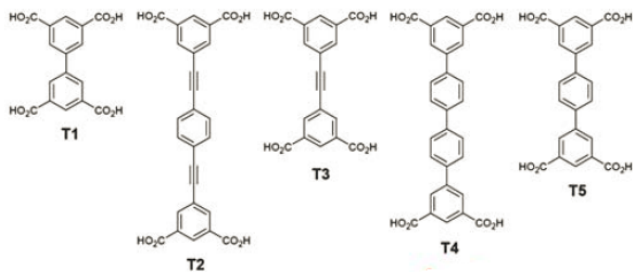


Figure 4.9: Tetracarboxylic acid tectons as labelled by Slater *et al.* The image adapted directly from work by Slater *et al.* [50].

Slater *et al.* observe that **T1** forms a parallel network, while **T2** forms a Kagomé network. **T3** forms a “frustated” system with regions of both parallel and Kagomé motifs with smooth transitions from one arrangement to the other. **T4**, likewise exists in both configurations, but research has shown that its regime can be modified by the addition of coronene. Coronene provides a guest-induced transformation, that is, causes networks to adopt regimes that accomodate it. In this case, the presence of coronene causes the **T4** tecton to adopt the Kagomé motif with the coronene molecule existing in the hexa-isophthalic acid pore.

T5 provides the most interesting structure when deposited. The position of molecules within the array is random rather than being confined to parallel or Kagomé-like arrangements. The reason for the additional arrangements can be understood with reference to the rhombus tiling model discussed in Section 3.5.2. All tetracarboxylic acid tectons can be represented by the tiling of a rhombus in a triangular lattice with the four sides of a rhombus representing the four bonding sites of a tecton.

The stability of arrangements of rhombus tiling can be understood by analysing the meeting points, or junctions, of the triangles in the lattice. Junctions are illustrated in red in Figure 4.10a. The possible fully-occupied arrangements of tiles around a junction are illustrated in Figure 4.10b. Arrangement 1 corre-

sponds to the parallel tiling regime while arrangements **2** and **3** correspond to the Kagomé-like tiling structure of the tectons. The **T5** tecton is able to form all five of these junctions stably, while the remaining four are restricted to only forming the first three. This is down to the physical dimensions of the **T5** molecule. The key dimensions of all the tetracarboxylic tectons are shown in Figure 4.10c with d_1 as the distance across two carboxyl groups and d_2 as the length of the backbone of the molecule. In the case of the **T5** molecule, the two distances are sufficiently similar allowing for the formation of stable junctions **4** and **5**. Both unsuccessful and successful formations of junctions **4** and **5** are shown in Figures 4.10d and e respectively.

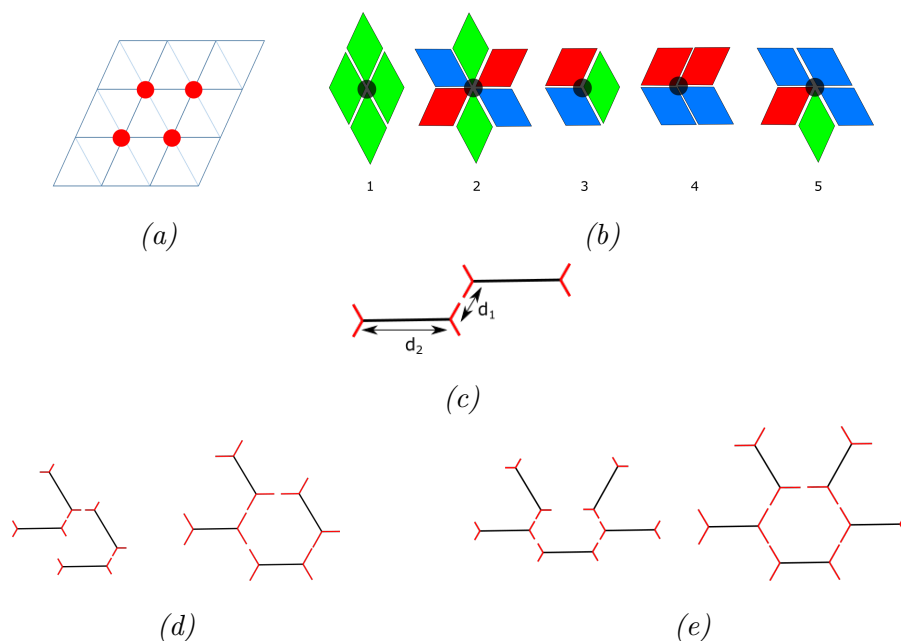


Figure 4.10: An image illustrating the arrangements of molecular junctions. (a) The interpretation of junctions in a triangular lattice. (b) The possible configurations of complete junctions. (c) The key dimensions that define the possible molecular arrangements, d_1 is the distance across carboxyl groups and d_2 is the length of the backbone of the molecule. (d) and (e) The comparison between a stable and unstable formation of arrangements **4** and **5** that depend on the relative lengths d_1 and d_2 .

4.4 NC-AFM Imaging of Hydrogen Bonded Assemblies

The imaging of supramolecular networks with STM can provide an excellent understanding of molecular arrangements within a structure, particularly by considering underlying energies and geometries. To glean a broader understanding, however, other imaging techniques, such as NC-AFM, are equally valuable and have been utilised to develop a richer understanding of these structures.

Zhang *et al.* investigated the nature of intermolecular bonding with NC-AFM, depositing 8-hydroxyquinoline (referred to as 8-hq) molecules onto a surface of Cu(111) [53]. The molecule is illustrated in Figure 4.11a. When deposited, the 8-hq molecules appear as either single molecules or randomly assembled aggregates. Examination of these assemblies under NC-AFM with a functionalised tip led not only to the observation of the underlying structure of the molecule itself, but also to features of similar contrast that existed between molecules. Zhang *et al.* remark that these features coincide with the position of expected locations of hydrogen bonds formed between molecules.

In a similar study, Sweetman *et al.* investigated hydrogen bonded assemblies of naphthalene tetracarboxylic diimide molecules (henceforth NTCDI) deposited on a surface of Si(111) and imaged at 5K [54]. The NTCDI molecule is illustrated in Figure 4.11b.

NTCDI molecules join in rows as shown in Figure 4.12 with two molecules connected by a pair of $N - H \cdots O$ hydrogen bonds. The NC-AFM scans imply the specific hydrogen bonds through the observed orientation of neighbouring NTCDI molecules with respect to each other but, as Sweetman *et al.* discuss, the same intermolecular features observed by Zhang *et al.* are also present in these images. Sweetman *et al.* take a more critical stance on the imaging of hydrogen bonds, comparing their images to a simulated model constructed using the techniques proposed by Hapala *et al.* in Section 3.6. The intermolecular

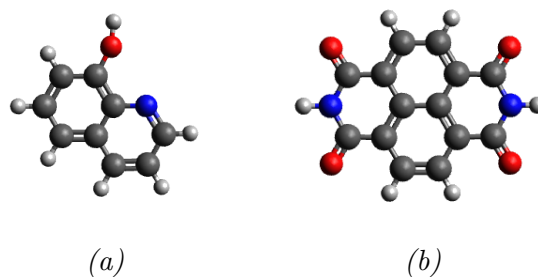


Figure 4.11: Molecules of study under NC-AFM. (a) The 8-hq molecule. (b) The NTCDI molecule. Both molecules are coloured with carbon atoms in grey, oxygen in red, nitrogen in blue and hydrogen in white.

structures appear in their simulated images, despite the fact the model is based solely on the Lennard-Jones forces acting between probe and molecule with no consideration of underlying electronic structure [36].

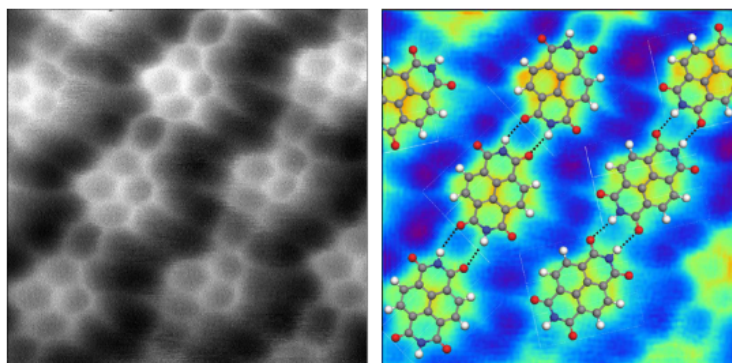


Figure 4.12: Images taken directly from work by Sweetman *et al.* [54] showing hydrogen bonded NTCDI molecules imaged with NC-AFM. Left is the raw AFM scan and right is a colourised version of the scan with the molecular structure overlaid.

Of further significance, with regard to the imaging of hydrogen bonds with NC-AFM, is work by Hämäläinen *et al.* [55] who deposited bis(para-pyridyl)acetylen (henceforth BPPA) onto a surface of Au(111), the molecule illustrated in Figure 4.13. Molecules of BPPA form supramolecular networks with C – H...N bonds between the pyridinic nitrogens and the hydrogen atoms on the pyridine

rings of neighbouring molecules [55]. NC-AFM scans show the intramolecular bonds and intermolecular features where the hydrogen bond is expected. Crucially, however, a further intermolecular feature is seen linking the two nitrogen atoms of two opposite molecules in the network. This intermolecular feature exists directly between two nitrogen atoms with no intermediary hydrogen atom present. This observation shows that features may be observed between two atoms where bonding is not possible but the atomic separations are comparable to the separations of hydrogen bonds.

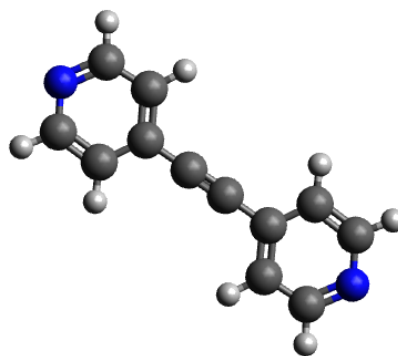


Figure 4.13: A molecule of BPPA with carbon atoms in grey, nitrogen in blue and hydrogen in white.

Hämäläinen *et al.* apply the same comparison between obtained NC-AFM scans of molecular networks and simulated images produced with techniques explained in Section 3.6. Once again the features observed in experimental scans were recreated in the simulations, including the presence of the $N \cdots N$ artifact.

The model proposed by Hapala *et al.* [41] has been of great significance in the interpretation of NC-AFM imaged networks of molecular assemblies. It shows that intermolecular features within networks can be recreated in a simulation that has no interpretation of interactions between atoms or molecules. While the locations of intermolecular features in NC-AFM scans may correlate with the positions of true hydrogen bonds in a network, such features cannot be definitively identified as a hydrogen bond [36].

The successful imaging of a hydrogen bond interaction within a molecular assembly is of great significance to the understanding of supramolecular networks. The definitive identification of hydrogen bonds within molecular structures would have implications for the study and fabrication of such networks and direct identification of hydrogen bonds through imaging continues to be of great interest. Such identification techniques, however, are not currently unambiguous and so while NC-AFM scans with functionalised tips are illuminating to the structure of molecular networks, care must be given to the subsequent interpretation of these images.

Chapter 5

Supramolecular Assemblies of Bi-isonicotinic Acid

5.1 Motivation

Section 3.3.1 mentions that when deposited on gold, bi-isonicotinic acid is expected to lie near parallel to the surface, with its conjugated electron system/fused aromatic rings close to parallel to the surface. [34, 56]. The former of the two papers, *Adsorption and charge transfer dynamics of bi-isonicotinic acid on Au(111)* [34], is of particular interest as it describes inferred surface features of the deposited molecule. Specifically, its referral to O'Shea *et al.* [57], in regards to hydrogen bonding in deposited molecular networks of bi-isonicotinic acid on Au(111) is of interest for the experiments conducted. Despite the large amount of photoemission spectroscopy that has been utilised to study photocatalytic dye centres and ligands such as bi-isonicotinic acid, no imaging of the networks has been studied and, as such, a logical experiment to conduct was that of the bi-isonicotinic acid ligand on Au(111).

5.2 Methodology

The experiment was conducted on a sample of Au(111) on mica. This type of sample consists a thin film of the desired substrate grown on a mica substrate. The film is typically of thickness $\sim 100\text{nm}$. The experiments detailed were conducted on the two Omicron systems at the University of Nottingham, initially the variable temperature (VT) system, and then subsequently the low temperature (LT) system. The samples were prepared in the manner described in Section 3.2.1, that is, cleaned with solvents in an ultrasonic bath and subsequently sputtered and annealed in-situ in UHV. A clean Au(111) sample was imaged as shown in Figure 5.1.

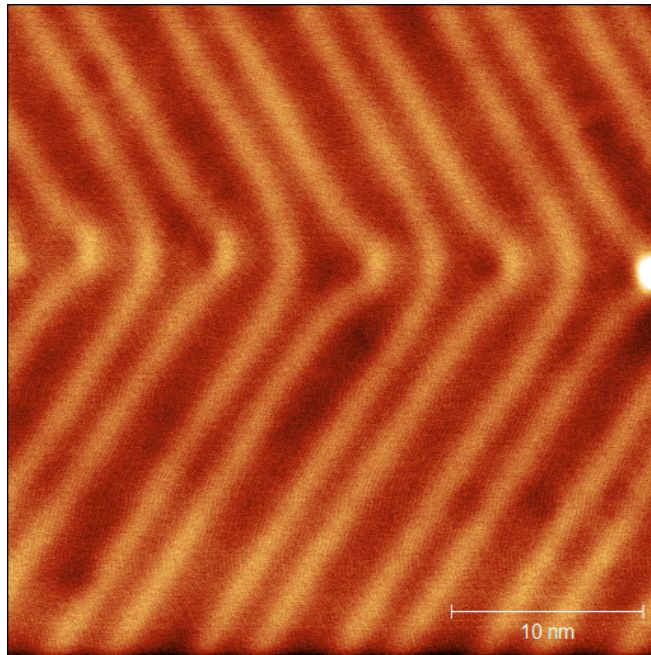
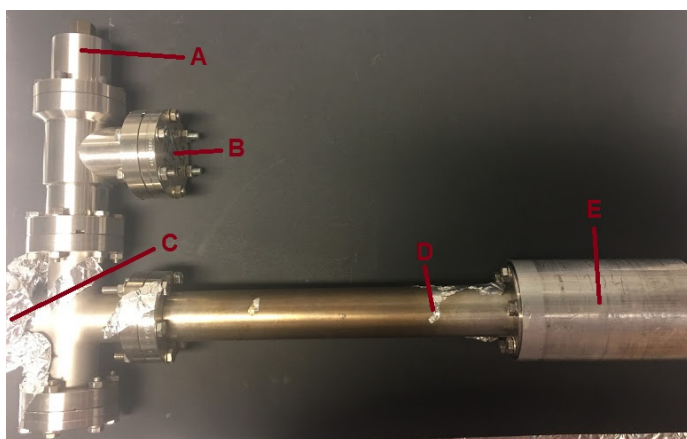


Figure 5.1: Clean Au(111) on mica, $30 \times 30\text{nm}^2$, $V = -50\text{mV}$, $I = 2\text{pA}$, shown here to highlight the herringbone pattern that exists on the bare gold surface. Imaged on the Omicron LT system.

5.2.1 Deposition

Molecules were deposited onto the Au(111) sample through the use of a K-cell. A K-cell is an extension of the UHV system containing a crucible of molecules. The molecules sublime from the crucible when it is resistively heated. Figure 5.2 shows the anatomy of a K-cell deposition source used on the omicron systems.



(a) A photo of a K-cell deposition source. **A**: A right angle valve present to isolate the K-cell from the pumping rig system. **B**: A flange located where a vacuum pumping rig would be located. **C**: The location of attachment to the UHV system. **D**: A chamber housing a crucible containing molecules to be deposited. **E**: An open cylinder containing wires to which electronics are attached, Expanded upon in (b).



(b) **A**: The wires through which a current is passed to heat the crucible in the K-cell. **B**: The probes of a thermocouple allowing for the temperature of the deposition source to be monitored.

Figure 5.2: A K-cell deposition source.

When the K-cell was heated, the pressure rose within the UHV chamber due to the degassing of the crucible. The sublimation temperature of bi-isonicotinic acid is 230°C but this temperature had to be approached gradually as more volatile atoms and molecules would release into the chamber at lower temperatures. So for a clean deposition, the temperature was raised and then the pressure

monitored. The pressure would rise with an increase in temperature and then fall as potential contaminants had been removed from the deposition source. Once the desired deposition temperature was reached, the K-cell was held at temperature for 30 minutes before the sample was placed in the path of sublimating molecules. The sample was exposed for ten minutes before the deposition was stopped. The aim for all experiments was to produce a sub-monolayer (ML) coverage to observe the formed networks as shown in Figure 5.3.

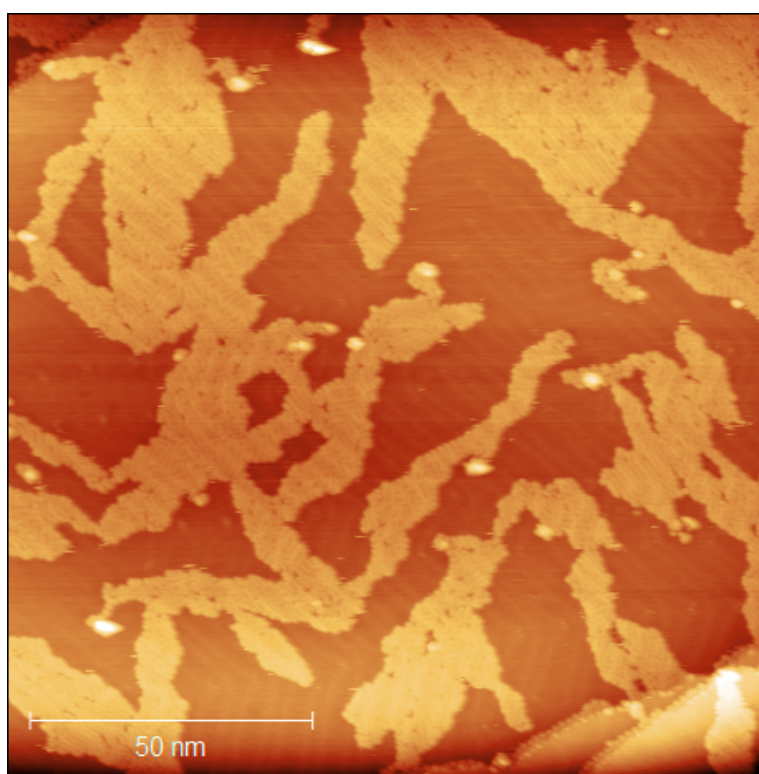


Figure 5.3: Islands of the bi-isonicotinic acid on the Au(111) surface, $150 \times 150 \text{ nm}^2$ original scan, which has been cropped due to a tip instability. $V = 1.5 \text{ V}$, $I = 10 \text{ pA}$.

5.2.2 Imaging techniques

Molecular networks were imaged using the Omicron LT and VT systems, and the Createc system at the university of Nottingham. The networks were imaged at

room temperature but, due to the very mobile nature of the molecules at room temperature, the decision was made to image the molecules at Liquid Helium temperature as well.

It was also decided to further understand the arrangements of molecular assemblies by using NC AFM. In order to further probe the molecular structure, it was decided to use tip functionalisation techniques. This involved the termination of the apex of the tip with a CO molecule as described in Sections 2.3.1 and 3.4. CO as a choice of tip functionalisation also allowed for comparisons with scans simulated using the model proposed by Hapala *et al.* using a flexible probe apex on a simulated tip.

5.3 Network Formation After Deposition

In the gas phase, bi-isonicotinic acid is free to rotate about its central sigma bond, thus the two conformers mentioned in Section 3.3.1 are not defined until a deposition actually takes place. When a molecule is deposited on the surface it gains a surface-induced chirality [58,59], that is, not a true chirality but one that is created by the constraints of existing primarily on a two dimensional surface.

Initial overview scans were successful with Figure 5.4 showing a large supramolecular network. The images were obtained at liquid helium temperatures and show a number of defects within the formed molecular network. This is because the molecules are locked in a local minimum of the potential energy surface, that is, although the entire network is not in its lowest energy state, there is insufficient kinetic energy for the molecules to leave a locally stable configuration. The figure also highlights a number of smaller areas where more localised scans took place. These are shown in Figure 5.5.

The localised scans reveal a greater level of detail of the deposited molecules. As has been repeated in this thesis, the interpretation of STM figures is not a complete schematic view of that which is being imaged but is subject to a level of

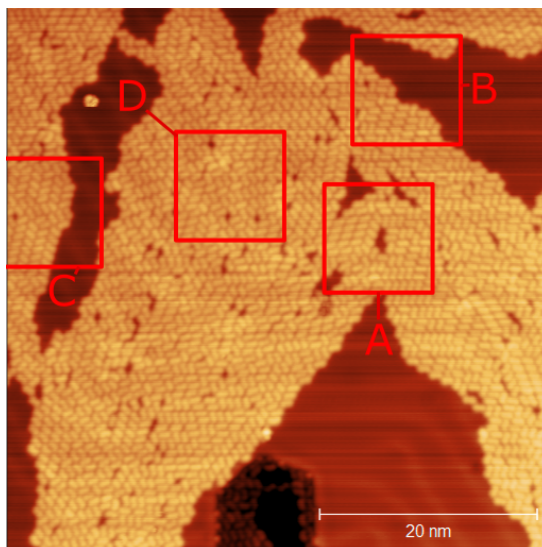
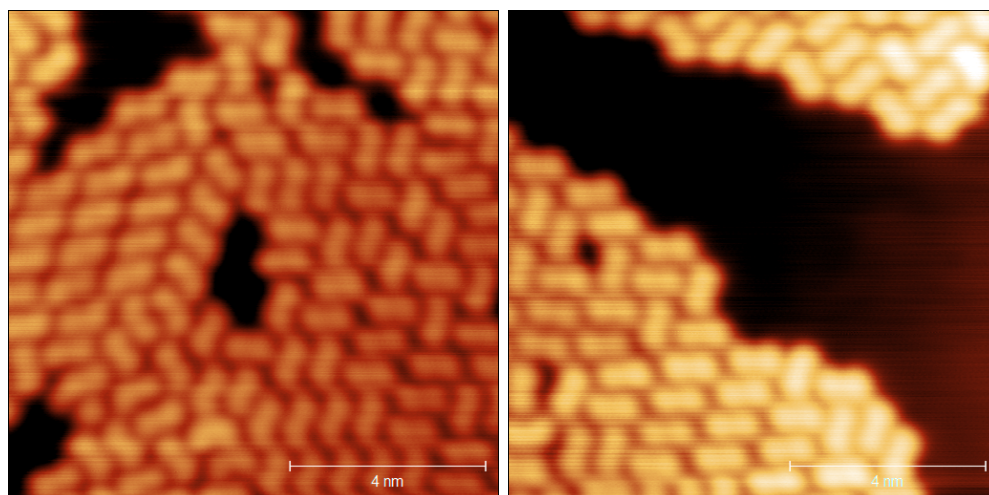


Figure 5.4: Low Temperature image of bi-isonicotinic acid on Au(111), $50 \times 50 \text{ nm}^2$, $V = -0.5 \text{ V}$, $I = 10 \text{ pA}$.

interpretation. Nevertheless, the STM images do provide an initial understanding of the molecular structure. The shape of the molecules is revealed to show two lobes, giving a vague “peanut” shape to the molecule. This shape is likely to be a consequence of the dimer nature of the molecule as discussed in Section 3.3.1. Also mentioned in the section is that the molecule can exist as either a *trans* or *cis* conformer after deposition.

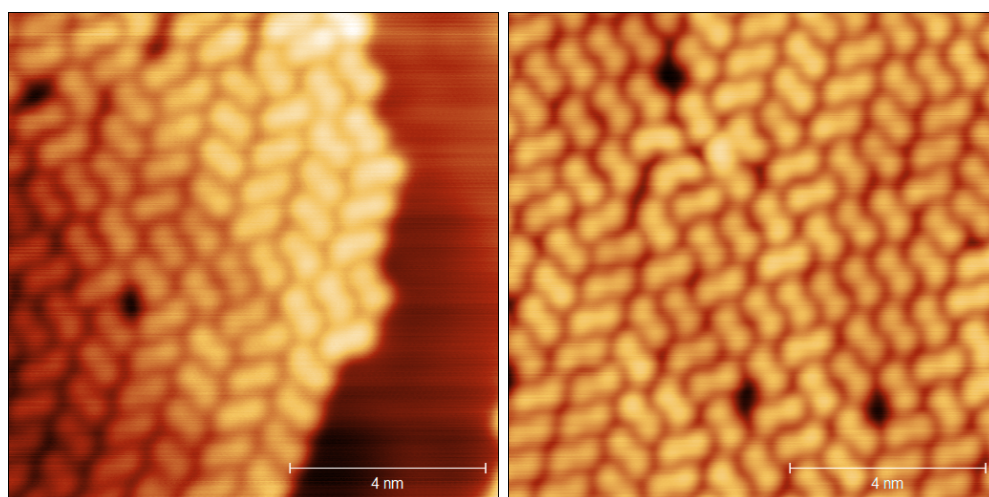
Figure 5.6 highlights a view of Figure 5.5d with a greater contrast and outlines added to show the projected shape of the molecules underneath. Based on the shape of the imaged molecules, it was inferred that most bi-isonicotinic acid molecules were *trans* conformers when deposited on a surface. Figure 5.6 displays probable forms of molecules based on shape, where molecules that appear to be *trans* conformers are highlighted in blue, while the *cis* conformers are represented in green.

The STM scans show a preference for the *trans* conformer in two dimensional networks on the surface. Molecules are locked into their configuration on deposition so the act of deposition, when a molecule adsorbs onto the surface



(a) $10 \times 10 \text{ nm}^2$,
 $V = -0.5 \text{ V}$, $I = 10 \text{ pA}$

(b) $10 \times 10 \text{ nm}^2$,
 $V = -0.5 \text{ V}$, $I = 10 \text{ pA}$



(c) $10 \times 10 \text{ nm}^2$,
 $V = -0.5 \text{ V}$, $I = 10 \text{ pA}$

(d) $10 \times 10 \text{ nm}^2$,
 $V = -0.5 \text{ V}$, $I = 200 \text{ pA}$

Figure 5.5: Localised areas obtained from taking localised scans, initially determined from the overview scan as given in Figure 5.4.

is likely to be the point at which this is defined. The increased observation of *trans* conformers could arise in several ways. Firstly, in the gas phase, molecules may spend less time statistically in a configuration that is likely to form a *cis* conformer, due to the presence of two repulsive nitrogen atoms. This would be a

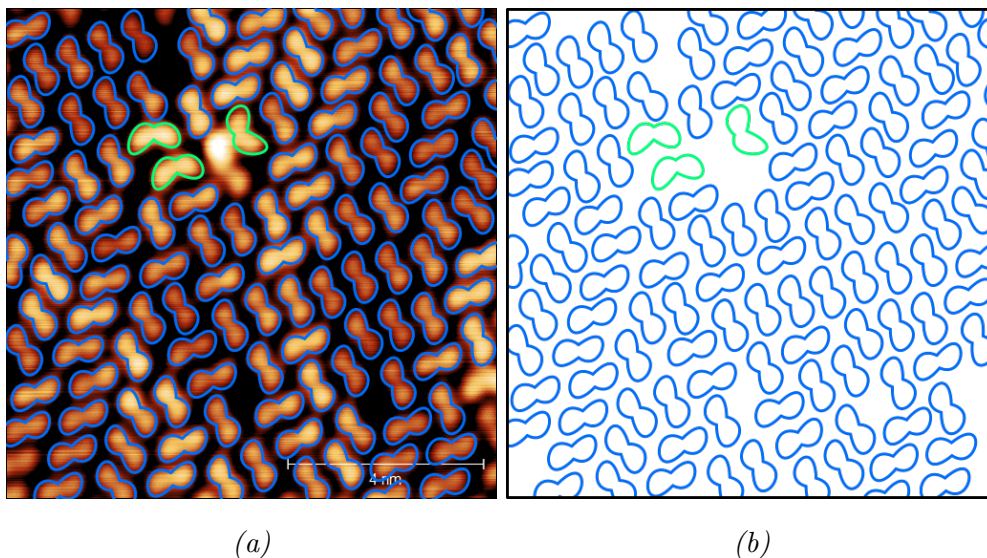


Figure 5.6: An modified view of Figure 5.5d with individual molecules highlighted. The blue molecules are inferred to be in the *trans* configuration while those in green are inferred to be in the *cis* configuration.

statistical phenomenon. Secondly, due to the geometry of the model, it may be that *trans* conformers are more energetically favourable to bind into a regular molecular network and, as such, a large proportion of the existing *cis* conformers may simply not remain attached to the observed 2D networks.

5.4 Molecular Constraints After Deposition

Analysis of the behaviour of bi-isonicotinic acid molecules in regard to their network formation must begin with an understanding of the restrictions placed on possible molecular rearrangements when deposited on a surface. Figure 5.7 provides a list of possible reconfigurations that an unrestricted molecule could undergo.

Translation and rotation can be simply understood as a free molecule changing its position or orientation due to diffusive behaviour on a sample surface. The surface-induced chirality means that the *trans* conformers can exist in two differ-

ent orientations, enantiomers of each other, where one is a mirror reflection of the other. The physical implications of a switching between enantiomers would require the entire molecule to flip when on a surface. In a similar fashion, while the sigma bond connecting the two pyridine rings can be considered easily rotatable if the molecule is in a gas phase, upon deposition a species switch would require half of the molecule to rotate while the other stays fixed, thus switching between conformers should energetically unfavourable. Based on energy requirements, the probability of either conformer or enantiomer switching events occurring should be considered remote to impossible.

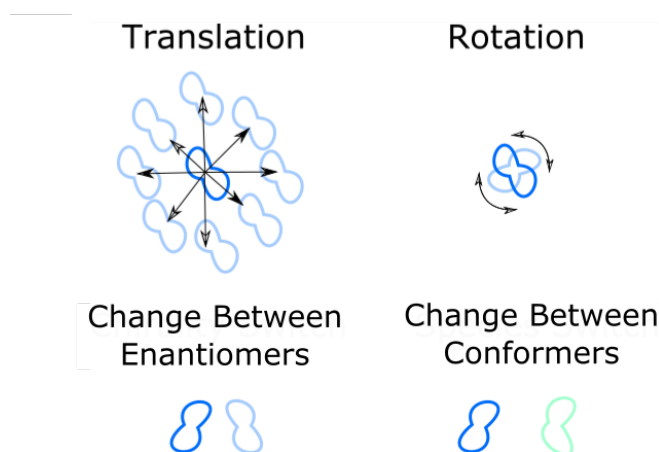


Figure 5.7: A diagram of all possible transformations of a molecule with unrestricted motion.

The physical implications of this limitation of degrees of freedom is that once a molecule is adsorbed onto the surface, its conformerisation and enantiomerisation are fixed properties.

Analysing Tiling Areas

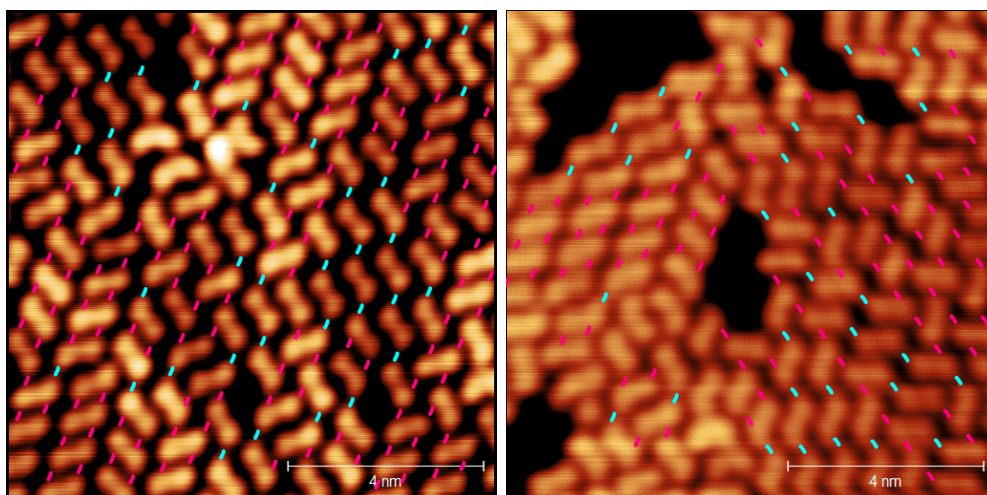
Of first consideration to arrangement of molecular networks is a surface-induced chirality, that is, while lying flat on a surface, the enantiomers of the *trans* conformers cannot be superimposed onto its mirror image.

Further analysis of the localised scans of Figure 5.5 reveals an important point in the arrangement of bi-isonicotinic acid. Examination of Figure 5.6 reveals that for all blue coloured, *trans* orientation molecules, bonding can only take place either between a single enantiomer *trans* molecule in an identical orientation or those of the other enantiomer locked, likewise in a specific alternate orientation.

The emergent constraints can begin to be discussed by examining Figure 5.8a, which shows projected hydrogen bonds based on the suggested molecular forms obtained from Figure 5.6. Two known hydrogen bonds can then be projected onto the image. These projections are carboxyl to carboxyl bonding (coloured in blue), and carboxyl to nitrogen bonding (coloured in magenta). The most striking feature of the projected bonds is that they all lie in same orientation. A hypothesis can be drawn at this point in the analysis; a defining feature of the network is that all hydrogen bonds, regardless of type, lie in identical directions. It is therefore to be considered that the direction of hydrogen bonding would define a tiling domain. Additionally it should also be noted that the greater presence of magenta bonds to blue indicates a preference for carboxyl to nitrogen bonds in comparison to a carboxyl to carboxyl bond within the STM studied network.

Figure 5.8b further explores projected hydrogen bonds and shows two domains meeting with hydrogen bonds highlighted in the same manner. Once again, in a given domain, molecules can exist as either enantiomer but in fixed orientations for the molecules within any given domain.

Figure 5.8 reveals an underlying subtlety in network formation, namely the hydrogen bond direction defining the overall network growth. Only molecules of the correct rotational-orientation and enantiomer combination will be able to bond within a network, thus molecules orientate themselves to the network. The bond direction is a local emergent property rather than a global one, meaning different domains can form in different local orientations. These networks cannot merge upon meeting, however, as their bond direction will be different. Networks



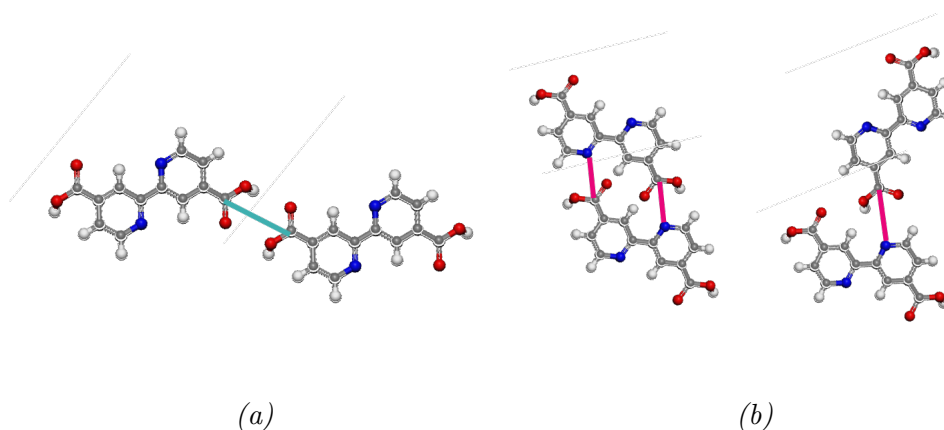
(a)

(b)

Figure 5.8: A further analysis of Figures 5.5 and 5.6, highlighting the suggested hydrogen bond relationship between molecules. Carboxyl to carboxyl bonds are coloured blue and carboxyl to nitrogen bonds are coloured magenta.

may meet but exist in different phases that may cause molecules on the edge of the network to switch rotation, and therefore domains.

Figure 5.9 show the proposed molecular layout explaining the bond colouration.



(a)

(b)

Figure 5.9: A molecular view of the highlighted bonds. (a) shows the carboxyl to carboxyl bond. (b) shows a carboxyl to nitrogen bond.

5.5 The Role of Hydrogen Bonding in Formed Networks

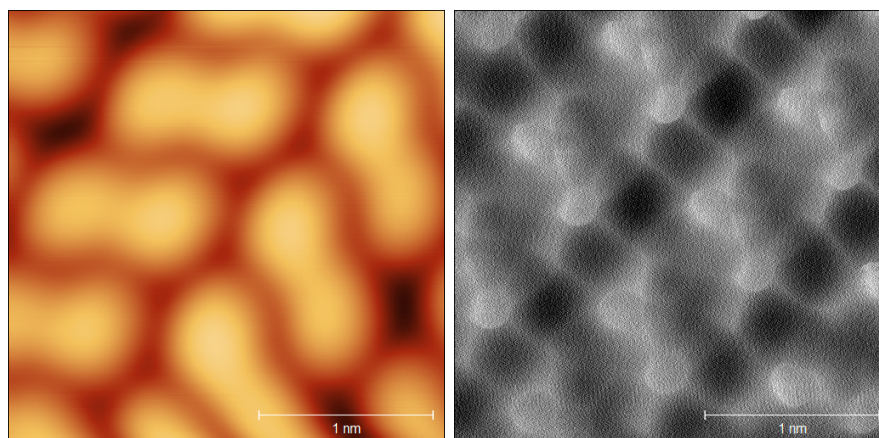
The presented NC-AFM scans show the underlying structure of the bi-isonicotinic acid molecule with its key features: the presence of two attached pyridine rings each with a carboxyl group.

Figure 5.10b shows scans obtained of the intramolecular structure in a resolution that is not afforded by the obtained STM scans. Figure 5.10c shows the structure of the bi-isonicotinic acid molecule for comparison. The structure imaged corresponds highly with that of the *trans* configuration of the molecule.

Several different arrangements of molecules were imaged under AFM in order to understand the underlying structures seen in the obtained STM scans. Figure 5.11 shows two NC-AFM scans where all of the imaged molecules have the same alignment, with two scans (a) being taken from a large tip-sample separation than that of (b). In order to illustrate the proposed molecular alignment unambiguously, (c) overlays the molecular model onto scan (a).

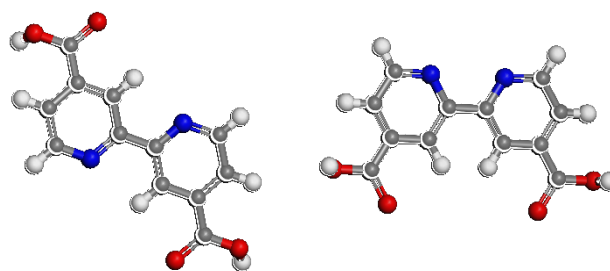
While the presence of hydrogen bonding is an inference from imaged data, an initial hypothesis can be drawn to the intermolecular bonds governing the formation of networks. Due to the highly mobile nature of the orientation of the H and OH branches of the carboxyl groups, the hydrogen has been omitted in this image so as not to imply accidentally any hydrogen bonding, however, the molecular alignment continues to support the idea of a nitrogen to carboxyl preference in inferred hydrogen bonds.

Figure 5.12 shows a set of scans around a small local region, though this time the STM scan, Figure 5.12a, suggested molecules of opposite chirality in the scanned area and so Figure 5.12 (b)–(e) show subsequent NC-AFM scans of the area around this STM scan, but are not all of the same area. Figures 5.12d and 5.12e show the presence of a possible carboxyl to carboxyl bond as opposed to the regular wholly carboxyl to nitrogen bond that is seen in Figure 5.12b



(a) STM, $2.5 \times 2.5 \text{ nm}^2$, $V = 3.0 \text{ V}$,
 $I = 50 \text{ pA}$

(b) NC AFM,
 $2.5 \times 2.5 \text{ nm}^2$



(c)

Figure 5.10: Two close scans of bi-isonicotinic acid on Au(111) showing a size comparison between the features in (a) STM and (b) NC AFM. (c) Shows the molecular structure of the bi-isonicotinic acid molecule for comparison. Left: the trans conformer. Right: the cis conformer.

It can be seen that there is a preference for molecules to align with those of similar rotational orientation and identical enantiomerisation. The figure highlights that while rows of these similarly oriented molecules are present, the rows can also alternate in chirality leading to a number of different possible arrangements. Carboxyl to carboxyl bonds were hypothesised in previous STM images, such as Figure 5.6. This arrangement was then imaged as can be seen in Figure 5.12 (c) – (e). It was decided to image this molecular junction in particular

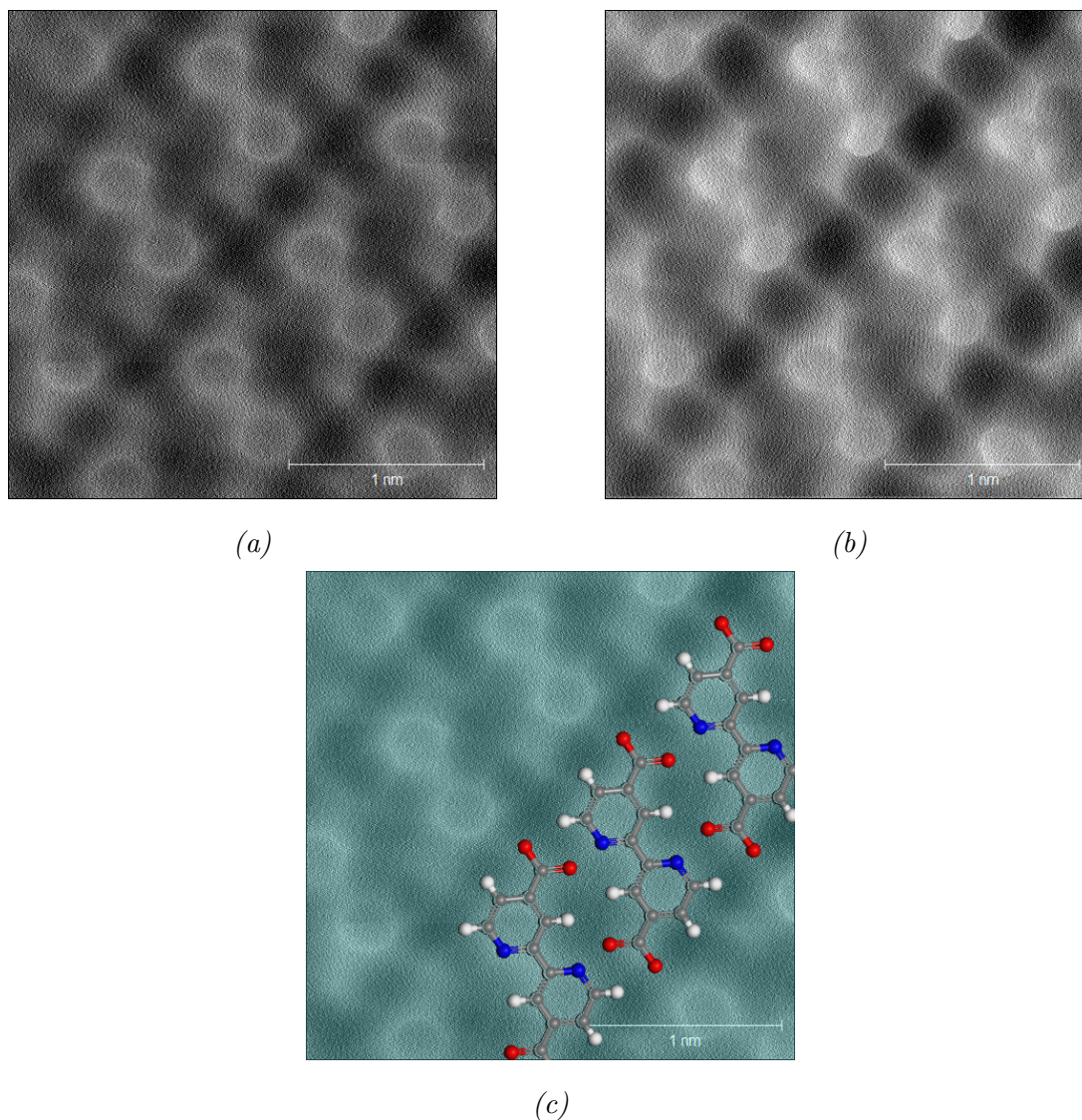


Figure 5.11: (a) and (b) are two NC-AFM scans at $2.5 \times 2.5 \text{ nm}^2$ taken at a greater and closer separation respectively. (c) Shows the bi-isonicotinic acid molecule superimposed onto a scan. The blue colouration of the scan has been chosen provide a better contrast between the scan and the molecule.

and so the scan area was directed to be directly over the carboxyl to carboxyl meeting between two molecules, this is shown in Figure 5.13, whose images are taken with a sequential reduction of the tip-sample separation.

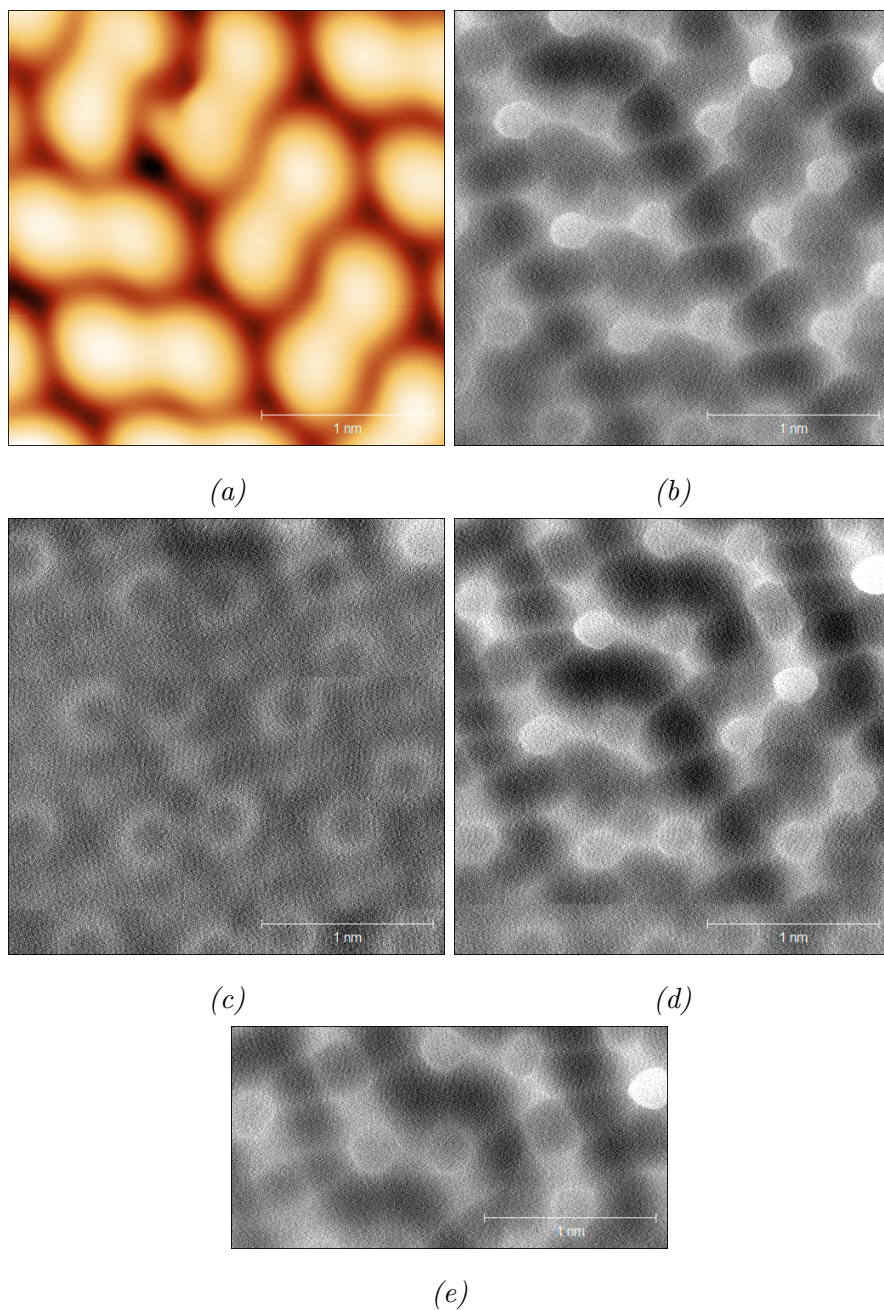


Figure 5.12: A set of $2.5 \times 2.5 \text{ nm}^2$ scans of bi-isonicotinic acid molecules of opposite chirality. (a) Is an STM scan of the area, (b)–(d) are NC-AFM scans of the same local area. (e) is an NC-AFM scan that focusses on the proximity of two carboxyl groups.

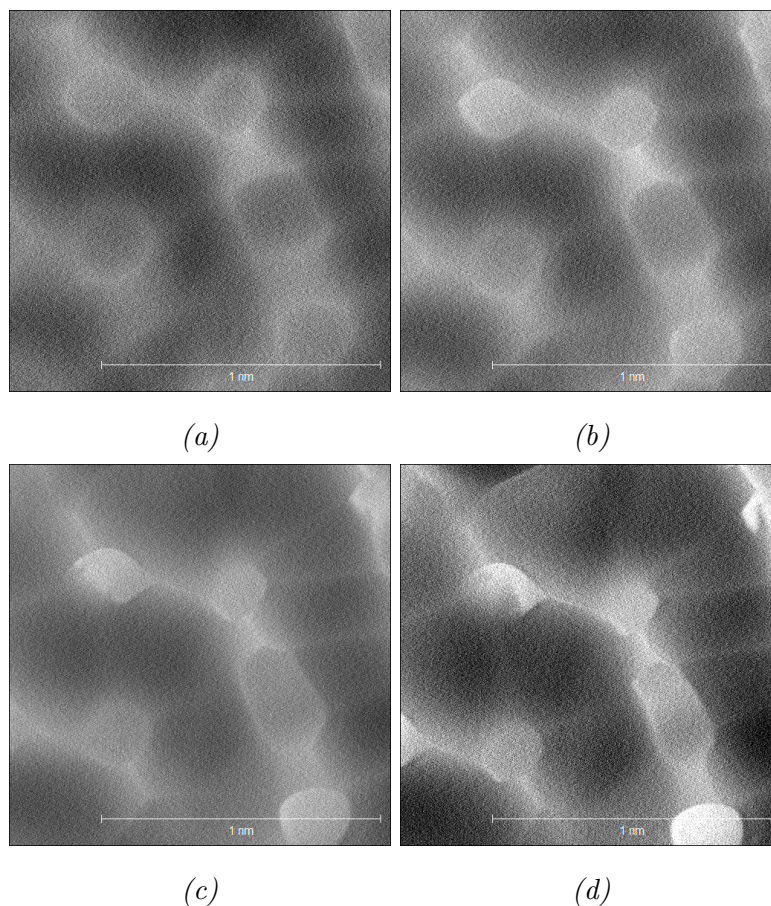


Figure 5.13: Four NC-AFM scans, $1.4 \times 1.4 \text{ nm}^2$ of a carboxyl-carboxyl junction in a bi-isonicotinic acid network. (a) – (d) shows a sequential reduction in tip-sample separation.

This imaging of the meeting of two carboxyl groups shows some striking features. The molecule appears increasingly bright, due to the increased repulsion caused by the closer tip-sample separation. Features of the molecules, such as the two pyridine rings appear increasingly asymmetric between (a) and (d) due to the increasing forces on the terminating apex of the tip. The scan also shows that the carboxyl to carboxyl junction images very brightly in a way that might be inferred as a direct connection between the two molecules. It is true that one carboxyl group will have affinity for another and many supramolecular assemblies are formed due to hydrogen bonding between these groups. The confirmation of

a hydrogen bond cannot be directly made but the location of the molecules with respect to each other in the images appears to support this hypothesis.

5.6 Network Boundaries of Molecular Assemblies

Thus far, discussion has focused primarily on the network structures of molecules within large networks on a flat surface. Experimental data were also obtained for molecules interacting with features of the surface itself, such as step edges, as well as data pertaining to molecules that lie on the edge of networks, thereby interacting with less of an energy minimum than those in the center of full networks.

Figure 5.14 shows a relatively large ($100 \times 100\text{nm}^2$) overview STM scan highlighting the behaviour of the molecular networks on a non-featureless Au(111) surface. The image shows step edges that provide boundaries in which molecular networks form. Of particular interest is a thin raised area that separates the lower planes. The image displays a feature that has been common in these scans, that is, the ordered molecules that appear to run parallel to the step edges. The behaviour of these molecules is different to the previously discussed two dimensional networks. Firstly, because there is a limit in the width of the network, which consists of rows of only two molecules. Secondly, because these molecules are confined to exist against preexisting features, that is, against step edges.

Figure 5.15 shows smaller scale scans that examine subregions of the overview image with a specific focus on molecules in networks defined by a step edge. In section 5.4, an effort to categorise molecules by their configuration was made, that is, into the *trans* and *cis* conformers. The hypothesised classification was marked in Figure 5.6, which inferred, which conformer was present by the shape of the molecule. Figure 5.15a shows a step edge network that meets a typical two dimensional assembly that has been previously discussed. The meeting points of

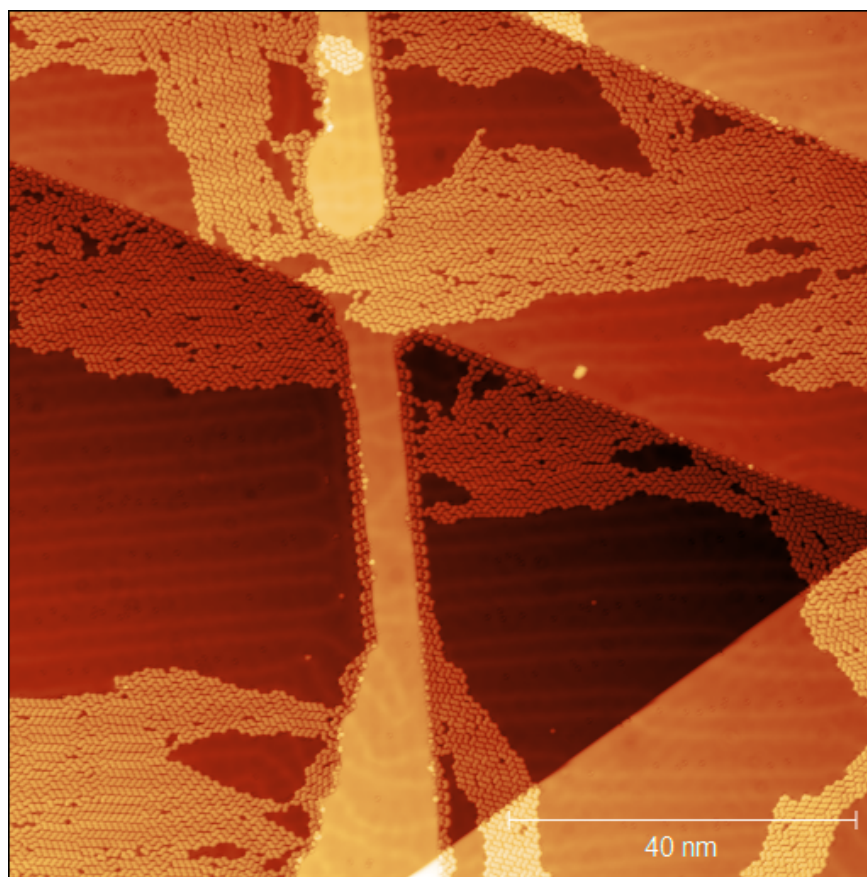


Figure 5.14: $100 \times 100 \text{ nm}^2$, $V = -0.5 \text{ V}$, $I = 10 \text{ pA}$

the two networks can be viewed on a larger scale in Figure 5.14, which shows that the typical assembly does interact with the step edge assembly but only through individual molecular interactions between the two, likely due to a sufficiently low local minimum in the potential landscape of the typical networks.

Figure 5.15b shows an isolated step edge network, highlighting the height difference between the two. This specific image was chosen to be the candidate for further NC-AFM imaging, though the specific scan requirements offered a modification of standard methodology. The easiest and most obvious experimental modification to make was to change the practice of taking square scans. Step edge networks, by their nature, contain two rows of molecules that are more self-contained than typical networks. While the interaction between these two domains did provide interesting experimental curiosity, it was much more prudent

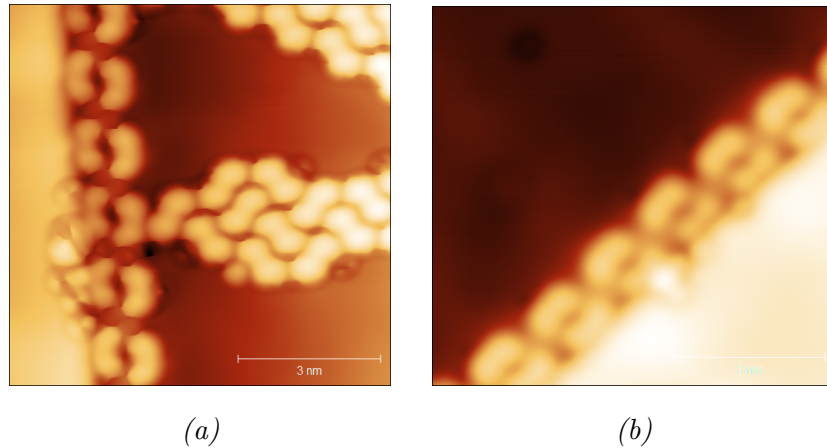


Figure 5.15: Two images focussing on local areas of interest from Figure 5.14.

$8 \times 8 \text{ nm}^2$, $V = -0.5 \text{ V}$, $I = 10 \text{ pA}$

to examine an isolated step edge network. The scan frame was therefore rotated and adjusted to a 2×1 ratio. This allowed the scan to be parallel to a step edge while not collecting data irrelevant to the desired scan area, that is, clean gold, which would dominate the scanned space. The second consideration was that NC-AFM scans are defined by their constant height relative to the sample. Hypothetically, a step edge network is an interesting region of study, while experimentally, a step edge presents a change in tip sample separation whose presence could obscure subtle changes in separation that define NC-AFM experiments. The choice was made, therefore, that while drift parallel to the network was deemed acceptable, drift away from the network or drift that incorporated the raised plateau of the raised part of the step edge would be limited.

Figure 5.15b shows another feature in addition to the step edge network and that is the presence of a bright feature in the STM image. The appearance of this feature is different to the scanned networks and additional CO adsorbates on the gold surface. This feature therefore should not be considered as experimentally deposited, however, it is still experimentally relevant. In such a clean deposition, this feature could be interpreted as a gold adatom, that is, an atom of gold that exists above the bulk and surface levels and functions as an adsorbate, free to

move around the surface but being relevant to the bonding structure of the subsequent deposition.

The area shown in Figure 5.15b was shown to be experimentally interesting and so the step edge network was imaged in NC-AFM leading to a collection of scans at increasingly reduced tip-sample separations as shown in Figure 5.16.

The scans under NC-AFM appear to support the hypothesis that step edge networks constitute an arrangement of the *cis* conformer. Also of note is the continued presence of bright protrusions, hypothesised to be adatoms of gold. As the tip-sample separation more of these adatoms appear within the molecular arrangement, though their positions do not follow a regularity. Their presence is therefore likely due to attraction into local energy minima, rather than a fundamental part of the structure of the network.

Figure 5.17, shows a wider NC-AFM scan showing a longer stretch of the step edge network. A schematic of the molecule has been overlaid to clarify the proposed structure that constitutes the network. The hydrogen atoms from the carboxyl groups have once again been removed so as not to imply hydrogen bonded structures. It is clear, however, the carboxyl groups of the molecule have an affinity for each other and likely define the double row structure of the step edge network.

The scans shown in Figure 5.17 show molecules arranging against a step edge, which is located parallel to the bottom edge of the scan. It has previously been remarked that bi-isonicotinic acid, specifically in its *cis* conformer, is a ligand in larger coordination complexes in ruthenium-based dye molecules. Thus, an affinity of the orientation for the transition metal surface, that is against a step edge, may arise in a similar manner that the previously mentioned coordination complexes do.

An interest had already been expressed in the imaging of the meeting of the two different network structures and the area shown in Figure 5.15a provided an ideal place to collect more NC-AFM data. While the images obtained of

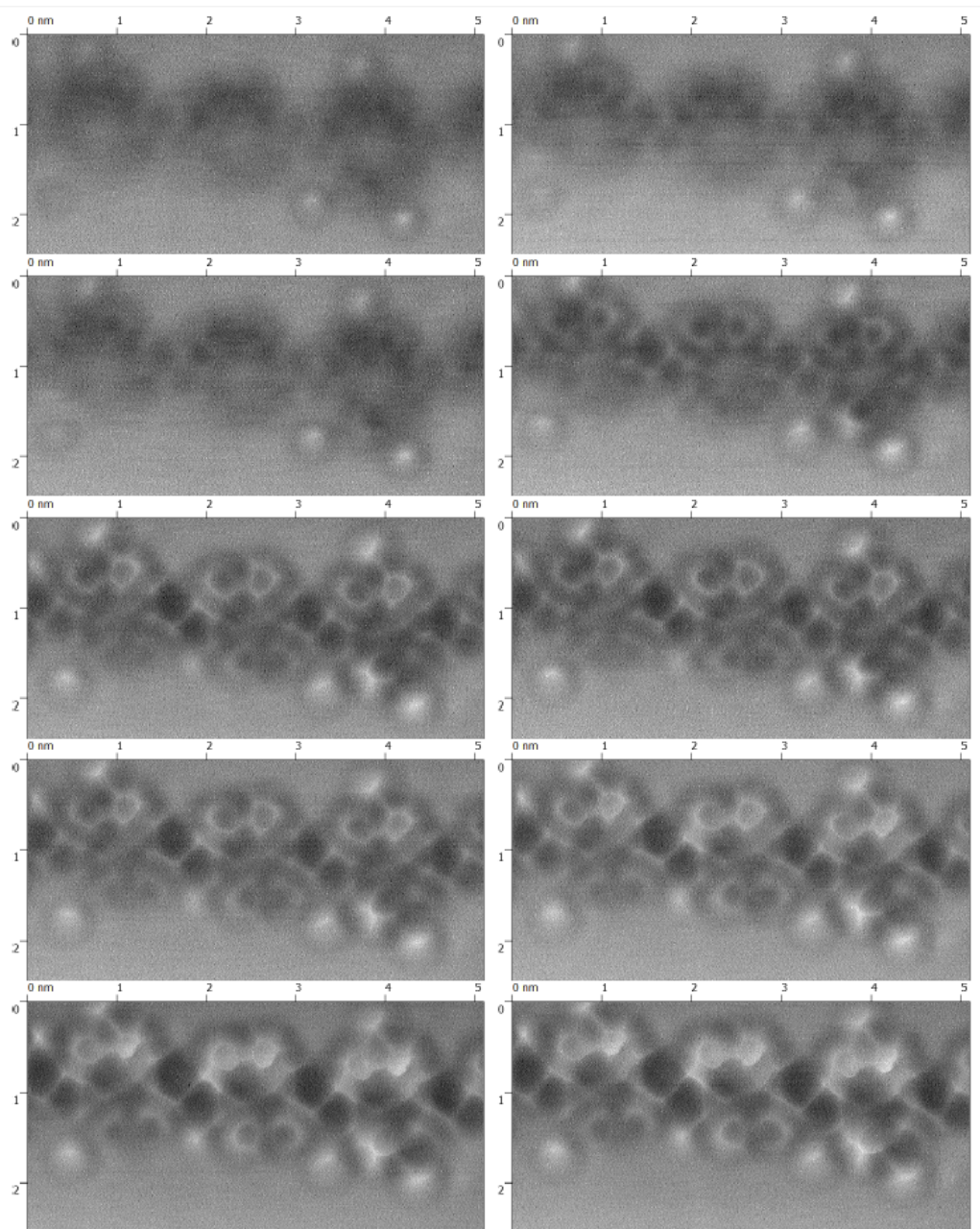
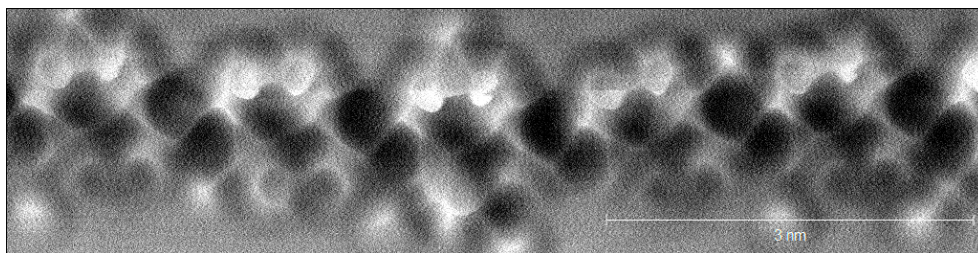


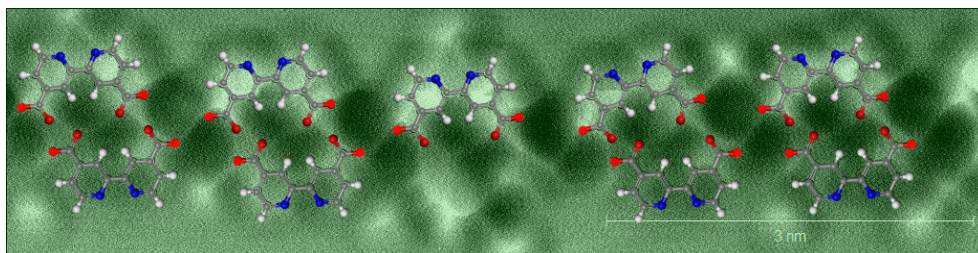
Figure 5.16: A collection of AFM scans taken in descending vertical height slices to better understand the bonding structure of the molecules.

$5 \times 2.5 \text{ nm}^2$

this network do not show the clarity of other NC-AFM images presented thus far, insight can still be obtained from the scan. Figure 5.18 shows the obtained



(a)



(b)

Figure 5.17: An NC-AFM scan with the proposed molecular structure overlaid. The green colour is once again to improve visual contrast. $8 \times 2.5\text{nm}^2$

scan and while the intramolecular bonds are not imaged as clearly as in some previous scans, the overall molecular shape is very striking. The network shows a mix of carboxyl to carboxyl junctions as well as carboxyl to nitrogen structures. The meeting of the two networks is formed by the meeting of a carboxyl group of the furthestmost constituent of the typical network meeting the side of the *cis* molecule of the step edge network that contains the two nitrogen atoms. It is unclear, however, whether there is an affinity for one or both of these atoms, whether there is a local energy minimum due to the presence of a general structure, or whether the position is simply geometric, that is, structure is formed purely from a tessellation.

5.7 Simulated AFM images

Section 3.6 provides a theoretical basis for the experiments conducted within this section. In order to further probe the understanding of image artefacts in

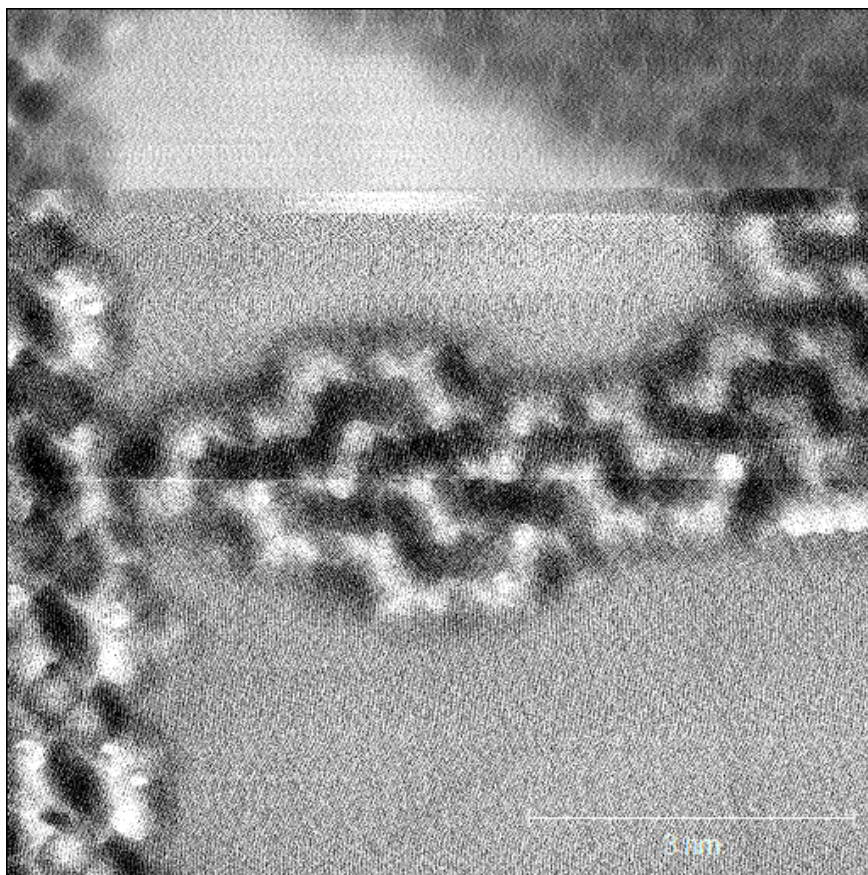


Figure 5.18: An NC-AFM scan showing the meeting of a step edge network and a typical network, $8 \times 8 \text{ nm}^2$

NC-AFM, it was extremely prudent to utilise the model proposed by Hapala *et al.* Figure 5.10 shows a collection of examples of a typical bi-isonicotinic acid network in a hypothetically hydrogen bonded arrangement. Artefacts exist between molecules, however, at sites that would not be expected to form the basis of a hydrogen bonded network. Naturally then, it is important to further understand the features imaged within the network. It was decided to simulate the placement of atoms that comprise the molecules on a surface with the distances determined from the NC-AFM scans directly.

Simulations within this section were conducted with the help of Abdur Rashid Mohammad, who conducted simulations to image bi-isonicotinic acid using the model proposed by Hapala *et al.*

Figure 5.19 shows a comparison between an experimental NC-AFM image of a typical molecular network and a simulated NC-AFM image of the same network using the model proposed by Hapala *et al.* It can clearly be seen that

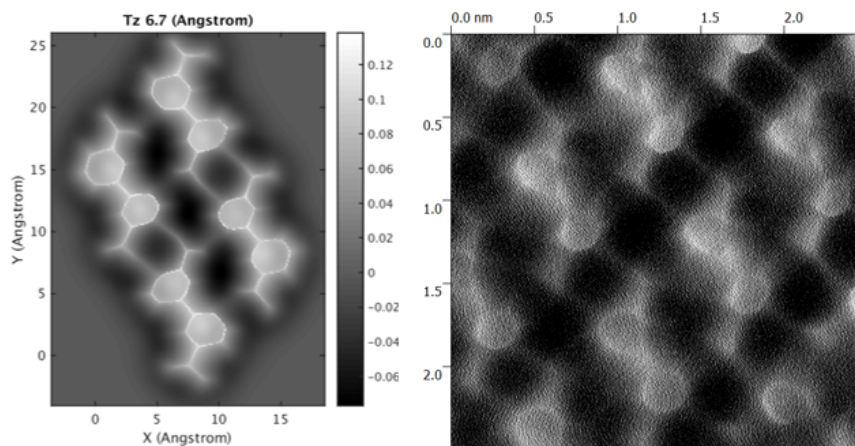


Figure 5.19: A comparison between (left) a simulated NC-AFM image created through the model proposed by Hapala *et al.*, and (right) an experimental NC-AFM image of a typical, aligned network of bi-isoncotinic acid.

features between molecules are present in the simulated image in positions where hydrogen bonding may be inferred. Interestingly, these features exist where hydrogen bonding is predicted likely, namely between the carboxyl group of one molecule and the nitrogen of the pyridine ring of another, but also where it is more suspect, that is, between the carboxyl group of one molecule and the hydrogens on the pyridine ring. The simulations show the importance of critical thinking when interpreting an image. The forces of hydrogen bonding between molecules is much weaker than the forces that hold the molecules together. When a suspected hydrogen bond appears on a scan, however, it is with an intensity comparable to the intramolecular bonds that constitute the molecule. Additionally, these apparent hydrogen bond features appear in simulations that do not take into account anything other than the forces acting on the simulated probe apex. The result agrees with interpretations previously proposed by Sweetman *et al.* [54] and Hämäläinen *et al.* [55] that artefacts that resemble hydrogen bonds

can appear on simulated images whose simulations do not take into account the interaction between atoms, only their position on a surface.

5.8 Spectroscopic Imaging of Bi-isonicotinic Acid Assemblies

As well as imaging bi-isonicotinic acid on a surface of Au(111), it was decided to also look at the molecular networks when deposited on a surface of Ag(100). The typical network structures formed on this surface are very similar to those of on Au(111) and shown in Figure 5.20.

Molecules were deposited on a surface cooled to 77K with liquid nitrogen and formed networks with fewer irregularities than those observed on the Au(111) surface, where several different tiling domains could be observed. Networks on the Ag(100) surface were uniform, consisting of the carboxyl to nitrogen hydrogen bonding solely and no carboxyl to carboxyl bonds.

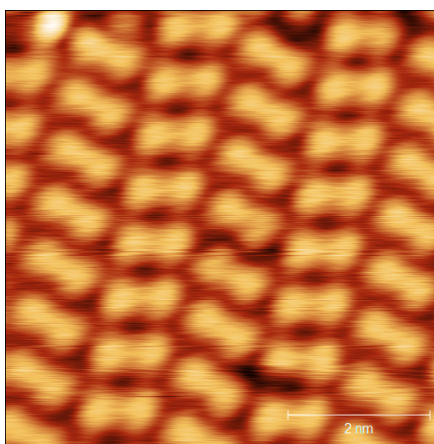
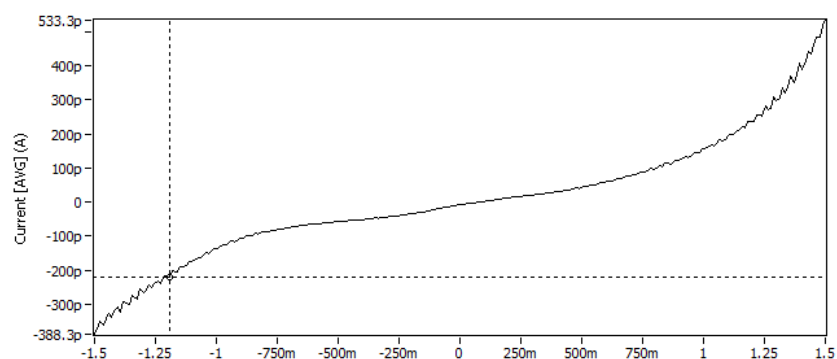


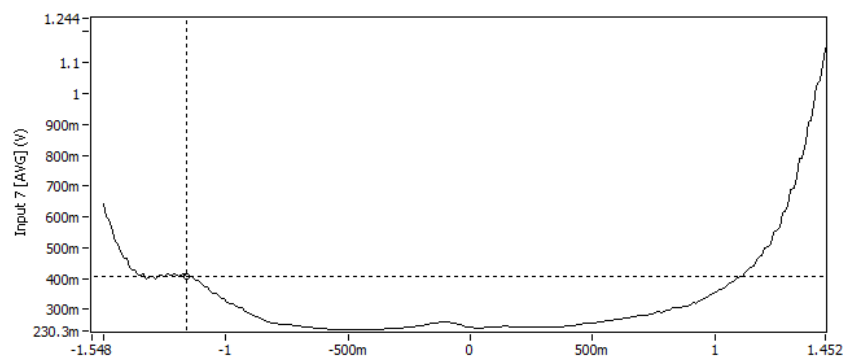
Figure 5.20: An STM scan of bi-isonicotinic acid on a surface of Ag(100), showing a typical regular network. $V = 1.5V$, $I = 50pA$, $6 \times 6nm^2$

It was decided to conduct a constant height STM scan of the network and, in order to do so, $\frac{dI}{dV}$ spectroscopy was conducted on a molecule within the network to determine any significant bias voltages with which to scan. Figure 5.21 shows

a spectrum taken by holding the tip at a fixed distance from the surface. The tip-sample separation was maintained by applying a compensation for thermal drift in the approach direction. The bias was then swept between -1.5 and $+1.5$ V. A peak was observed at -1.17 V corresponding to a significant energy level



(a)



(b)

Figure 5.21: Two spectra taken of the tunnel current between the tip and sample when the bias is swept between -1.5 and $+1.5$ V. (a) Shows the current $I(V)$ graph while (b) is its derivative ($\frac{dI}{dV}$)

for the molecule. The bias was then set at this value and constant height scans, together with $\frac{dI}{dV}$ scans, were taken above the molecular network. The resulting scan is shown in Figure 5.22.

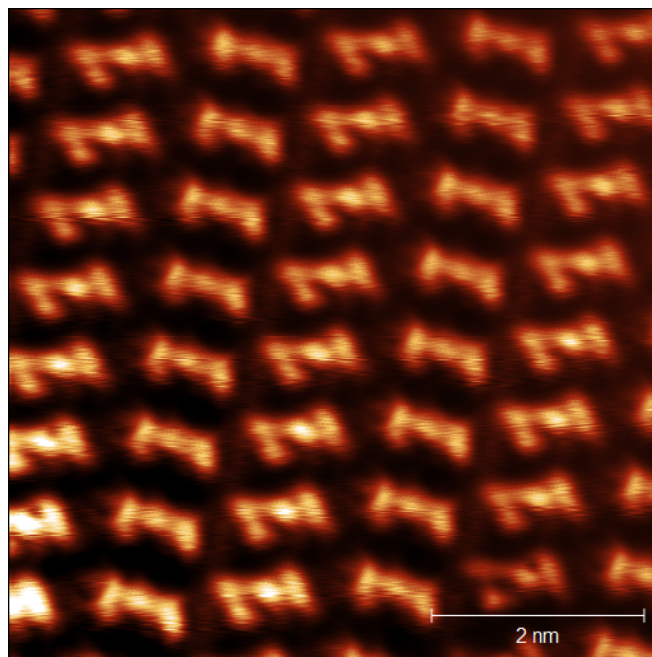


Figure 5.22: A scan of the $\frac{dI}{dV}$ signal of a constant height STM scan taken of bi-isonicotinic acid deposited on Ag(100). $V = -1.17\text{ V}$, $6 \times 6\text{ nm}^2$

5.9 Conclusion

Bi-isonicotinic acid has proven to have interesting properties when deposited on a surface of low reactivity. The nature of the formed molecular networks, is driven heavily by the bonding restrictions that the molecule has. While hydrogen bonding cannot be fully certain, specific locations of molecules with respect to each other in a network do imply the presence of such bonding. The specific location in question is the high quantity of carboxyl groups next to nitrogen atoms, or carboxyl groups next to other carboxyl groups.

It can also be seen that, when forming networks, the surface-induced chirality gives rise to conformer and enantiomerisation of the molecule on a surface. This means that bonding geometries are limited to either molecules of identical enantiomerisation and rotational configuration, or opposite enantiomerisation and a specific alternate rotational configuration. Islands which have different signa-

ture structures can meet but cannot combine neatly with each other causing the development of phase boundaries within networks.

When considering the *cis* conformer, it has a tendency to form networks along step edges consisting of two rows of the *cis* molecular configuration. It appears that the nitrogen atoms of one the *cis* conformer may have an affinity for the transition metal step-edge in much the same way that they form ligands in ruthenium dye complexes.

Simulations were also conducted to explore the nature of scan artefacts under NC AFM that appeared where hydrogen bonds would be predicted to be. These simulations using the model proposed by Hapala *et al.* recreated the same scan artefacts despite having no information on the underlying charge structure, merely the position of atoms in a molecule and its neighbours, with respect to each other.

Chapter 6

Monte Carlo Simulations

6.1 Monte Carlo Methods

To further investigate the assemblies of bi-isonicotinic acid, the decision was made to simulate the networks using Monte Carlo methods. The model used was based on the initial investigations by Stannard *et al.* discussed in Section 3.5 [40]. The initial consideration was formulated based on the similarity between the molecular geometry of bi-isonicotinic acid and the molecular tectons discussed in Section 4.3, particularly the **T1** molecule, shown along side bi-isonicotinic acid in Figures 6.1a and 6.1b. An overlay of a rhombus onto an experimental image is shown in Figure 6.1c displaying the initial consideration for how bi-isonicotinic acid could be represented in a tiling model.

6.1.1 Limitations of Initial Monte Carlo Model

It was recognised, while sharing similarities to the **T1** molecule, bi-isonicotinic acid would need to be modelled with further considerations based on molecular structure and experimentally observed behaviour. One of the most obvious differences between the two molecules is the absence of two of the four carboxyl groups present on the **T1** molecule. This leads to important considerations that neces-

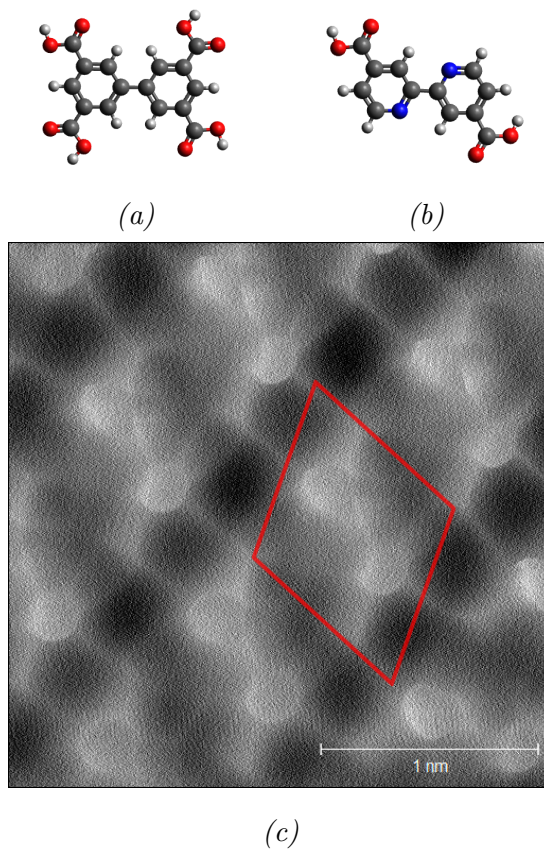


*Figure 6.1: An image showing the initial assumptions of a bi-isonicotinic acid tiling model. A comparison of (a) the **T1** tecton and (b) the bi-isonicotinic acid molecule showing their similar molecular structures. (c) Shows the overlay of a rhombus on an experimental NC-AFM image.*

sitate the modification of the tiling model. A tile must have fewer symmetries than those used to model tetracarboxylic tectons. The surface induced chirality of bi-isonicotinic acid means that the symmetry of reflection is not present. This consideration further implies that while previously tectons have been modelled with three orientations of tile representing different rotations of the molecule, bi-isonicotinic acid must be modelled with six different tiles, representing both the rotations and the reflections of the molecule.

The need to account for the chirality of the molecule provided further need for the modification of the initial tiling model. In initial considerations, the four

edges of a rhombus tile would be considered as equivalent to each other with the energy considerations of the molecule defined by a localised hamiltonian:

$$E = -\epsilon \sum_{\langle ij \rangle} n_i n_j + \mu \quad (6.1)$$

where ϵ represents the relative strength of interactivity between neighbouring sites, μ represents the chemical potential of the site itself and n_i and n_j represent the occupation of neighbouring sites by other molecules, which would lower the potential energy experienced by a molecule occupying a given site. The introduction of chirality and the need for edges of rhombi to represent different molecular features necessitated more than a simple consideration of whether neighbouring sites were occupied. The energy considerations also needed to take into account *what* was occupying those sites.

Experimental observation discussed in chapter 5 informed further modifications to the initial tiling model. One of the most important limitations of the initial model was the presence of an offset between rows of molecules, as illustrated in Figure 6.2. While molecules arranged themselves in row structures, it was clear that the pyridine rings of one molecule would appear aligned with the carboxyl groups of the molecules on neighbouring rows.

The observed half-molecule offset between rows meant that the consideration of a molecule as a single rhombus modelled on a triangular lattice was impossible. The model was not abandoned, however, as it was concluded that an effective representation of the tiling of bi-isonictonic acid could be built upon the rhombus tiling principles.

6.1.2 Proposed Molecular Tiling Structure

In order to revise the initial tiling model, a representation of a triangular lattice was overlaid onto obtained experimental data as shown in Figure 6.3. It was

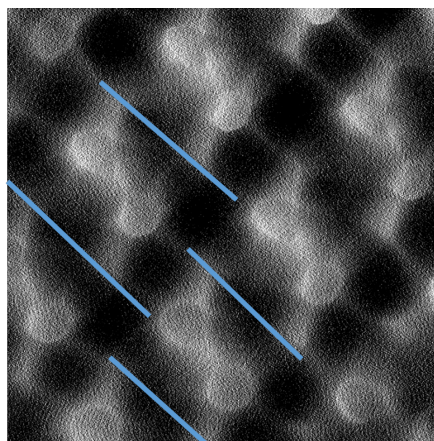


Figure 6.2: NC-AFM image of bi-isonicotinic acid molecule with blue lines indicating an offset in alignment between rows of the molecule.

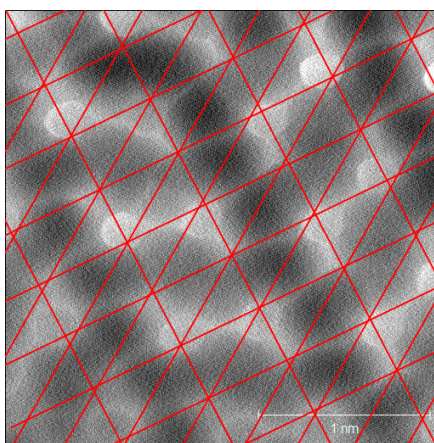


Figure 6.3: A triangular lattice in red is overlaid onto an NC-AFM scan

recognised that if triangles could be utilised to reconstruct experimental data, the triangular lattice and principles of rhombus tiling could still be of use.

The overlaid triangular lattice suggested that the vertices of triangles would represent significant points of the molecule rather than the edges, which were utilised in modelling of tiling tectons. A molecule was then formed through the combination of three rhombi, allowing for the modelling of chirality and a geometry that could allow for the half-molecule offset as observed in experimental scans. This refined model is illustrated in Figure 6.4, where the molecules have been grouped with those of the same chirality. As with the initial Monte Carlo

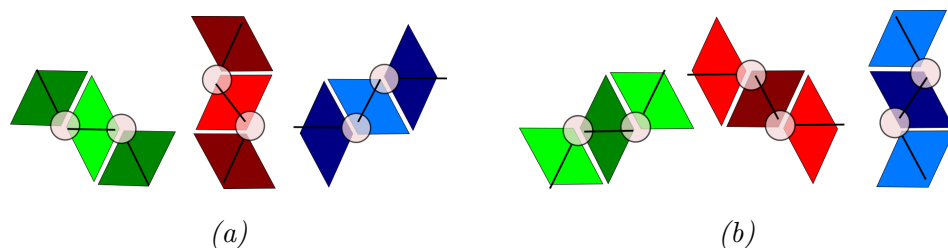


Figure 6.4: The proposed molecular model constructed of three rhombi to represent a single bi-isonicotinic acid molecule. A skeletal approximation of the molecule is overlaid for clarity.

model discussed in Section 3.5, it was realised that a molecule’s structure could be understood from a single point of occupation within a matrix. In the model of a single rhombus, only the up-facing triangles on a triangular lattice needed to be considered and the down-facing triangles could subsequently be inferred. The same principle was applied further by modelling a molecule as the middle rhombus of the three and inferring the outer two subsequently.

To model the energy landscape of the molecule, the bonding geometries were defined using the assumption that molecules would only bond with those whose outer two rhombi were of the same form as each other. The allowance of only these tiling junctions can be understood as the alignment of the carboxyl groups of two molecules, or as the alignment of a carboxyl group with the location of a nitrogen atom on a pyridine ring. Examples of these bonds are shown in Figure 6.5.

6.1.3 Modification of Experimental Algorithms

Simulations conducted by Stannard *et al.* reproduced the effect of molecules adsorbing onto or desorbing from a surface with a liquid film deposited on it [40]. The model simulated the effects of molecules in solution that would form assemblies in energetically-favourable, localised clusters on a surface. The algorithm would inspect a random site on the surface and place, alter, or remove a tile

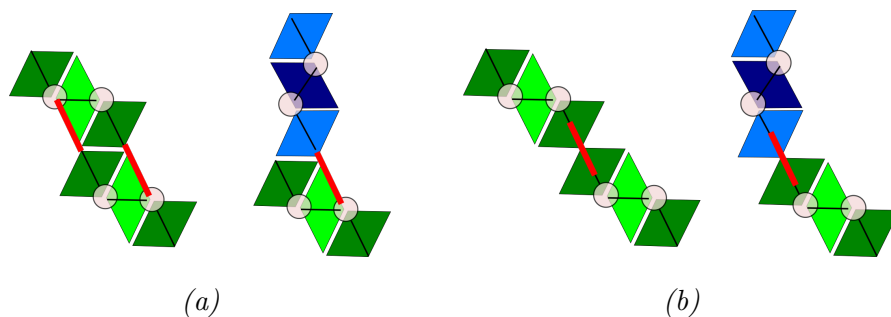


Figure 6.5: Examples of allowed bonding configurations within the simulated networks. (a) Represent a carboxylic to nitrogen hydrogen bond. (b) Represent a carboxylic to carboxylic hydrogen bond.

based on the Boltzmann weights of each state. Whilst the Boltzmann weights are likewise considered in the formation of the experimental algorithm used in bi-isonicotinic acid simulations, the algorithms used are slightly different.

The initial stage of the simulation functions as a simulated deposition. Once a concentration of molecules is specified along side the size of the lattice, the appropriate number of tiles are placed. A random orientation and surface-induced chirality is chosen and then this molecular tile is placed randomly with only consideration on whether the molecule will fit and no initial calculation of how energetically favourable the simulated molecule's position will be.

Once the surface is populated, rather than considering a random site, a random *molecule* is considered. It is then the motion of this molecule that is determined, based on similar principles to those of the heat bath algorithm. In this model, the modification of a molecule has nine possible states. These states are represented through either a molecule's translation to one of the six nearest neighbour sites of a triangular lattice, a molecule's rotation by 60° or a molecule remaining in place. The representations of the modifications to a molecule's state are represented in Figure 6.6. Molecules are not allowed to switch the defined chirality once they are deposited as this would require much larger energies in reality to lift the molecule and flip it.

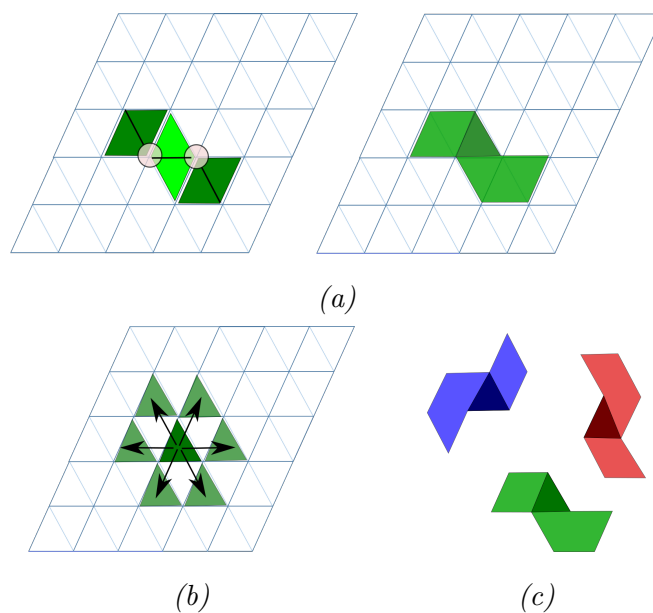


Figure 6.6: (a) Shows the representation of a molecule on a triangular lattice, both the skeletal model overlaid on the rhombi, and a representation the key lattice site that defines the position of the molecule. (b) Shows how the key lattice site has six nearest neighbour translation options. (c) Shows the key lattice site highlighted and permitted rotation options available for the molecule.

The Boltzmann weight of all of these states are calculated and then a random number is generated. As in the Heat Bath algorithm, the possible states of the molecule are appropriately weighted and the random number is compared with the weights, as described in Section 3.5.3 in order to modify the molecules state within the simulation. Molecular coordinates are stored within an array so that each molecule's state can be visited, rather than inspecting random sites. Molecules are visited in a random order, however, so that any emergent behaviour will not emerge due to the order of consideration. A Monte Carlo sweep in this algorithm is defined as a number of random inspections and state modifications equal to three times the number of deposited molecules.

6.2 Tiling Regimes of Simulated Molecules

6.2.1 Simulation Parameters

In order to consider possible final lattice states, it is important to understand the variables that ultimately govern the simulations' evolution. The energy of a molecule in a given lattice site is:

$$E_s = -\epsilon_1 \sum_i n_i - \epsilon_2 \sum_j n_j + \mu, \quad (6.2)$$

where E_s is the energy of the state, ϵ_1 is the bonding strength between molecular neighbours due to a carboxyl to nitrogen hydrogen bond, ϵ_2 is the bonding strength between molecular neighbours due to a carboxyl to carboxyl hydrogen bond, and μ is the chemical potential of the lattice. n_i and n_j represent the number of nearest neighbours that can undergo their respective bond types.

Due to the fact that once molecules are deposited, they cannot leave the surface, μ becomes common to all simulated molecules and will not drive the evolution of the system. The absolute strengths of the ϵ bonds are important, however as a stronger bond will fix emergent networks in place. The relative strengths of the ϵ_1 and ϵ_2 bonds are also relevant as if one type of bond is stronger than the other, it is likely to lead to emergent behaviours within networks. It was decided that the absolute strength of the bonds would be a parameter of interest, whereas altering the relative strengths could be the premise for future simulations.

As well as altering the relative bonding strengths, the kinetic energy of the molecules can also be varied. The Boltzmann weight of a molecule is given by the equation:

$$S = e^{E_s/k_B T}, \quad (6.3)$$

where S is the Boltzmann weight, k_B is the Boltzmann constant and T is the temperature of the system. By increasing the temperature in the system, molecules

gain more effective kinetic energy which reduces the probability that they will be fixed into network. This parameter creates an interesting phenomenon in that with an increase in kinetic energy, molecules can remove themselves from an effective local energy minimum and are, therefore, more likely to tend to a global energy minimum of the lattice, given enough time. With too much kinetic energy, however, bonds will be continually made and broken resulting in an unbound phase.

A final parameter of interest is the concentration of molecules deposited on a surface. Molecular domains will form with different primary orientations on the surface and the growth and evolution of these domains will be driven by the concentration of molecules. Small isolated domains will simply accrue the limited number of remaining molecules that may be unbound, but the domains are unlikely to meet each other and hence the final state of the lattice will continue as small isolated domains. With a high concentration of molecules, domain boundaries are like to meet and the molecules on the boundary are free to switch between similar local energy minima at the edge of each boundary. The resulting lattice evolution sees certain domains to acquire the molecules of others and hence grow larger while reducing the size of others. This may be driven by more energetically favourable conditions in one domain over another, or can simply be a consequence of statistics. Over time this domain coarsening will be much more present in lattices with high molecular concentrations.

6.2.2 Simulation Results

A large number of simulations were required to produce a statistically relevant set of results. Of the tested parameters, concentration is the most simple to interpret visually. Concentration is measured in units of monolayers (henceforth ML), where one ML represents the coverage of every possible lattice site with a molecule. Concentration was varied in twelve equally spaced steps between 0.1ML and 0.8ML. Concentration variation limited below 0.8ML due to the way

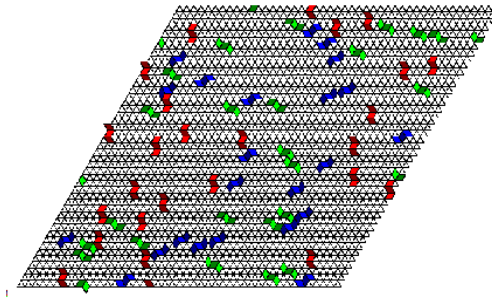
model is enacted. Within the model, 1ML is defined such that every triangular site in the lattice is occupied. During initial placement of molecules, they are placed randomly and, as the system has not had time to evolve, it may not be possible to place additional molecules as vacant spaces need to consist of several rhombi in set configurations.

Both bonding strength and temperature are measured in arbitrary units as their absolute values are not as important as their value relative to each other. Higher numbers for temperature correspond to hotter systems, that is, systems with more kinetic energy. Higher numbers for the bonding strength correspond directly to the strength of the bond, with a higher number leading to a stronger bond. ϵ , the strength of the molecular bond was taken at twelve equally spaced values between 0.1 and 2, temperature was taken at twelve equally spaced values between 0.1 and 1.

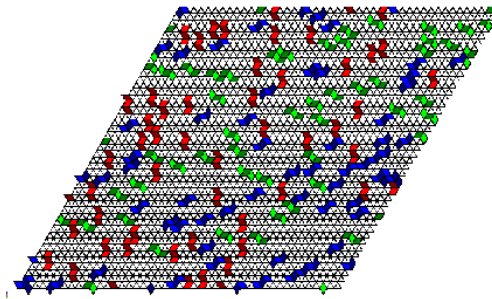
For each of these individual parameters, 100 repetitions were performed as, due to the random nature of Monte Carlo methods, no individual final lattice state would be representative of a set of parameters, but rather the statistical tendencies of multiple simulations using the same parameters would be of much more significance. A number of different final lattice states were observed after running the simulations for 10000 Monte Carlo sweeps.

Unbound States

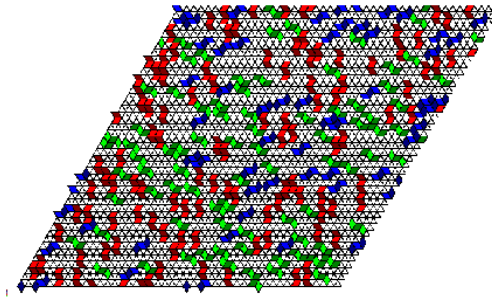
The most straightforward state to recognise is the unbound lattice. When the temperature of a system is sufficiently high, no stable networks can form between molecules. Figure 6.7 shows the final states of lattices with a low binding energy and high temperature at concentrations of 0.16ML, 0.35ML and 0.55ML. In these simulations it can be seen that molecules do not lie in any predictable arrangement. The kinetic energy of the molecules is high enough to prevent any structures from forming. As an unbound state arises to a temperature that allows



(a)



(b)



(c)

Figure 6.7: Unbound final lattice states of concentrations: (a)0.16ML, (b)0.35ML and (c)0.55ML

binding to be surpassed, it is useful to do some statistical analysis to quantify which parameters lead to bound and unbound states.

The model that defines how simulated molecules have an affinity for each other allows for both carboxyl group to carboxyl group bonding and carboxyl group to nitrogen atom bonding, thus each molecule has four potential bonding

sites available to it. A simple value can then be calculated for each molecule:

$$N = \frac{\sum n_{\text{bonds}}}{n_{\text{mol}}}, \quad (6.4)$$

where N is the bonding value, n_{bonds} is the number of bonds between molecules observed due to placement and n_{mol} is the total number of molecules on the lattice. If, on average, there is at least one bond per molecule, that is $N \geq 1$, the lattice could be considered in a bound state where kinetic energy has not overcome the formation of small localised molecular clusters. Thus, for a given concentration, a phase space map can be produced between ϵ , the molecular bonding strength, and T , the temperature of the lattice. A selection of these phase space maps are shown in Figure 6.8 for different concentrations of molecules. The number in each square corresponds to the average number of bonds per molecule, N , and the red colour allows for a visualisation of this number using an opacity that corresponds to N , where fully opaque would mean that all molecules have bonds at all four of their bonding sites.

Bound states

When the number of bonds per molecule, N , is one or greater, the lattice can be considered in a bound state. Bound states are lattices that contain molecular islands of varying size. The primary interpretation of N has been used to determine if the lattice is in an unbound state. For values of $N \geq 1$, however, a further inference can be applied. The value of N also represents the size of molecular islands within the simulation. Smaller but more numerous islands will lead to a lower number of average bonds per molecule in a given lattice, whereas fewer larger islands will represent a lattice that has coarser domains. The limiting number of an average of four bonds per molecule will not be achieved in any simulation in practice as it would require every molecule to be bonded at all four sites with no exceptions. As concentrations of molecules are always below 1ML, there will always be molecules on the edge of island structures which do not have all four bonds completed and thus a value of $N = 4$ is impossible.

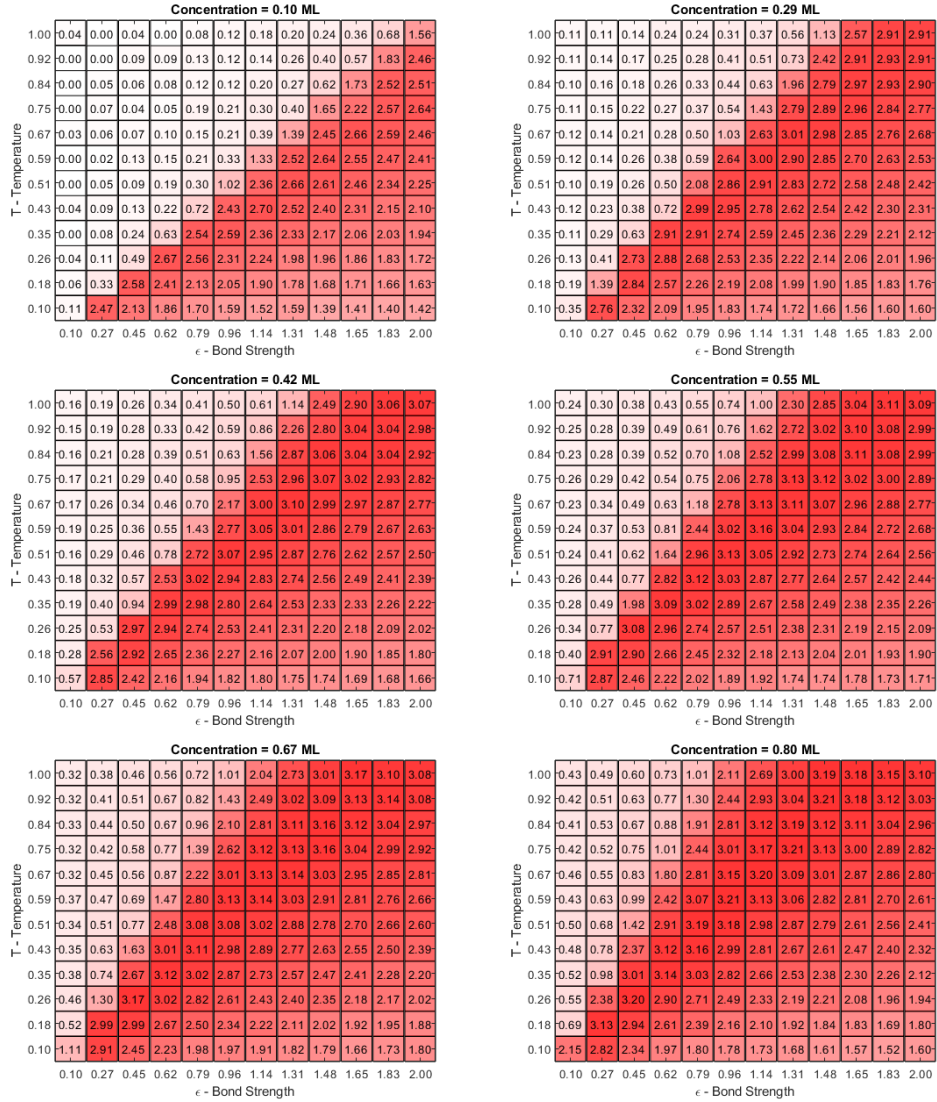


Figure 6.8: Phase space maps of different concentrations of molecules showing the number of bonds per molecule N for different values of bond strength, ϵ and temperature, T .

For each value of bond strength tested, there will be a critical temperature at which N is maximum. Below this temperature, islands remain in a stable configuration where individual molecules may reconfigure themselves out of the local minimum, due to the random nature of the Monte Carlo algorithm. Above this critical temperature, however, islands can still form but the molecules that define the outside of the island are in a much more dynamic state, effectively

diffusing between islands in a manner similar to experimental images seeing extraneous molecular movement such as those seen in room temperature scans of bi-isonicotinic acid on Au(111). Figure 6.9 shows a progression of scans at fixed concentration and bond strength but with increasing values of temperature to illustrate the relevance of the critical temperature.

The critical temperature of the simulated scans presented in Figure 6.9 is at $T = 0.59$, where the average number of bonds per molecule is $N = 3.05$. As temperature increases up to this critical temperature, molecular islands get larger and coarser with all molecules bound in a network. As temperature increases above this critical temperature, domain size begins to reduce as individual molecules become free to diffuse between islands.

While the number of bonds per molecule is a useful figure to compare simulations, other associated figures relating to the final lattice can be of equal value. As well as counting bonds generally between molecules, there are different molecular bonding configurations, thus, the number of carboxyl to nitrogen bonds can be counted and compared with the number of carboxyl to carboxyl bonds. A preference score for a given bond type can be defined using the ratio:

$$P = \frac{\sum n_{\text{OH-N}} - \sum n_{\text{OH-C}}}{\sum n_{\text{bonds}}}, \quad (6.5)$$

where P represents the preference score, $n_{\text{OH-N}}$ and $n_{\text{OH-C}}$ is the number of carboxyl to nitrogen bonds and carboxyl to carboxyl bonds respectively, and n_{bonds} is the number of total bonds formed in the lattice.

It can be seen in simulated scans that coarser domains tend to show a large number of like orientated molecules and so this, too, can be interpreted as a measure of order within the simulations. The preference score, therefore, represents a level of organisation or order within the final state of a simulation. Figure 6.10 shows the difference between the level of order within networks. As domains get coarser, the regions within the domain also coarsen with a preference being given to nitrogen to carboxyl bonds over carboxyl to carboxyl bonds. This preference is characterised by a molecule's neighbours being of like orientation and chirality.

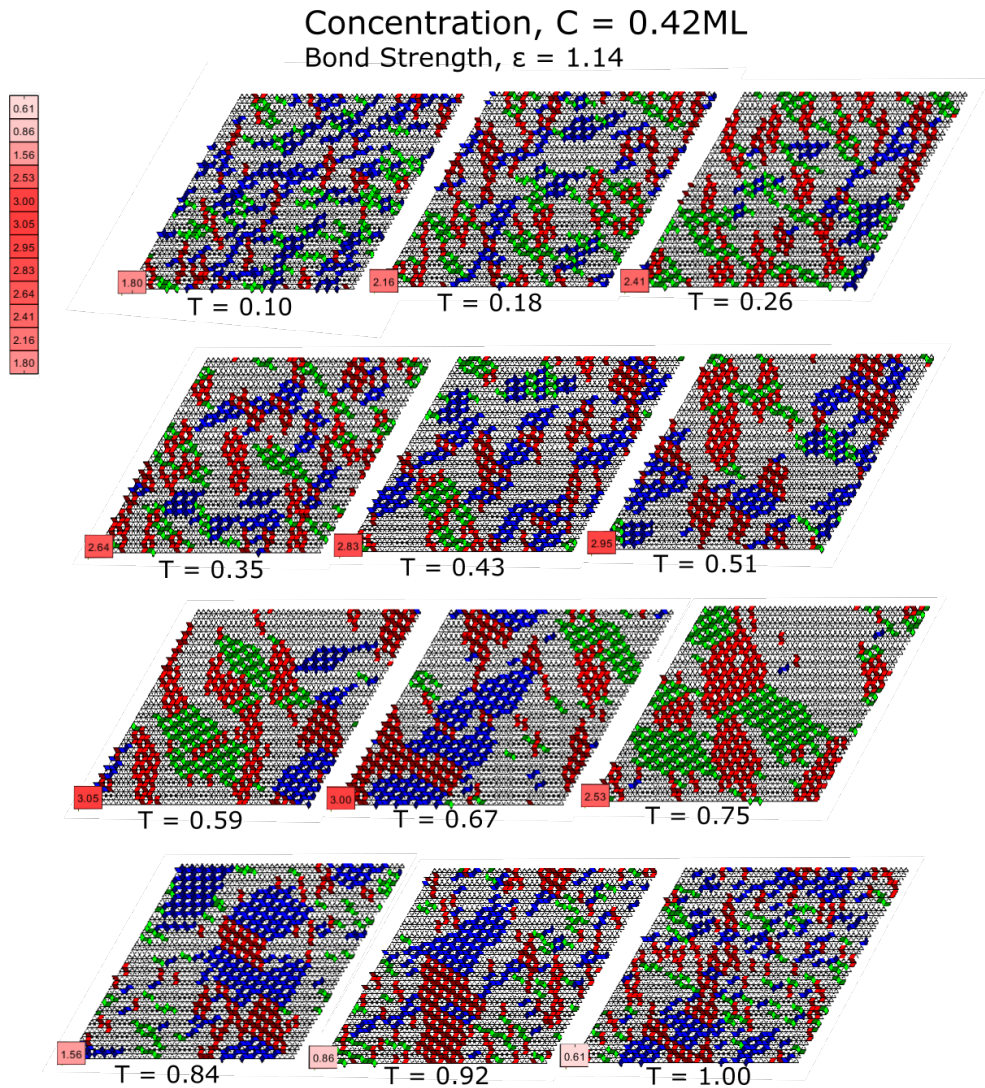


Figure 6.9: A progression of scans at fixed concentration and bond strength but with increasing values of temperature. Each simulated lattice is presented along with its number of bonds per molecule, N . Scans shown are individual results from simulations, whereas the values for N are the statistical average of all final state lattices in the category.

The preference score, P , will be higher for a greater number of molecules with neighbours of a like orientation. The score should be considered as a spectrum with no physical significance being attributed to the absolute value of P . It is prudent to visualise the proportion of each type of bond in another phase

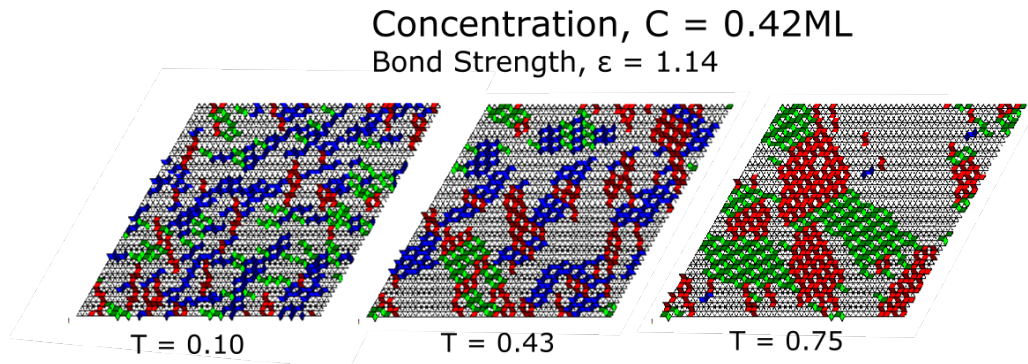


Figure 6.10: Examples of bound networks from simulation with increasing temperature leading to coarser domains and a higher number of molecules with similarly oriented neighbours.

space diagram. The phase space diagram is coloured using a red colour whose opacity is a measure of the average number of nitrogen to carboxyl bonds per molecule, and a green colour whose opacity is a measure of the average number of carboxyl to carboxyl bonds per molecule. Phase space diagrams of this kind for multiple different concentrations of molecular deposition are shown in Figure 6.11, with the associated number being the preference score, P . The colouring of squares and the associated number are only plotted for those lattices which exist in a bound state as the numbers for the unbound state will effectively arise only within statistical noise.

The phase space maps show a similar evolution of preference score, P , arising from the relationship between temperature and bond strength as given by N . That relationship is that namely there exists a certain critical temperature for each given value of bond strength. The preference for nitrogen to carboxyl bonds over carboxyl to carboxyl bonds increases up to this value. Subsequently, above this critical temperature, the number of both types of bond decrease as the lattices enter a more diffuse nature.

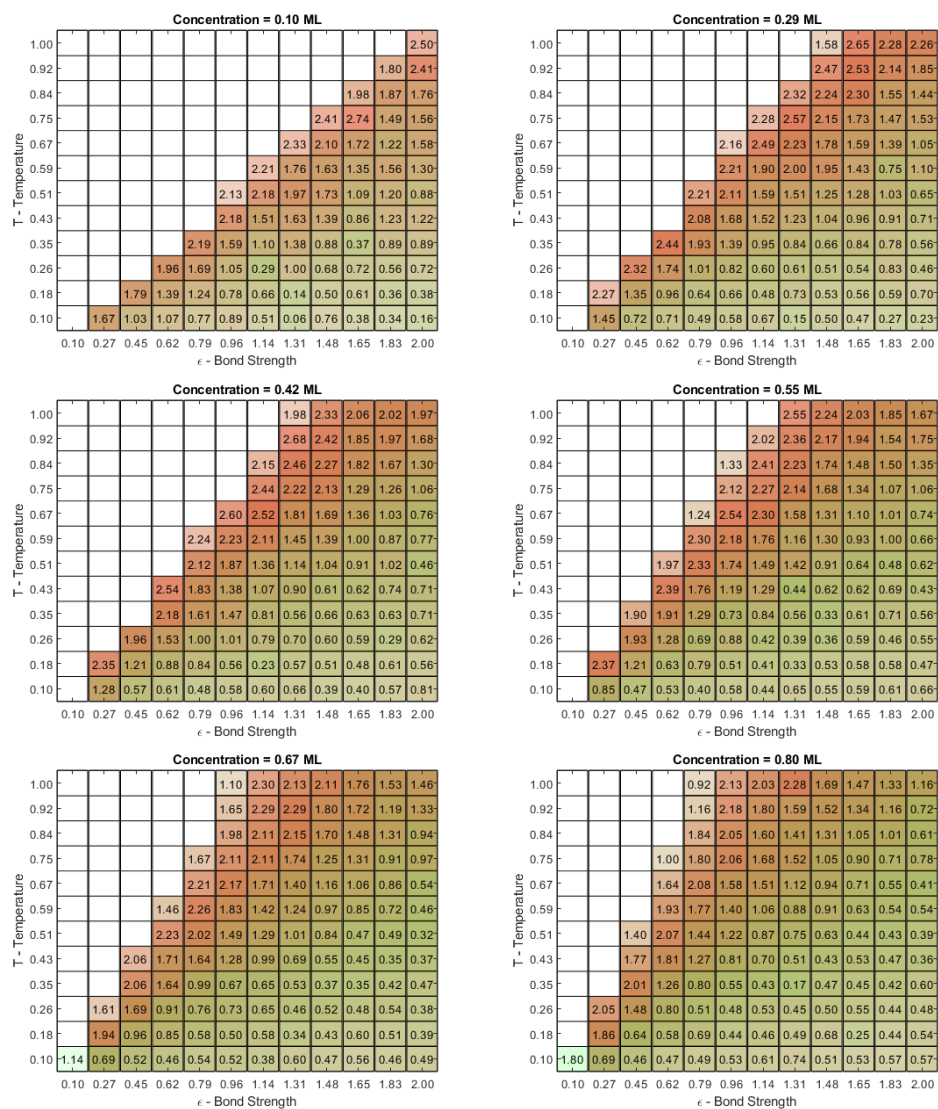


Figure 6.11: Phase space maps of different concentrations of molecules showing the preference score, P , for different values of bond strength, ϵ , and temperature, T .

Chapter 7

Categorisation of Assembly Regimes with Machine Learning

7.1 Motivation

Image analysis is a key component in the field of SPM, however, the field, by its nature, contains several obstacles to analysis. Data acquisition can frequently be a slow process, interpretation of the images acquired can require high levels of esoteric knowledge, and large quantities of data may have to be collect, many of which are not significant.

It was decided to explore the possibility of using machine learning on the simulated results of Chapter 6, in order to explore two uses of machine learning with regards to molecular networks. The simulated networks were chosen as large amounts of data could be generated that could map into an SPM acquired image.

The first of the two uses was the feasibility of using machine learning to determine the parameters that an experimental parameters, that is the temperature, bond strength or concentration, from the final state lattice. The second of the two was designed to measure how successful machine learning could be at applying categorisation to networks from their final state lattices.

Experiments in this section were conducted with the help of Oliver Gordon who was heavily involved in designing a lot of the machine learning architecture and also helped with the implementation

7.2 Neural Networks Background

In the most simple interpretation, a traditional computing algorithm takes a set of inputs and follows a number of predefined instructions to convert these inputs to become set of outputs. The outputs can manifest in many different ways, such as numerical or graphical information or even information that can be subsequently be used as an input in a more complex string of algorithms. For many computing tasks, the traditional algorithm is more than adequate, however, for certain tasks it is incredibly limited. This limitation can arise from many places, for example, the amount of input information may be impractical to consider or the number of actions within an algorithm may be so large as to become unfeasible to program. An example related to the latter case would be a layer of simple unrelated decisions. A single binary decision may then necessitate two unrelated binary decisions depending on the outcome of the first. With each additional layer of decisions, considerations grow exponentially and thus become impractical to program.

By design, the instructions that constitute the traditional algorithm are all specified by the algorithm's architect and are subsequently fixed. Tasks that require a level of adaptability, however, can utilise the concept of machine learning. Machine learning forgoes the idea of a list of set instructions and instead allows a specific network to learn to perform a task. This is useful for tasks that may be typically more subjective such as image recognition or categorisation.

7.2.1 Evolutionary Algorithms

In order to understand the construction and utilisation of a neural network, it is first useful to understand evolutionary algorithms. An evolutionary algorithm provides the foundation for adaptability utilised in machine learning scenarios. The construction is inspired by the process of evolution through natural selection.

In the most crude biological understanding, evolution through natural selection occurs on a genetic level. Living creatures contain genes, which are essentially a set of instructions informing individual structures on how to grow and, to a certain extent, how to behave. As living creatures have offspring, their genetic material is passed on so that the offspring's genes are defined by the parent, sharing their genetic material. As these genes are passed through successive generations, however, the process for copying the genes from parent to the offspring is subject to imperfections. As such, small mutations can occur in the genes between generations. These mutations change the development of the creature, either physically or mentally in a random fashion.

Although development of new traits occurs randomly in offspring, those traits that are detrimental to survival in a given environment will cause that offspring to be less suited to that environment. Consequently it is more likely to die before being able to reproduce. Conversely, if a trait is beneficial to the offspring, it has a greater chance of survival and reproduction. Over the course of successive generations, beneficial mutations will become commonplace in the genetic code of a species. If an environment is capable of supporting a finite number of species, those who are better adapted to the environment will be the ones to survive and reproduce, making the beneficial adaptations part of the standard genetic structure of a creature.

This principle has inspired a more abstract idea of adaptation in design and the performing of tasks in the world of machine learning. A population of networks may be assigned a task and the way they perform the task is defined by a genetic structure, which could be as simple as a string of bits. Each bit or

set of bits correspond to how the network performs a task and could manifest as a decision or action that is performed at a given time. By beginning with a random genetic structure, the networks then perform the task and those who perform the task most successfully will be allowed to reproduce their genetic material that will define how the subsequent generation performs the task. Those less successful will be removed from the gene pool and thus the next generation will be based on a selection of the most successful from the previous generation. If mutations to the genetic structure are also included in the process of reproduction, the population of networks will evolve through successive generations to become superior at performing the tasks assigned.

As in biological evolution, evolutionary algorithms will require many generations of slow adaptation to refine their performance of a given task. Consideration should also be made that while each successive generation is learning to perform better on average than the previous, evolutionary algorithms are not designed to find the optimal strategy to perform a task. Several very diverse strategies may lead to initial successes, however, one may be considerably more successful over the course of generations than another, and as such populations may become stuck in an “evolutionary cul-de-sac”, unable to improve as the nature of such a large change in strategy can lead to initially worse performances, which are selected against. The most successful optimisation strategies may therefore utilise large populations capable of supporting a number of successful strategies, although supporting larger populations can lead to a large increase in computational time to see these networks evolve.

A final consideration to evolutionary algorithms is the concept of seeding. Some elements of positive task performance may be known to the programmer and thus the initial population may be seeded so that early successes and successful evolutionary avenues are present in the initial populations. This may not happen at just the outset, it can also be useful to have a network learn to perform a task by breaking it into a set of smaller sub-tasks that can be optimised individ-

ually. Essentially if the successful performance of *task B* requires the successful performance of *task A*, it may be more prudent to train networks to perform *task A* in a more optimised way before subsequently training them to perform *task B*. The consideration does not have an obvious solution and decisions should be made on a case by case basis. It is important to weigh how helpful an initial seed defined by the programmer will be to the subsequent evolution of networks. In many cases, this may only be understood through trial and error.

7.3 Architecture of a Neural Network

The neural network utilises the principle of evolutionary algorithms in order to produce a rudimentary brain, designed to complete specific tasks. Subsequently the structure of the brain is changed as the network learns to perform tasks. The user of a neural network will recognise only the input and the output of the network, whereas the central stages are a much more abstract structure. Figure 7.1 shows an example network structure, which can be identified into several key points.

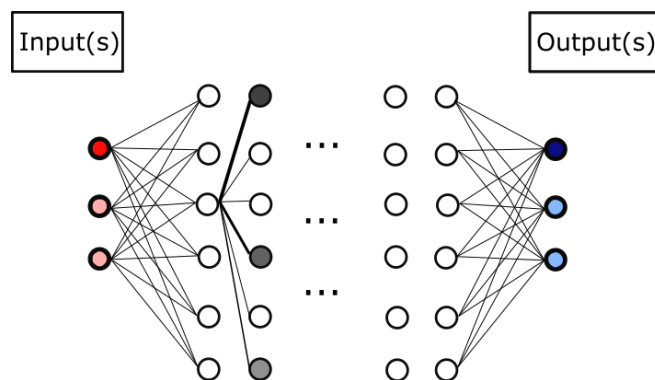


Figure 7.1: An example of a generic neural network structure highlighting the inputs and outputs as the key features and multiple connections of different strengths that are formed within the network.

The inputs to the neural network represent the information that the network has at its disposal and the outputs represent the choices that the network makes based on those inputs. The central part of the network is constructed by a set of nodes in a number of layers. Each node in a layer is connected to every node in the previous and next layer. Ultimately, the central structure of a neural network is defined by learning combinations of connection that give the most consistent or true results. The formation of a categorising network is managed through a training period that enforces decisions through the methodology of reweighting pathways that come to a decision.

The layers that make up a bespoke neural network will depend on the task being carried out. In the following sections, the structure of a convolutional neural network (henceforth CNN) will be discussed.

7.3.1 Fully Connected Layers

Fully connected (or dense) layers are the most crucial structure for machine learning in neural networks. They are made up of layers of nodes that each contain a numerical value. Within the fully connected layer, every node in one layer is connected to every node in the next layer. The node takes these inputs and determines a suitable output based on the information being presented to it. While it is important to convey the general architecture of a fully connected layer, it may not lead to complete understanding of the subtleties of machine learning. In order to understand how a neural network functions on this subtler level, it is prudent to consider a single node within the fully connected layer and how it responds to inputs.

The functionality of a node is illustrated in Figure 7.2. Essentially, the previous layer to the node contains a set of input values, x_i . These values may be numerically significant, representing how activated a node has become, or else discrete values representing discrete levels of activation, such as binarised values, on or off (represented with 0 or 1). The nodes can also be negatively valued

meaning a nodes contribution reduces the activation of subsequent layers, when set discretely, values of 1, 0 and -1 would be suitable.

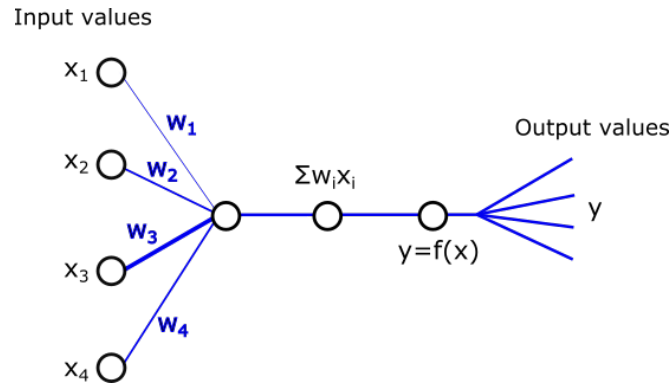


Figure 7.2: An illustration of a functionality of a node in a neural network showing a set of inputs, x and a simplified diagram of internal processing resulting in a node's output value, y .

Each input node has a weighted value that defines its strength of contribution, w_i . In order to determine how the node activates the sum of the product of its inputs with their associated weight is taken. An additional consideration should be made at this point in that the weighted sum may be offset by applying a bias value to the sum. Thus the input that the node sees is:

$$x = \sum_i^N x_i w_i + b, \quad (7.1)$$

where x represents the single valued input of the node based on the previous layer and b is the bias value that the node requires of the incoming sum. With the single valued input now calculated, this is passed through an activation function.

An activation function determines the output of the node based on its input and generally utilises correlation in some capacity. The specific choice of function should depend on the form of the output. For example, in a network whose nodes are binarised, the activation also serves to binarise the result based on a given threshold. This may be useful if an output is based on one or more yes or no choices as an output. If node values are not binarised, the activation function

may serve to limit the output of a node in a consistent way. When large numbers of inputs are summed, even if the sum is weighted so that few inputs actually meaningfully contribute, the subsequent stacking of layers could lead to values of activation that may be large or arbitrary. In this case the activation function should be a function that sets the level of activation to exist between zero and one. An example of such a function would be the sigmoid activation function, $\sigma(x)$:

$$\sigma(x) = \frac{1}{1 + e^{-x}}. \quad (7.2)$$

The specific choice of activation function in the experiments conducted will be discussed alongside the experiment conducted.

The functionality of the interpretation of information passing from one layer to the next can be presented in a concise mathematical way:

$$\begin{bmatrix} y_1 \\ y_2 \\ y_3 \\ \vdots \\ y_m \end{bmatrix} = f \left(\begin{bmatrix} w_{1,1} & w_{1,2} & w_{1,3} & \cdots & w_{1,n} \\ w_{2,1} & w_{2,2} & w_{2,3} & \cdots & w_{2,n} \\ w_{3,1} & w_{3,2} & w_{3,3} & \cdots & w_{3,n} \\ \vdots & \vdots & \vdots & \ddots & \vdots \\ w_{m,1} & w_{m,2} & w_{m,3} & \cdots & w_{m,n} \end{bmatrix} \begin{bmatrix} x_1 \\ x_2 \\ x_3 \\ \vdots \\ x_m \end{bmatrix} + \begin{bmatrix} b_1 \\ b_2 \\ b_3 \\ \vdots \\ b_m \end{bmatrix} \right) \quad (7.3)$$

$$\mathbf{x}^{(k+1)} = f(\mathbf{w}\mathbf{x}^{(k)} + b), \quad (7.4)$$

where f represents the activation function, b is the applied bias value, \mathbf{x} is a vector that denotes the values of all nodes within the layer with the superscripts k and $k + 1$ representing the layers index number within the network. \mathbf{w} is the matrix that represents each individual weighted connection between each node in the previous layer to the next.

The architecture presented in this section shows the structure of the part of the network that learns. A neural network can be constructed with further layers designed to make training more effective.

7.3.2 Additional Layers in a Convolutional Neural Network

Discussion of the inputs to a network has thus far been neglected, but it is necessary to specify exactly how information is input into the neural network. For image recognition, the input into the system is, naturally, the image itself, either in a raw form or with relevant features artificially highlighted through a set of preparations. An image can be considered as a 2-D matrix of pixel values and so the input of an image into the network can be considered as functionally identical to the input of a matrix. The input of a matrix into a network can be considered as predictably sized numerical values in two dimensions of a defined size. For the simplicity of input into a network a matrix transformation operation (using `flatten()` in python) is performed, which takes a 2D matrix and reduces it to a single 1D matrix, as illustrated in Figure 7.3. Flattening the matrix allows the input to be as simple as possible at no cost. Features between neighbouring cells can still be identified as it is the relationship between certain cells that is strengthened in the learning process and this does not take into account whether the index of a given cell is close to the index of another relevant cell.

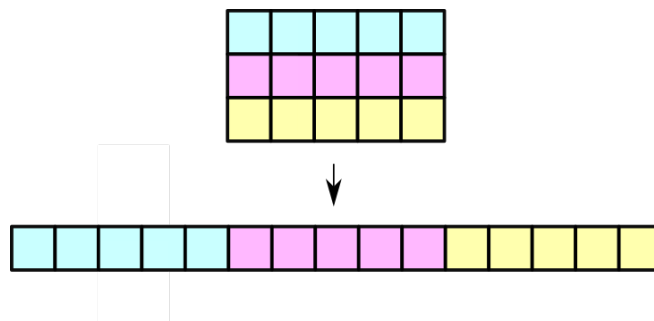


Figure 7.3: An illustration of the flattening of a 2D matrix into a long 1D matrix.

Convolution and Pooling Layers

Although all layers discussed to this point are able to function as a neural network capable of performing image recognition tasks, it is sometimes useful to process

the raw input data in some manner so that what is processed is more of a map of features within a matrix. It is useful to do this firstly as it allows for the highlighting of important features, such as an edge detection in an image. Secondly, transforming raw input data into a feature map allows for a reduction in size of the input data. As machine learning is a computationally intensive process, any reduction to the overall size of the number of weights and biases to learn in the fully connected layers will save computational time.

Convolutional layers take the input matrix or image and convolves with a feature detecting kernel. The way a feature map, S is created through the convolution of an input matrix M , and a kernel K , can be expressed mathematically as:

$$S(x, y) = (M * K)(x, y) = \sum_i \sum_j M(i, j)K(x - i, y - j), \quad (7.5)$$

where x and i represent horizontal cell indices, and y and j represent vertical cell indices [60]. Figure 7.4 shows the convolution of an input and a kernel and how the output is formed in a visual manner. An example of a typical kernel used in image recognition would be a Sobel kernel, an edge detection kernel:

$$\begin{bmatrix} -1 & 0 & 1 \\ -2 & 0 & 2 \\ -1 & 0 & 1 \end{bmatrix} \quad \text{or} \quad \begin{bmatrix} -1 & -2 & -1 \\ 0 & 0 & 0 \\ 1 & 2 & 1 \end{bmatrix},$$

which detect horizontal and vertical edges in an image respectively.

Pooling layers serve to remove a sensitivity to features being in a specific location. The process of pooling is very straightforward. Essentially, the value of a collection of cells, typically 2×2 , are pooled together in a given way. This could be the sum or average of the values in the cell but for experiments conducted in this thesis, the maximum value of the four cells is taken. This is known as a max pooling operation and is illustrated in Figure 7.5.

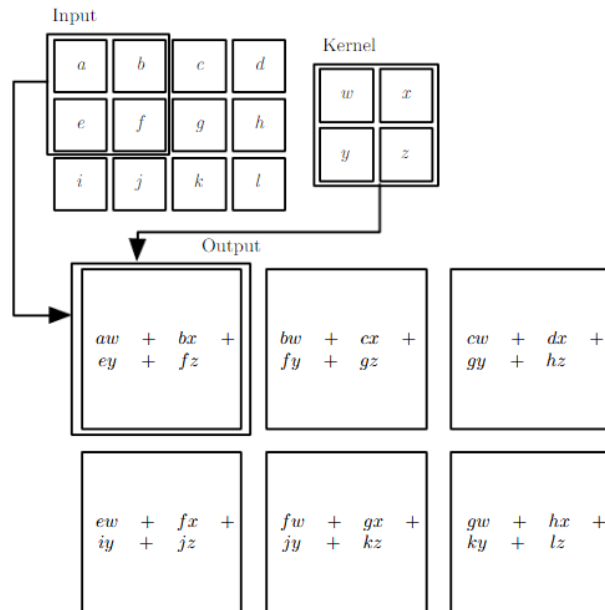


Figure 7.4: An image taken directly from Goodfellow et al. [60], showing an illustration of a convolution operation between an input and kernel.

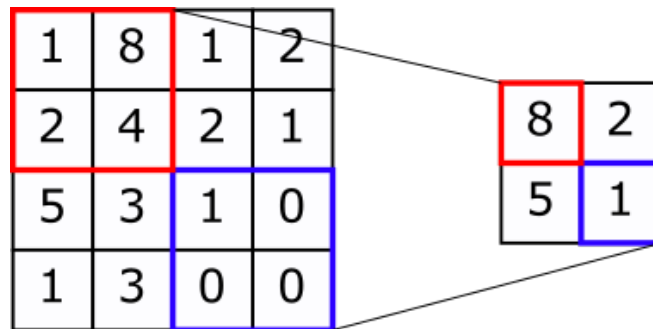


Figure 7.5: An illustration of a max pooling operation conducted on a matrix, taking the maximum value of a group of cells.

7.4 Training of a Neural Network

The training of a neural network requires the modification of the weights and biases between nodes in the fully connected layers described in Section 7.3. Early strategies of network training take their inspiration of genetic algorithms, that is the best performing of a randomly generated set of weights and biases form the basis of the next generation of networks. These are modified slowly over

generations and the best performing are kept so that the population of networks improves at the task.

More modern methods have taken to leaving the evolutionary strategy behind and go for a more sophisticated direct approach to training a network. The training process essentially compares the output or outputs of a network with the outputs that it should give, this is achieved using a loss function. A loss function is a measure of how incorrect the output's value is compared with the true value. Simply, the square of the error is taken:

$$L(y) = (y - y_0)^2, \quad (7.6)$$

where $L(y)$ is the loss calculated, y is the output given by the the network, and y_0 is the correct value. Ultimately, the loss given by the network needs to be minimised. The loss function depends on the inputs, and all the weights and biases within the network. Finding a local minimum in a function is mathematically trivial, simply it is the point at which the gradient of the function is zero. Two problems arise from determining this gradient, however, the first of which is that the loss function depends on every weight, bias and activation level of every node. This means that the loss value and the gradient is dependent on thousands of variables. The second problem is that minimising the function by finding a minimum is only effective to find a local minimum, that is that while this may be a minimum in the system, it may not be the global minimum. The global minimum in this case would represent the ideal set of weights and biases that the network could have to produce the best possible output, given the architecture. The second problem should not be viewed as an obstacle but more a consideration. In a dynamic learning environment, when input data is constantly being generated to feed in, the ideal configuration of all connections may not be determinable. As long as the network performs sufficiently well at tasks, a local minimum may be sufficient.

It is also possible to manipulate the network's multiple values through a technique known as back propagation. Each node's value depends on three pa-

rameters, the weights connecting into the node, the bias of the node, and the values of the inputs into the node, mathematically this is expressed:

$$x^{(l)} = f(w^{(l)}x^{(l-1)} + b^{(l)}). \quad (7.7)$$

In order to understand back propagation, one should consider the output layer and consider how the weights and biases should be adjusted. The loss that the network experiences by adjusting the weights such that those which affect the loss most are most heavily adjusted. The method of steepest descent is a method of modifying these values using the gradient of the cost function and proposes a new value for the weight defined by:

$$w'_k = w_k + \epsilon \frac{\partial}{\partial w_k} L(w_k), \quad (7.8)$$

where w' is the new value for the given weight, w is the initial value, $L(w)$ is the loss function, and ϵ is a constant known as the learning rate [60]. If all weights and biases are adjusted using the technique, all that remains is to calculate the derivative of the loss function. Here, it is useful to define some quantities formally:

$$L = (a^{(l)} - y)^2 \quad (7.9)$$

$$z^{(l)} = w^{(l)}a^{(l-1)} + b^{(l)} \quad (7.10)$$

$$a^{(l)} = f(z^{(l)}), \quad (7.11)$$

where l represents an index that refers to the considered layer, $z^{(l)}$ is to combine the multiple inputs to be applied to f , the activation function, $a^{(l)}$ is the value after the activation function is applied and represents the final level of activation of a given node. Using the chain rule, it is possible to determine the modification of a weight:

$$\begin{aligned} \frac{\partial L}{\partial w^{(l)}} &= \frac{\partial L}{\partial a^{(l)}} \frac{\partial a^{(l)}}{\partial z^{(l)}} \frac{\partial z^{(l)}}{\partial w^{(l)}} \\ &= 2(a^{(l)} - y) f'(z^{(l)}) a^{(l-1)}, \end{aligned} \quad (7.12)$$

as well as the modification of a bias:

$$\begin{aligned}\frac{\partial L}{\partial b^{(l)}} &= \frac{\partial L}{\partial a^{(l)}} \frac{\partial a^{(l)}}{\partial z^{(l)}} \frac{\partial z^{(l)}}{\partial b^{(l)}} \\ &= 2(a^{(l)} - y)f'(z^{(l)}).\end{aligned}\tag{7.13}$$

Essentially both derivatives depend on the activation function used and how active the node is. The adjustment to the weight has an additional proportionality to the level of activation of the previous layer.

Finally, it is also useful to understand that the level of activation of the previous layer will affect the activation of the next in addition to the weights and biases. Thus a third equation can be determined:

$$\begin{aligned}\frac{\partial L}{\partial a^{(l-1)}} &= \frac{\partial L}{\partial a^{(l)}} \frac{\partial a^{(l)}}{\partial z^{(l)}} \frac{\partial z^{(l)}}{\partial a^{(l-1)}} \\ &= 2(a^{(l)} - y)f'(z^{(l)})w^{(l)},\end{aligned}\tag{7.14}$$

which shows that the level of activation of the previous layer should be adjusted in proportion to the weight of its connection. Unlike the weights and biases, the activation of the previous layer's nodes cannot be numerically altered directly but it can be altered through the same considerations applied between the penultimate and output layers. The idea of back propagation, then, seeks to adjust weights and biases starting from the the output and working back through the layers until the first fully connected layer is reached.

The final consideration of network training is that in order for the network to develop strong and definitive associations, training must be done through a very large number of examples. The numbers involved are typically of the order of $10^3 - 10^5$ so as to produce consistent and reliable results.

7.5 Predicting Input Parameters of Simulations

7.5.1 Preparation of Training Data

Simulated molecular networks, discussed in Chapter 6 were proposed as a suitable candidate to explore the machine learning techniques discussed. Experiments were conducted varying the simulation parameters discussed in that chapter, namely the concentration of molecules, the strength of bonding between those molecules, and the temperature of the system. Concentration, C , was varied at 12 levels between 0.1ML and 0.8ML. While the numbers involved for bond strength and temperature are of arbitrary units, the same values were used as to produce the phase maps in chapter 6, that is 12 levels of bond strength, ϵ , between 0.1 and 2.0, and 12 levels of temperature, T , between 0.1 and 1.0.

In order to produce the numbers of simulated results necessary for machine learning, each fixed combination of these parameters was given 100 repetitions and thus 100 final state lattices were produced using the Monte Carlo methods previously discussed. The data sample size was therefore 172800 final state lattices with varied input parameters.

For the input into the network it is unnecessary to input the image representations of the final states, the raw matrix representations of the final state lattices were, therefore, used. Each of these is a 2D matrix of dimensions 45×45 with non-zero numbers representing occupied lattice sites, where the specific number represents the orientation of the molecule. Due to the way machine learning works, it is not necessary to provide the network any information on the specific meanings behind the numbers as it will build the associations between the lattices and its decisions.

7.5.2 Architecture of network used.

Figure 7.6 shows the architecture of each layer of the network used. It is useful to break down the stages of preparation for the specific task in order to better

understand the function of the network. The first six layers are alternating convolution and pooling layers designed to condense the input matrices into feature maps. The first convolution layer takes the input matrix and convolves it with 16 kernels to produce 16 different feature maps, these are then pooled to reduce their size. At this stage, the matrices are convolved with two more kernels, pooled, followed by a final convolution with two further kernels and a further pooling operation resulting in 64 matrices of size 3×3 .

The key observation here is that the information supplied to the fully connected, or dense, layers is a very abstract feature map, which, while being much more impenetrable to human recognition, a neural network can utilise in a much more effective manner than the original raw input matrices.

For the prediction of input parameters of a simulation, it follows that the neural network will have three output parameter, each corresponding to one of the input parameters of the simulation.

For the fully connected layers, the *rectified linear unit* (henceforth ReLU) activation function was used. ReLU is a very simple function:

$$\text{ReLU}(x) = \max(0, x), \tag{7.15}$$

hence the activation level is x if x is positive, and zero otherwise. This particular function has one consideration that should briefly be mentioned. It does not confine the values within a given range. Section 7.3.1 shows that it can be useful to restrict an activation to output values to a given range, such as between 0 and 1, or -1 and 1. The restriction does not need to be implemented for the prediction of simulation parameters as the outputs will correspond to these parameters. If the network overestimates the value of the parameters, the loss function will punish this overestimation heavily. In short, the task itself restricts the possible predictions that the network can make and the unlimited upper end of the ReLU activation function will not pose problems.

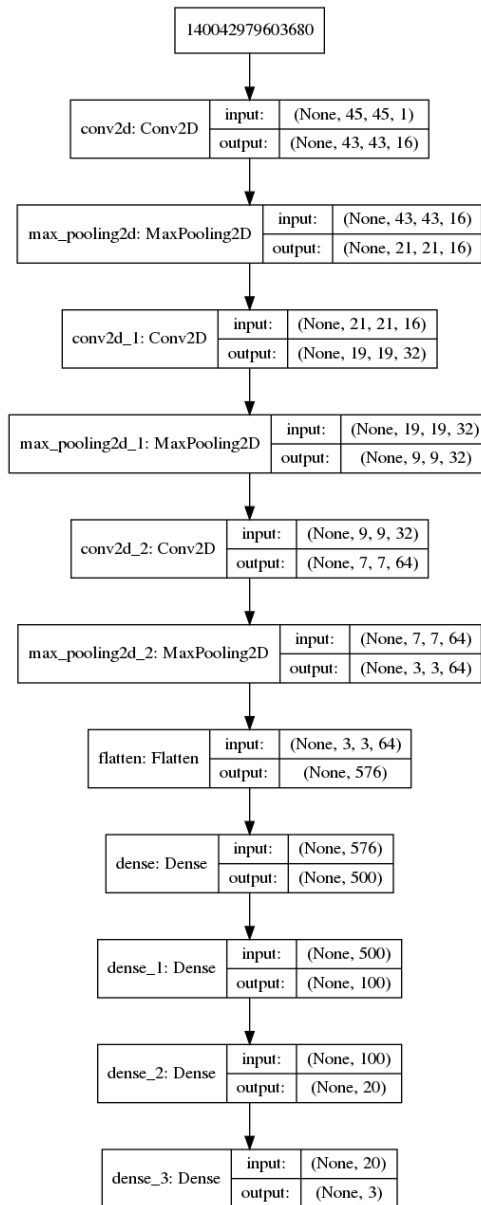


Figure 7.6: A flowchart representing the layers applied within the neural network

7.5.3 Prediction of Simulation Parameters

In order to perform a fair test, it is necessary that the testing data is distinct from the training data. A selection of ~ 16000 final lattice states were tested to determine the capability of the network after training. The results of the predicted value against the true value for each input parameter are presented in

Figure 7.7. The graphs presented show the true value of the parameter plotted

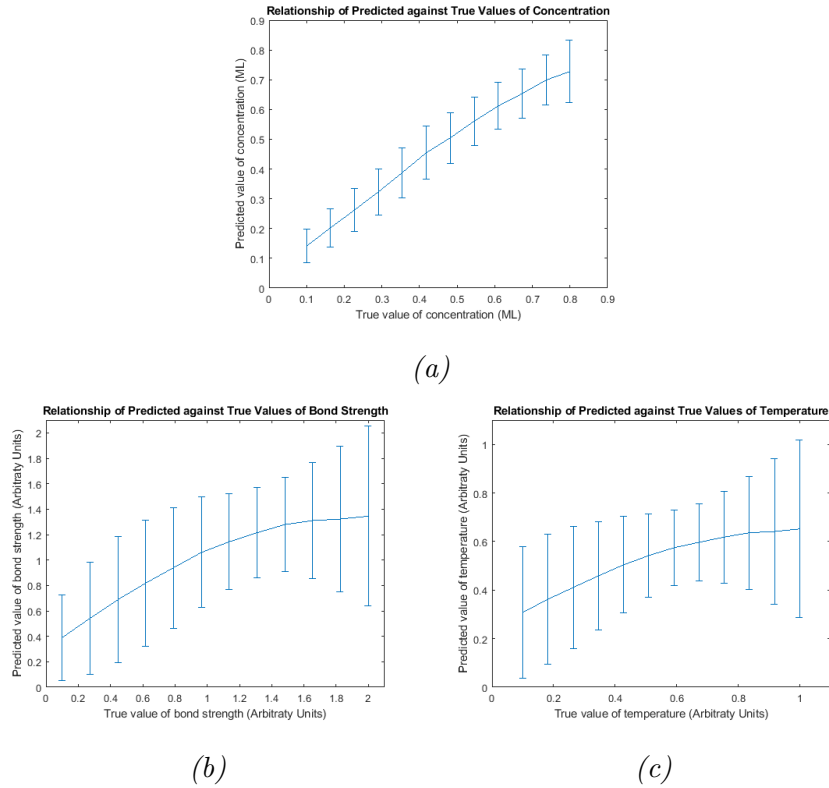


Figure 7.7: Graphs of predicted values of the three simulation parameters against their true values.

against the mean of the predicted values. The error bars show the root mean square error calculated from the statistical deviation from the mean. The graph for the concentration parameter shows a reasonable correlation between predicted and true values. For the other two parameters, this correlation is present but far less pronounced.

It can also be observed that in the prediction graphs for ϵ and T , the error bars are larger at the extremes of the scales. This may be due to a couple of subtle factors. At high temperatures and low bond strengths, there will be an increased ambiguity, due to the nature of unbound lattice states being disordered. Likewise at high bond strengths and low temperatures, lattices that are formed are likely to be fixed in place with much less chance of seeing significant changes in the

arrangement of molecules. This may also lead to an increase in ambiguity. The most distinction between parameters may therefore exist toward the middle of the parameter range as an artifact of statistics. This can be tested by running a greater set of experiments within a smaller range in the given parameters.

The overall root mean square errors for each input parameter are given as follows:

$$\varepsilon_C = 0.0807$$

$$\varepsilon_\epsilon = 0.4708$$

$$\varepsilon_T = 0.2387,$$

where ε represents the error in the given parameter, C represents the concentration, ϵ represents the bond strength, and T represents the temperature of the system. To further understand the suitability of these values they can be shown as a proportion of their ranges:

$$\varepsilon_C = 11.5\%C$$

$$\varepsilon_\epsilon = 24.77\%\epsilon$$

$$\varepsilon_T = 26.52\%T.$$

Ultimately, while the predictions of simulation parameters made by the network showed some correlation to the true values, the predictions were only a rough approximation. Nevertheless, as an initial experiment it showed promise for further testing of the simulation data with machine learning.

7.6 Categorisation of Simulated Results

Chapter 6 described an attempt to categorise final state lattices of simulations based on a couple of key values, N , the number of bonds per molecule, and P , the preference score, which shows the collective affinity of molecules bonding with those in identical configurations. This provides an interesting experimental space to test categorisation properties of a machine learning.

There is a very discrete change observed between behaviour of lattices with $N < 1$ and $N > 1$. As previously discussed, when $N < 1$, the collective behaviour of the molecules is disconnected, resulting in a diffuse state with molecules not forming bonded networks. The visual interpretation is very clear between these two states and there is a distinct numerical boundary that defines a diffuse and non diffuse lattice. The preference score, P , is a much more continuous property of the lattice and, while statistically prudent, is much less visually clear to interpret.

It was decided to define four distinct categories:

- **Class 0:** — Any final state lattice with $N < 1$,
- **Class 1:** — A final state lattice with $N \geq 1$ and $P < 1$,
- **Class 2:** — A final state lattice with $N \geq 1$ and $1 \leq P < 2$,
- **Class 3:** — A final state lattice with $N \geq 1$ and $P \geq 2$.

Figure 7.8 shows an example final state lattice for each of these categories.

After the classification was applied to all final state lattices simulated, 90% of these were used for training the network and 10% were then tested against the trained network.

7.6.1 Architecture of the Network

Figure 7.9 shows the layered structure of the neural network used for the classification task. This network features a different type of layer known as a dropout layer. The functionality of this is to drop the activation of randomly selected nodes in the network. When training, nodes and connections are fine tuned to the specific task using the techniques discussed in Section 7.4. There may be issues in that certain pathways may become very strongly associated with a large part of the task given. This is a problem as a single pathway will still not be perfect and hence errors in judgement will strongly influence key decisions. It is better

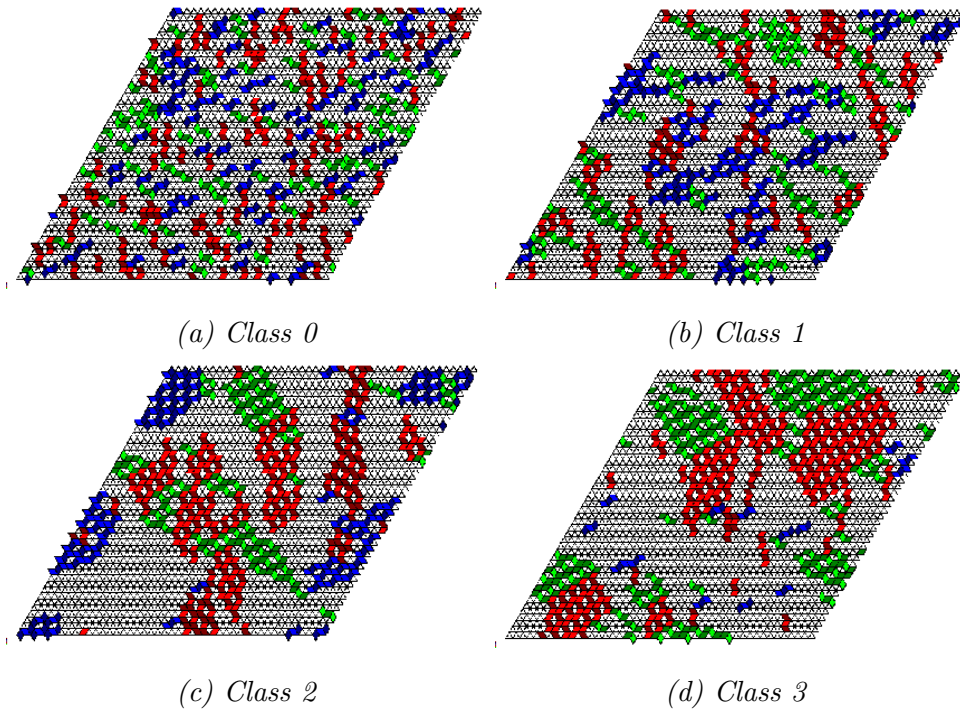


Figure 7.8: A representation of how final state lattices of the different classes appear.

that a number of pathways be jointly involved and the dropout prevents small paths becoming too dominant in responsibility for a final output. A crude but useful analogy would be that with more pathways being responsible for choices, more “thinking” is applied to a task.

The activation function used in the fully connected layers of this network was a softmax function. This function activates the node to a level similar to a probability. If x represents the input to a node as given in equation 7.1, then the softmax produces an output:

$$y_i = \frac{e^{x_i}}{\sum_j^K e^{x_j}}, \quad (7.16)$$

where K represents the layer index. So activation values of all nodes on a layer will sum to unity.

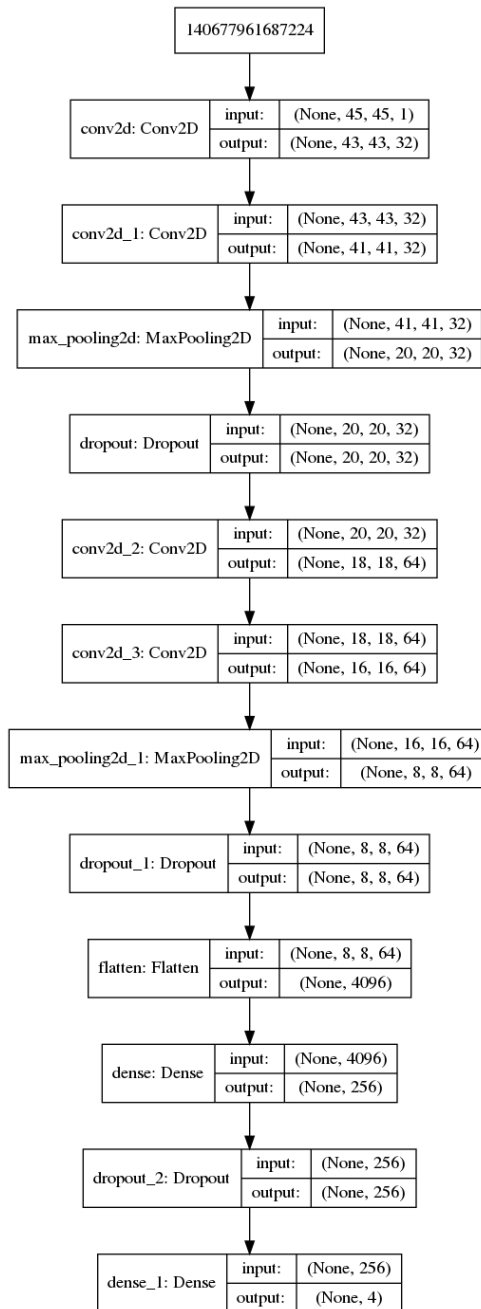


Figure 7.9: A flowchart representing the layers applied within the neural network.

7.6.2 Results of Categorisation using Machine Learning

Figure 7.10 shows the results of the predicted categorisation made by the neural network displayed in a matrix. The matrix shows the accuracy of predictions made by the network showing the probabilities involved in how the network

categorises a given class. The most promising result here is that the network was strongly able to differentiate between diffuse and non-diffuse final state lattices with an accuracy of 98%. This is an excellent result as the network has no prior understanding of the number of bonds per molecule, N , it can entirely infer it based on the final state lattice arrangement.

The predictions given that differentiate between classes 1, 2 and 3 are also very promising results despite the numbers appearing less accurate at first glance. The preference score, P , exists as a continuous value, whereas the classification of these networks was only made with a rudimentary classification in mind. An example of the flaw of the classification would be that a final state lattice with a preference score of $P = 0.98$ would be in the range of $0 \leq P < 1$ but would be functionally much more similar to networks with a value of $P = 1$ than those of $P = 0$. Confusion between non-diffuse classes occur almost solely between a class and the classes immediately above or below it. Class 1 shows a prediction accuracy of 87% but the percentage misclassified as class 3 is only 0.3%. While the classification performed by the network is still limited, the network definitely shows an understanding of how P changes between different networks, while not truly divining its direct value. Incorrect classification occurs but it is not certain whether this is due to the limitations of the network or the arbitrarily divisions drawn in the classification system.

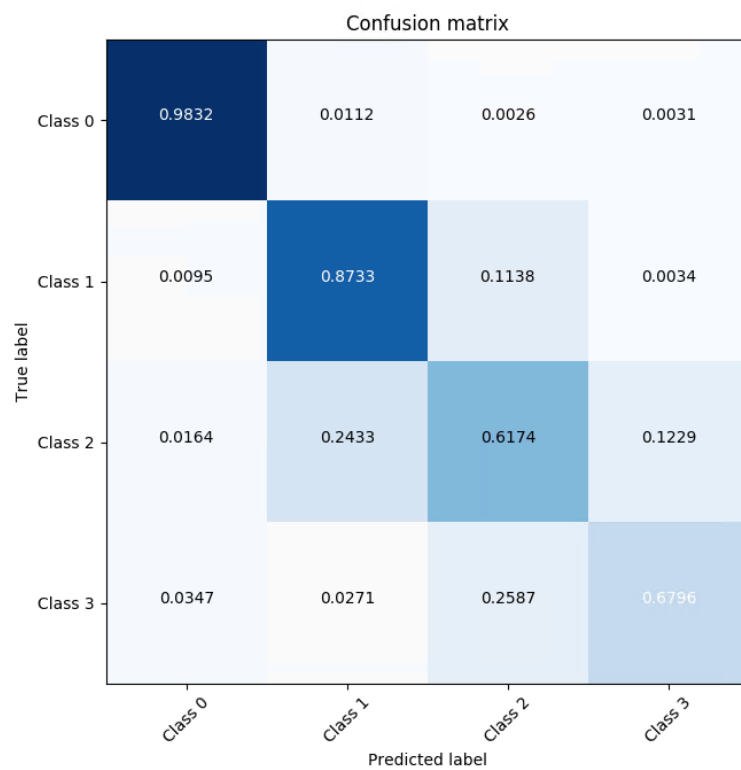


Figure 7.10: A confusion matrix showing how the network's predictions of a class correspond with the true class of a final state lattice.

Chapter 8

Conclusion

This thesis has maintained a common theme in the analysis of the bi-isonicotinic acid molecule and the networks it forms. The molecule is of a high level of interest for a number of reasons. While previous studies have been conducted into networks governed by hydrogen bonding, the *trans* form of the bi-isonicotinic acid molecule has some features that distinguish it from other molecules of study. Its surface-induced chirality means that, while it shares bonding characteristics with the tectons discussed in Chapter 4, the number of orientations that the molecule can take to form a continuous network is reduced, leading to restrictions in the formation of assemblies. These restrictions provide a strong reason to study these assemblies as a reduction in degrees of freedom of a system can arguably lead to a greater focus on the remaining degrees of freedom themselves. This property also necessitated a much less intuitive, but greater refinement in determining bonding geometries.

One of the key findings of Chapter 5 was the apparent restriction of hydrogen bonding to a single common direction that defined domains within broader networks. Certainly it seems that bonding is restricted to fixed orientations within networks but reasons for the phase changes within these networks is worth further consideration. One hypothesis might be that the changes in phase are driven by the underlying Au(111) surface. It would be very useful to analyse

a network boundaries in comparison to the direction of the characteristic heringbone structure of the bare Au(111) surface. This analysis will determine whether the observed changes in bonding orientation are present independent of the underlying surface structure. Such a study would provide additional insight in the dynamics of network growth as a network with a collection of domains of different phases may be a consequence of many small domains growing and meeting each other with insufficient mobility to facilitate domain coarsening on the timescales observed in a low temperature system. With all of these considerations, a study would be well placed to analyse networks deposited on Au(111) with specific focus given to the underlying surface features and this should be conducted at multiple temperatures. Comparative studies should also be made with surfaces that do not have the distinctive features that define the Au(111) surface. The surface of the crystal is crucial in this study so a reasonable study may compare different crystal directions, and their effects on the surface, and how these different surface orientations define the networks.

The studies conducted in Chapter 6 have taken preexisting simulations of molecular dynamics and built upon them. This created more refined models that incorporate the specific bonding geometries of bi-isonicotinic acid. The results of this chapter provide a demonstration of network growth and evolution with specific constraints. The capacity for the continued evolution of this model. Modifications and increasingly sophisticated constraints can be placed on such simulations, however, such considerations should be considered with caution. The scope for increasingly sophisticated algorithms is potentially unlimited, however, the execution highlights the principle of diminishing returns. The most prudent examination of these experiments should expect that a model can be refined to better express the dynamics of an evolving system but equally be limited in its capacity to model reality, rather becoming more and more of an academic exercise. Continually evolved models, therefore, must exercise caution

in not letting the modelling of specifics outweigh the generality of reality. In increasingly specific simulations, this will always be the danger.

With such a clear consideration presented, there is still plenty of scope for the continued evolution of the model used to represent the tiling dynamics of bi-isonicotinic acid. Thus far, the current simulations have not taken into account different surface dynamics. While it has been remarked in Chapter 6 that the constant surface potential should not mathematically have an effect on the evolution of lattices, surface properties do in reality provide a very important role in defining the evolution of systems. The incorporation of this, therefore, is an important adaptation that needs to be implemented to some degree in the evolving dynamics of simulations. A prudent hypothesis of work needs to modify simulations but allow them to evolve based on additional restrictions placed, such as discontinuities in surface potentials and work out how to effectively apply them within simulations.

Chapter 7 represents an exploration of the future of SPM. Machine learning has existed for some time but significant advancements are being made in the field along side its applications. The results from this chapter show a nascent ability for a machine to categorise observed molecular assemblies, potentially in a real time scenario. Within any field of study in science, there will be a number of possible obstacles to progress. In the field of SPM broadly, and certainly in UHV low temperature SPM specifically, a large obstacle is the time. While sample preparation and successful depositions represent a large time investment themselves, a large portion of time is invested in acquiring appropriate images. The acquisition of images is itself a slow process and the time cost is further compounded by the need for tip conditioning, which is necessary for both clarity and stability. The automation of this process and similar processes has numerous advantages. Firstly it allows for an SPM to be freed from continuous human supervision. This means the acquisition of *useful* data can be greatly increased with automation improving tip conditions both as a time cost and

in terms of efficiency. A more relevant application that can be drawn from experiments conducted within this thesis is the principle of classification that can likewise take place while acquiring data. If a machine, even in a rudimentary sense, is able to provide perspective on the networks or surfaces that it is imaging alongside the perspective of the user. Large strides may be made in the field of nanoscience.

While the perspective on the future remains hypothetical at this time, it is a realistic idea. Machine learning is a field that requires a huge amount of input data in order to make any significant progress in learning. Data acquisition in SPM is a constant and large amounts of data are collected. While most of these data are perceived as unsuitable for presentation, they are potentially incredibly useful for training purposes in the automation of SPM.

Appendices

Appendix A

Derivations

A Driven Simple Harmonic Oscillator

This section handles the full derivation of the solution of the a driven harmonic oscillator as covered in Section 2.3.

The derivation begins with Equation 2.37, that is:

$$m \frac{d^2 z}{dt^2} + b \frac{dz}{dt} + kz = F(t), \quad (\text{A.1})$$

Solving the steady state solution (particular integral) of the oscillator can be very involved with sines and cosines, thus it is easier to solve as a single exponential and deal with the physical consequences later. Formalising this equation leads to:

$$\frac{d^2 x}{dt^2} + \frac{b}{m} \frac{dx}{dt} + \frac{k}{m} x = \frac{F_0}{m} \cos(\omega t) \quad (\text{A.2})$$

and this can be rewritten as:

$$\frac{d^2 x}{dt^2} + \frac{b}{m} \frac{dx}{dt} + \frac{k}{m} x = \frac{F_0}{m} e^{i\omega t} \quad (\text{A.3})$$

The particular integral can then be taken:

$$x_p = Ae^{i\omega t} \quad (\text{A.4})$$

$$\frac{dx}{dt} = i\omega Ae^{i\omega t} \quad (\text{A.5})$$

$$\frac{d^2x}{dt^2} = -\omega^2 Ae^{i\omega t} \quad (\text{A.6})$$

and through substitution:

$$-A\omega^2 e^{i\omega t} + \frac{b}{m} i\omega Ae^{i\omega t} + \frac{k}{m} Ae^{i\omega t} = \frac{F_0}{m} e^{i\omega t} \quad (\text{A.7})$$

$$A \left(-\omega^2 + \frac{b}{m} i\omega + \frac{k}{m} \right) = \frac{F_0}{m} \quad (\text{A.8})$$

$$A \left(-\omega^2 + \frac{b}{m} i\omega + \omega_0^2 \right) = \frac{F_0}{m} \quad (\text{A.9})$$

then rearranging for A:

$$\begin{aligned} A &= \frac{F_0/m}{(-\omega^2 + \frac{b}{m} i\omega + \omega_0^2)} \\ &= \frac{F_0/m}{((\omega_0^2 - \omega^2) + \frac{b}{m} i\omega)} \end{aligned}$$

A is complex, which in its fundamental nature means it contains both a magnitude and a phase. To determine the magnitude:

$$|A| = \sqrt{AA^*} \quad (\text{A.10})$$

$$= \sqrt{\frac{F_0/m}{((\omega_0^2 - \omega^2) + \frac{b}{m} i\omega)} \cdot \frac{F_0/m}{((\omega_0^2 - \omega^2) - \frac{b}{m} i\omega)}} \quad (\text{A.11})$$

$$= \sqrt{\frac{F_0^2/m^2}{((\omega_0^2 - \omega^2)^2 + (\frac{b}{m}\omega)^2)}} \quad (\text{A.12})$$

$$= \frac{F_0/m}{\sqrt{((\omega_0^2 - \omega^2)^2 + (\frac{b^2}{m^2}\omega^2))}} \quad (\text{A.13})$$

it is more mathematically correct to express A with a denominator that is real:

$$A = \frac{F_0/m}{((\omega_0^2 - \omega^2) + \frac{b}{m}i\omega)} \cdot \frac{((\omega_0^2 - \omega^2) - \frac{b}{m}i\omega)}{((\omega_0^2 - \omega^2) - \frac{b}{m}i\omega)} \quad (\text{A.14})$$

$$= \frac{F_0/m}{((\omega_0^2 - \omega^2)^2 + (\frac{b^2}{m^2}\omega^2))} \cdot \left((\omega_0^2 - \omega^2) - \frac{b}{m}i\omega \right) \quad (\text{A.15})$$

The phase is expressed by analysing the relative ratio of the real and imaginary parts:

$$\left((\omega_0^2 - \omega^2) - \frac{b}{m}i\omega \right) \quad (\text{A.16})$$

and thus the phase relationship can be determined:

$$\tan(\phi) = \frac{-b\omega/m}{\omega_0^2 - \omega^2}, \quad (\text{A.17})$$

which can also be expressed as:

$$\tan(\phi) = \frac{-b\omega}{m} \frac{1}{\omega^2 - \omega_0^2} \quad (\text{A.18})$$

Appendix B

Initial Motivations of Experiments

The process of splitting water dates back to the 1800s from experiments using electrolysis. The principle uses two electrodes, a positive and negative. The oxygen makes contact with the anode, causing it to lose electrons, breaking the bond with the hydrogen atoms and to emerge as pure O₂ gas. A similar process happens at the cathode of the system, with the hydrogen being reduced, and converting to H₂ gas.

The Gibbs free energy formation is a measure of the change in energy that determines the formation of a molecule from its constituent components. The Gibbs free energy of water splitting has been recorded at $\Delta G = 237.2$ kJ mol⁻¹ [61]. This leads to the minimum potential to facilitate the reaction being determined from

$$\Delta G = nFV_{rev} \tag{B.1}$$

where ΔG is the change in Gibbs free energy, n is the number of moles of electrons, F is the Faraday constant and V_{rev} is the thermodynamic reversible potential [62]. Substituting the appropriate values gives [61] [63]:

$$V_{rev} = 1.23\text{V}$$

The Faraday constant $F = eN_A$, where e is the fundamental electron charge and N_A is Avagadro's constant. This means that $V = 1.23\text{V}$ is related to the photon energy required to split water molecules, $E = 1.23\text{eV}$ and therefore:

$$\lambda = \frac{hc}{E}$$

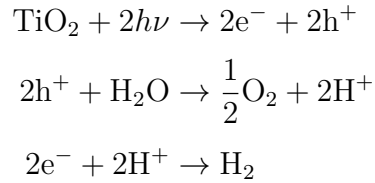
$$\lambda = 1011\text{nm}$$

This wavelength provides key pieces of information. Firstly there is enough energy in visible light (typically 400–700 nm) to split water. However, water is transparent to visible light and therefore will not absorb any incident photons to break molecular bonds. The following literature review addresses how this gap can be overcome by using an electrolysis system with a TiO_2 semiconductor base [63].

B.0.1 Electrochemical photolysis of water

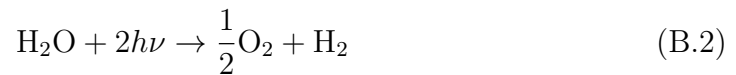
Fujishima and Honda [63] have been the point of reference for much research into the evolutions of hydrogen and oxygen from water. Their experimental setup as mentioned previously used a semiconductor base of TiO_2 irradiated by light. The TiO_2 functions as one electrode connected to a second electrode made of platinum. When irradiated, electrons are excited from the valence band into the conduction band of the TiO_2 , these then flow to the platinum electrode, creating a potential difference. the platinum functions as the cathode and the TiO_2 , the anode. A current will begin to flow for energies of around 3.0eV, or wavelengths shorter than 415nm.

The following evolution then takes place:



Irradiation of two photons on the TiO_2 surface leads to two electron-hole pairs. Here the holes at the anode facilitate the oxidation of water, creating O_2 molecules and the electrons at the cathode facilitate hydrogen reduction, creating H_2 molecules.

This leads to the overall reaction:



This is an important conclusion; indirectly, by irradiating the semiconductor surface, the wavelengths required for water splitting are now comparable to that of visible light.

Photo-catalytic Water Splitting Literature Review

B.0.2 Expanding on Dye-sensitised solar cells

This section focuses solely on the sensitizer cells themselves and not the water splitting catalysis, to review the mechanisms of the cell itself. Nazeeruddin *et al.* discuss the sensitised solar cell in an overview paper. It discusses the five components needed for the DSSCs:

(a) A mechanical support coated with Transparent Conductive Oxides; (b) The semiconductor film, usually TiO_2 ; (c) A sensitizer adsorbed onto the surface of the semiconductor; (d) An electrolyte containing a redox mediator; (e) A

counter electrode capable of regenerating the redox mediator, such as platinum [64]. As in the original paper, this is schematically represented in Figure B.1.

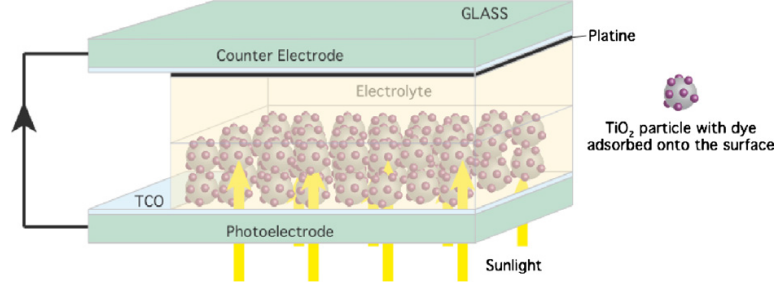


Figure B.1: Schematic representation of the DSSC [64].

Although this review will not consider the following in detail, it is useful to make note of the equations that describe the *incident photon-to-current conversion efficiency*, henceforth IPCE. This is defined as the number of electrons generated by light in the external circuit, divided by the number of incident photons as a functions of excitation wavelength:

$$\begin{aligned} \text{IPCE} &= \frac{\text{Photocurrent density}}{\text{Wavelength} \times \text{Photon flux}} \\ &= \text{LHE}(\lambda) \times \phi_{inj} \times \eta_{coll} \end{aligned} \quad (\text{B.3})$$

Here $\text{LHE}(\lambda)$ is the light-harvesting efficiency at a given wavelength λ , ϕ_{inj} is the quantum yield for electron injection from the excited sensitizer in the conduction band of TiO_2 , and η_{coll} is the efficiency for the collection of electrons [64].

Overall the efficiency (η) of the DSSC is determined as follows:

$$\eta_{global} = \frac{J_{SC} \cdot V_{OC} \cdot ff}{I_S}, \quad (\text{B.4})$$

where J_{SC} is the photocurrent density, V_{OC} is the open circuit potential, I_S is the intensity of the incident light and ff is the fill factor of the cell. The fill factor simply a ratio of the maximum power output of the cell to the maximum theoretical power output and is a measure of the quality of the cell.

Discussion of Molecular Sensitizers

Nazeeruddin *et al.* list a number of sources discussing the different molecular sensitizers analysed, not listed in this review. As discussed in the section 3.1, the **N3** has a reputation for the best photo-voltaic performances in terms of conversion yield and long term stability [64].

The main focus is the comparison of three similar molecules. They are all single centre molecules based on **N3**. The only difference is the number of free hydrogen atoms on the ligands. The molecules are shown in Figure B.2. The research given here, although not involved with catalysis, does highlight an important factor in the efficiency of cells. The term *short circuit photocurrent* is used when referring to the currents generated here; this is due to a current being seen without any externally applied voltage.

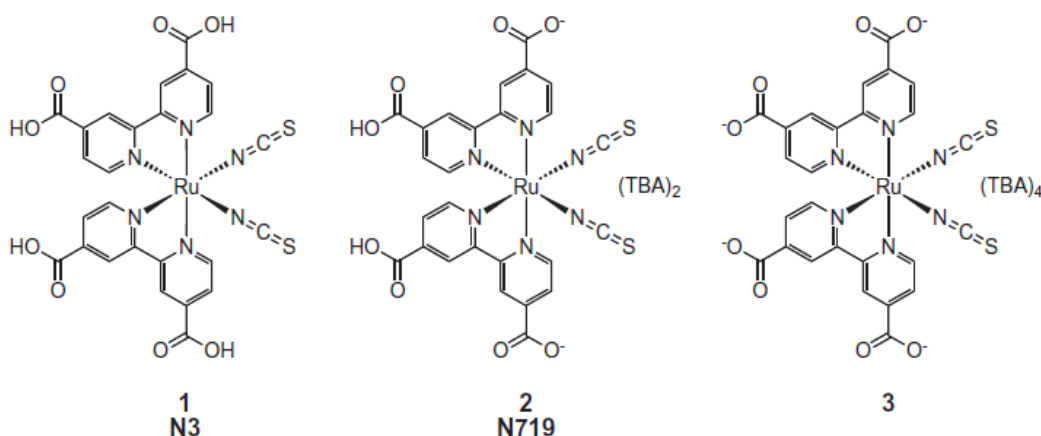


Figure B.2: The three molecules listed in Nazeeruddin *et al.* [64].

Complex **1** is shown to be fully protonated, containing four lone protons on its ligands, whereas **2** and **3** contain two and none respectively. The protonation of the dye molecules is shown to influence the efficiency of the DSSCs.

With its higher protonation, complex **1** charges the surface positively by transferring its protons. This allows the electric field associated with the dipole generated in this fashion to enhance the adsorption of the ruthenium complex and

assists electron injection from the excited state of the sensitizer into the titania conduction band, favouring high photo-currents. There is, however, a payoff; the open circuit potential is lowered due to the positive shift of the conduction band edge, induced by the surface protonation [64].

In the case of complex **3**, the reverse is true. Due to the lack of single protons, the open circuit potential is much higher in comparison to **1** but due to the relative negative shift of the conduction band, the short circuit photo-current is lower.

Optimising the short circuit photo-current and open circuit potential is key and performance data was collected from the complexes in Nazeeruddin *et al.* comparing the current and potential. Using equation B.4, it was determined that complex **2** showed the best efficiency at 11.18%. This means that the performance of the complex carrying two protons is superior to those of the compounds that contain four or no protons and so the double protonated form is preferred for the sensitization of nanocrystalline TiO₂ films. This is only for the operation of the cell and does not focus on the catalysis which is an equally important aspect.

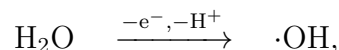
B.0.3 Making Oxygen with Ruthenium Complexes

J. J. Concepcion *et al.* reviewed the current state of ruthenium dye complexes in 2009 [29]. The account describes water oxidation in molecules that catalyse the reaction, while also functioning as a sensitiser for the semiconductor surface, as previously discussed in section 3.1. The review discusses the comparison to artificial photosynthesis, integrating several nanoscale events listed as (i) light absorption, (ii) excited-state electron transfer, (iii) directional long-range electron transfer, and (iv) single electron activation of multi-electron catalysts.

This process involves Proton-Coupled Electron transfer (PCET), referenced in the sources: [65–67]. This is a mechanism that involves the transfer of an electron through the molecule; at the same time a hydrogen atom (or proton)

is also transferred. Weinberg *et al.* describe the process in depth in a complete review of the Proton-Coupled Electron transfer mechanism.

Examining the reaction,



Concepcion *et al.* and Liu *et al.* discuss the importance of PCET. Both mention that a mechanism requiring a $1e^-$ transfer as too slow to be of interest. This is where PCET becomes a factor. It is necessary to have multiple redox equivalents accumulated at a single catalyst site or cluster.

Catalytic Water Oxidation and the *Blue Dimer*

Liu *et al.* discuss, in *Mechanisms of Water Oxidation from the Blue Dimer to Photosystem II* [67], the history of water splitting catalysts. The work focuses around the molecule pictured in Figure B.3, *cis,cis*- $[(\text{bpy})_2(\text{H}_2\text{O})\text{Ru}^{\text{III}}\text{ORu}^{\text{III}}(\text{OH}_2)(\text{bpy})_2]^{4+}$, henceforth referred to as the Blue Dimer Molecule.

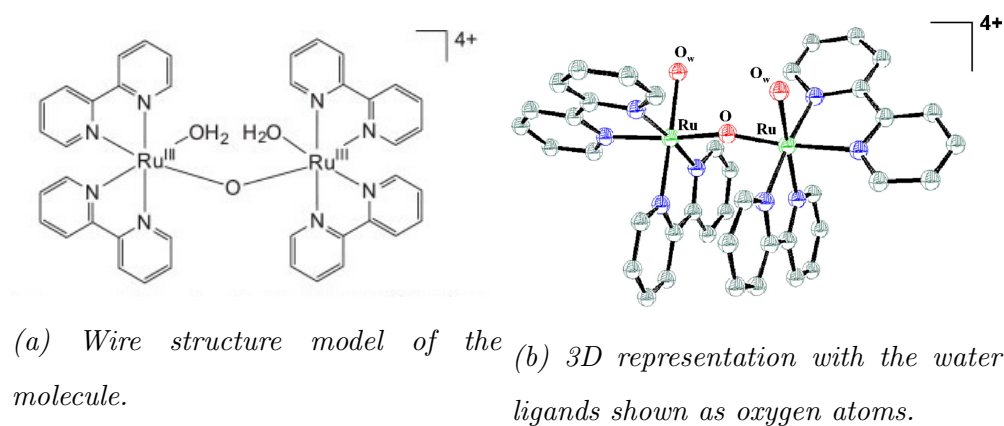


Figure B.3: The Blue Dimer molecule.

Liu *et al.* remark that the blue dimer is the first designed, well-defined molecule known to function as a catalyst for water oxidation. The article briefly discusses the history of the family of polypyridylruthenium molecules and their rich stoichiometric, catalytic and mechanistic oxidation chemistry [67] [68].

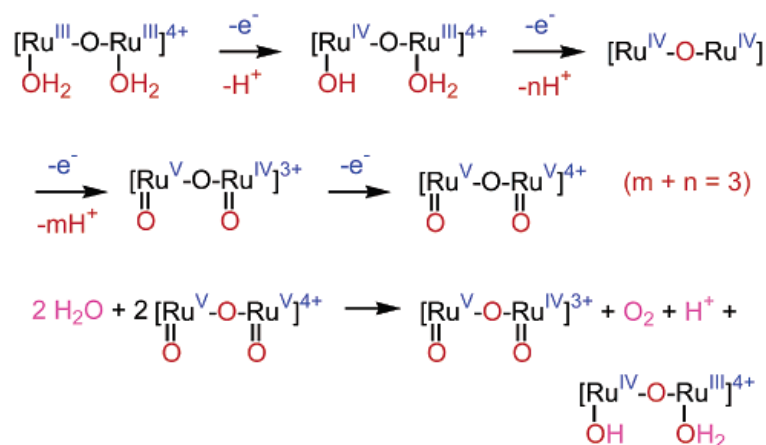


Figure B.4: Water oxidation mechanism for the blue dimer.

The water oxidation mechanism for the blue dimer is shown in the Figure B.4. It shows the PCET mechanism in each stage.

Concepcion *et al.* focus on thermochemical water splitting involving Ce^{IV} for most of the paper, however, discussion of photoelectrochemical (PEC) water splitting using the same mechanisms takes place. Particularly highlighted are the demands of useful PEC water splitting:

(i) Turnover rates as rapid as or more rapid than the solar flux of $\sim 10 \text{ mA/cm}^2$ are required. In ambient light, Photosystem II¹ turns over on the millisecond time scale. Rapid rates are needed to maximize the solar source with the goal of making the rate of solar insolation rate limiting. Even more rapid rates would enable the use of concentrator technologies. (ii) Maximum use of the incident solar spectrum throughout the visible into the near-IR is needed to maximize solar efficiencies. Manipulation of Ru polypyridyl complexes is highly evolved with good models available for black metal-to-ligand charge transfer (MLCT) absorbers that maximize light absorption into the near-IR. Even so, the thermodynamic demands for the water oxidation must be met following photoinjection. (iii) Long-term stability remains an unknown. It is encouraging that

¹The first protein complex in the light-dependent reactions of oxygenic photosynthesis.

experimental simulations point to operational stabilities of up to ~ 20 years for dye-sensitized solar cells. [29]

A final key point from Concepcion *et al.* [29] and also from Weston *et al.* [31] is the Concepcion paper shows the multicentre dye complexes catalyse the water splitting reaction more effectively than single centre ones, due to the presence of both a reaction centre and a charge transfer centre, as mentioned in section 3.1.2.

Bibliography

- [1] B. Bhushan, editor, *Springer Handbook of Nanotechnology* (Springer-Verlag Berlin Heidelberg New York, 2004).
- [2] G. Binnig, H. Rohrer, C. Gerber, and E. Weibel, *Applied Physics Letters* **40**, 178 (1982).
- [3] L. E. Van De Leemput and H. Van Kempen, *Reports on Progress in Physics* **55**, 1165 (1992).
- [4] G. Binnig, C. F. Quate, and C. Gerber, *Physical Review Letters* **56** (1986).
- [5] W. Bragg and W. Bragg, *Proc. R. Soc. Lond. A* **88** (1913).
- [6] K. Besocke, *Surface Science* **181** (1987).
- [7] H. Zhang, S. Y. Zhang, Z. J. Chen, and L. Fan, *IEEE Transactions on Ultrasonics, Ferroelectrics, and Frequency Control* **57**, 1140 (2010).
- [8] S. Behler, M. K. Rose, D. F. Ogletree, and M. Salmeron, *Review of Scientific Instruments* **68**, 124 (1997).
- [9] J. A. Stroscio and W. J. Kaiser, editors, *Scanning Tunneling Microscopy* (Academic Press Limited, London, 1994).
- [10] D. R. Lide, editor, *CRC Handbook of Chemistry and Physics, Internet Version 2005*, 90 ed. (CRC Press, Boca Raton, FL, 2005).
- [11] J. Bardeen, *Physical Review Letters* **18** (1967).

- [12] S. Heinze, S. Blügel, R. Pascal, M. Mode, and R. Wiesendanger, *Physical Review B - Condensed Matter and Materials Physics* **58**, 16432 (1998).
- [13] S. Heinze, R. Abt, S. Blügel, G. Gilarowski, and H. Niehus, *Physical Review Letters* **83**, 4808 (1999).
- [14] J. Tersoff and D. R. Hamann, *Physical Review B* **31**, 59 (1985).
- [15] B. J. Albers *et al.*, *Review of Scientific Instruments* **79**, 033704 (2008).
- [16] N. Koch, N. Ueno, and A. T. Wee, editors, *The Molecule-Metal interface* (Wiley, 2012).
- [17] L. Gross *et al.*, *Science* **325**, 1110 (2009).
- [18] F. Mohn, B. Schuler, L. Gross, and G. Meyer, *Applied Physics Letters* **073109**, 1 (2013).
- [19] A. Sweetman, J. Stirling, S. P. Jarvis, P. Rahe, and P. Moriarty, *Physical Review B* **94**, 1 (2016).
- [20] C. Edelmann, *Vakuumphysik* (Spektrum Akademischer Verlag, 1988).
- [21] M. Prutton, *Introduction to Surface Physics* (Oxford University Press Inc., 1994).
- [22] B. S. Salmons, D. R. Katz, and M. L. Trawick, *Ultramicroscopy* **110**, 339 (2010).
- [23] B. O'Regan and M. Grätzel, *Nature* **353**, 737 (1991).
- [24] M. Grätzel, *Nature* **414** (2001), 5.
- [25] M. Grätzel, *Journal of Photochemistry and Photobiology A: Chemistry* **164**, 3 (2004).

- [26] M. Weston, *Adsorption and charge transfer dynamics of photovoltaic and photocatalytic dye-sensitizers*, PhD thesis, University of Nottingham, 2014.
- [27] J. E. House and K. A. House, *Descriptive Inorganic Chemistry*, 2nd ed. (Elsevier, 2010).
- [28] P. Persson and S. Lunell, *Solar Energy Materials and Solar Cells* **63**, 139 (2000).
- [29] J. J. Concepcion *et al.*, *Accounts of Chemical Research* **42**, 1954 (2009).
- [30] M. Weston, A. J. Britton, and J. N. O'Shea, *Journal of Chemical Physics* **134**, 054705 (2011).
- [31] M. Weston, K. Handrup, T. J. Reade, N. R. Champness, and J. N. O'Shea, *The Journal of chemical physics* **137**, 224706 (2012).
- [32] F. Hanke and J. Björk, *Physical Review B* **87**, 235422 (2013).
- [33] N. Takeuchi, C. T. Chan, and K. M. Ho, *Physical Review B* **43**, 14363 (1991).
- [34] J. B. Taylor *et al.*, *Journal of Chemical Physics* **127**, 134707 (2007).
- [35] L. Bartels, G. Meyer, and K.-H. Rieder, *Applied Physics Letters* **71**, 213 (1997).
- [36] S. P. Jarvis, *International Journal of Molecular Sciences* **16**, 19936 (2015).
- [37] M. E. J. Newman and G. T. Barkema, *Monte Carlo Methods in Statistical Physics*, 4th ed. (Oxford University Press Inc., 2004).
- [38] E. Ising, *Zeitschrift für Physik* **31**, 253258 (1925).
- [39] A. D. Stannard, *Pattern Formation in Nanostructured Systems*, PhD thesis, University of Nottingham, 2009.

- [40] A. Stannard, M. O. Blunt, P. H. Beton, and J. P. Garrahan, *Physical Review E - Statistical, Nonlinear, and Soft Matter Physics* **82**, 1 (2010), 1004.3127.
- [41] P. Hapala *et al.*, *Physical Review B* **90**, 085421 (2014), arXiv:1406.3562v1.
- [42] J. E. Sader and S. P. Jarvis, *Applied Physics Letters* **84**, 1801 (2004).
- [43] P. A. Kollman and L. C. Allen, *Chemical Reviews* **72**, 283 (1972).
- [44] T. S. Moore and T. F. Winmill, *J. Chem. Soc.* **101**, 1635 (1912).
- [45] L. Pauling, *The Nature of the Chemical Bond*, 3rd ed. (Oxford University Press Inc., 1960).
- [46] Z.-T. Li and L.-Z. Wu, *Hydrogen Bonded Supramolecular Structures* (Springer-Verlag Berlin Heidelberg New York, 2015).
- [47] J. W. Steed and J. L. Atwood, *Supramolecular Chemistry*, 2nd ed. (Wiley, 2009).
- [48] S. Griessl, M. Lackinger, M. Edelwirth, M. Hietschold, and W. M. Heckl, *Single Molecules* **3**, 25 (2002).
- [49] H. Zhou *et al.*, *Journal of the American Chemical Society* **129**, 13774 (2007).
- [50] A. G. Slater, P. H. Beton, and N. R. Champness, *Chemical Science* **2**, 1440 (2011).
- [51] M. O. Blunt *et al.*, *Chemical Communications* **20**, 2304 (2008).
- [52] M. O. Blunt *et al.*, *Science* **322**, 1077 (2008).
- [53] J. Zhang *et al.*, *Science* **342**, 611 (2013).
- [54] A. M. Sweetman *et al.*, *Nature Communications* **5**, 3931 (2014).
- [55] S. K. Hämmäläinen *et al.*, *Physical Review Letters* **113**, 1 (2014), 1410.1933.

- [56] J. B. Taylor, L. C. Mayor, J. C. Swarbrick, J. N. O'Shea, and J. Schnadt, *Journal of Physical Chemistry C* **111**, 16646 (2007).
- [57] J. N. O'Shea *et al.*, *Surface Science* **486**, 157 (2001).
- [58] R. Raval, *Chem. Soc. Rev.* **38**, 707 (2009).
- [59] N. Chen, Q; Frankel D.J.; Richardson, *Chem. Soc. Rev.* **497**, 37 (2002).
- [60] I. Goodfellow, Y. Bengio, and A. Courville, *Deep Learning* (MIT Press, 2016).
- [61] M. G. Walter *et al.*, *Chemical Reviews* **110**, 6446 (2010).
- [62] C. A. Grimes, O. K. Varghese, and S. Ranjan, *Light, Water, Hydrogen* (Springer, 2008).
- [63] A. Fujishima and K. Honda, *Nature* **238**, 37 (1972).
- [64] M. K. Nazeeruddin, E. Baranoff, and M. Grätzel, *Solar Energy* **85**, 1172 (2011).
- [65] D. R. Weinberg *et al.*, *Chem Rev.* **107**, 5004 (2007).
- [66] M. H. V. Huynh and T. J. Meyer, *Chemical Reviews* **107**, 5004 (2007).
- [67] F. Liu *et al.*, *Inorganic Chemistry* **47**, 1727 (2008).
- [68] T. J. Meyer and M. H. V. Huynh, *Inorganic Chemistry* **42**, 8140 (2003).

List of Figures

2.1	An illustration of a piezoelectric material and its specific deformation under an applied bias voltage.	6
2.2	The schematic design of a tube scanning unit. (a) Shows cross-section of the unit with its labelled sectors. (b) Shows the use of an applied bias to manipulate the shape of the tube in order to control imaging.	6
2.3	Three graphs showing the path of a hypothetical tip in a given scan direction. (a) Shows the fast scan direction and the progression back and forth over time. (b) Shows the same idea in the slow scan direction. These graphs are placed together for contrast. (c) Shows the progression of the tip over a hypothetical area, showing the path taken by the tip.	8
2.4	A schematic of the Besocke microscope design. (a) A side view of the tripod. The tip extends down from the upper plate and can be approached to the sample in the middle. (b) Shows the design of the plate, to which the tip is attached. The supported plate also shows the helical ramps in each sector to allow the tip to be approached or retracted with respect to the sample. (c) Shows a plan view of the Besocke design, highlighting the motion of the legs	10

2.5	A one dimensional analogue of the potential barrier of a vacuum, E_{vac} , separating a sample and tip. The red line represents the wave function of an electron incident from the left tunnelling from the tip to the sample.	11
2.6	An illustration of the different energy levels that result from the application of a bias voltage between the tip and the sample. E_F^T is the Fermi level of the tip and E_F^S is the Fermi level of the sample. 12	
2.7	An image of low voltage atomic resolution scan of a metal, adapted from [15] along with its caption: STM image (raw data) of Cu(111) ($I = 50$ pA, $V = +100$ mV, $T = 5$ K, scan speed of 13 nm/s, image size: 13×13 nm ²). An electronic surface charge wave, caused by a step edge located just outside the scanned area next to the upper left corner, runs diagonally from upper left to lower right. The arrows on the left indicate the position and orientation of the individual wave fronts. [15]	18
2.8	A plot of the Lennard-Jones potential showing the potential well, depth E_0 , set at equilibrium position, r_0	22
2.9	A graph of the relationship of the oscillation amplitude as a function of the driving frequency as given in Equation 2.41. A peak is shown as the driving frequency reaches the natural oscillation frequency of the system, that is, the point of resonance. In this graph, k represents an arbitrary constant.	24
2.10	A comparison of an STM scan taken (a) before picking up a CO molecule on the tip apex, and (b) after picking up a CO molecule, $V = 3$ V, $I = 50$ pA, 7×7 nm ²	27
2.11	An image of the Omicron VT system at the University of Nottingham	29
2.12	An image of the Omicron LT system at the University of Nottingham	30
2.13	An image of the Createc LT system at the University of Nottingham	30

2.14	Photograph of the scan head including the copper fins	32
2.15	A graph showing the relationship of the mean free path of a gas molecule in relation to pressure.	34
2.16	A close up of an etched STM tip with the characteristic tapered apex.	37
2.17	An STM scan of Ag(100) showing creep at the top of the image. .	38
2.18	Common tip artefacts in SPM. (a) Shows a blunt tip with large blurred features present throughout the scan. These features can be produced from relatively fine features on the scanned surface and subtle detail can be lost. (b) shows a surface with a tip double where surface features reproduced twice. This image also highlights the key feature of a tip double that each feature appears as two features separated by exactly the same separation distance and angle.	41
2.19	STM scans showing the process of a sputter anneal cycle. (a) An example of a sputtered surface of Ag(100). The surface shows a set of crater-like structures where silver has been bombarded by incident argon atoms. (b) An example of the same Ag(100) surface following an anneal. The surface shows a number of step edges but the terrace structure is much larger on this surface. . .	44
3.1	Graphs showing efficiencies of absorption on a TiO ₂ surface with and without dye adsorption. 3.1a shows the modification in efficiency against wavelength of light of an untreated surface, ‘A’, versus one with an adsorbed dye ‘B’. 3.1b shows a similar result using different dye complexes, discussed in section 3.1.2.	46
3.2	The N3 molecule, known formally as cis-bis(isothiocyanato)bis(2,2'-bipyridyl-4,4'-dicarboxylato)-ruthenium(II).	48
3.3	The “Black” dye developed by the Grätzel group. In this image, TBA refers to a tetrabutylammonium cation.	49

3.4	A multi-centre dye complex containing the labelled charge transfer centre and reaction centre.	51
3.5	The bi-isonicotinic acid ligand.	51
3.6	a is the previously referenced N3 molecule with b (Ru 455) and c (Ru 470) being based on similar structures [30].	52
3.7	Monolayer and Multilayer spectroscopy with the WSC and CISC molecules taken from Weston et al. [31].	54
3.8	The bulk structure of an unreconstructed gold crystal cut in the (111) plane.	55
3.9	Model showing the bulk gold structure in filled gold circles. The overlaid surface atoms are white circles highlighted in red. The blue bar at the top highlights the 22 bulk atoms and the compressed 23 surface atoms that align along this length.	56
3.10	The atomic arrangement of the (100) cut of silver.	56
3.11	The two orientations of bi-isonicotinic acid; the trans form is shown on the left and the cis form on the right. Here, the grey atoms represent carbon, the red are oxygen, the blue are nitrogen and the white are hydrogen.	57
3.12	Image taken directly from [17]. STM and AFM imaging of pentacene on Cu(111). (A) Ball-and-stick model of the pentacene molecule. (B) Constant-current STM and (C and D) constant-height AFM images of pentacene acquired with a CO-modified tip.	58
3.13	The formulation of a triangular lattice by dividing (a) a square lattice into (b) two triangular sections and (c) skewing the lattice.	61
3.14	The different orientations of molecules with the associated label in the up-facing triangle. Orientation of rhombus is defined by a number.	62

3.15	A matrix of different states and its interpretation into the tiling model.	62
3.16	Illustration of possible relative sizes of probabilities of states, also remarking that all probabilities sum to 1.	64
3.17	An image illustrating the model used for simulations. This image is taken directly from Hapala et al. [41]	65
4.1	A simplified illustration of a hydrogen bond showing the three atoms involved in a hydrogen bond. The red atom is covalently bonded to a hydrogen atom, coloured in white. The hydrogen atom displays a slight positive charge, $\delta+$, which is attracted to the electronegative, $\delta-$, presence of the lone valence pair of the blue atom,	68
4.2	A double hydrogen bond, illustrated in blue, formed between two carboxyl groups.	69
4.3	Representations on observations of Griessl et al. of the assemblies formed by TMA on graphite. (a) Is the TMA molecule with carbon atoms in grey, oxygen in red and hydrogen in white. (b) and (c) show arrangements that the molecule make due to hydrogen bonding.	70
4.4	The STM images of the two different arrangements of TMA deposited on graphite. Taken directly from Griessl et al. [48].	71
4.5	An additional TMA molecule confined through hydrogen bonding within the regular ring structure of the TMA assembly.	71
4.6	The STM images of the host-guest situation. Taken directly from Griessl et al. [48].	71
4.7	The isophthalic acid group with carbon atoms in grey, oxygen in red and hydrogen in white.	72

4.8	Arrangements of tetracarboxylic acid tectons. (a) The structural model. (b) The parallel arrangement. (c) The non-parallel, Kagomé-like arrangement.	73
4.9	Tetracarboxylic acid tectons as labelled by Slater et al. The image adapted directly from work by Slater et al. [50].	74
4.10	An image illustrating the arrangements of molecular junctions. (a) The interpretation of junctions in a triangular lattice. (b) The possible configurations of complete junctions. (c) The key dimensions that define the possible molecular arrangements, d_1 is the distance across carboxyl groups and d_2 is the length of the backbone of the molecule. (d) and (e) The comparison between a stable and unstable formation of arrangements 4 and 5 that depend on the relative lengths d_1 and d_2	75
4.11	Molecules of study under NC-AFM. (a) The 8-hq molecule. (b) The NTCDI molecule. Both molecules are coloured with carbon atoms in grey, oxygen in red, nitrogen in blue and hydrogen in white.	77
4.12	Images taken directly from work by Sweetman et al. [54] showing hydrogen bonded NTCDI molecules imaged with NC-AFM. Left is the raw AFM scan and right is a colourised version of the scan with the molecular structure overlaid.	77
4.13	A molecule of BPPA with carbon atoms in grey, nitrogen in blue and hydrogen in white.	78
5.1	Clean Au(111) on mica, $30 \times 30\text{nm}^2$, $V = -50\text{mV}$, $I = 2\text{pA}$, shown here to highlight the herringbone pattern that exists on the bare gold surface. Imaged on the Omicron LT system.	81
5.2	A K-cell deposition source.	82

5.3	Islands of the bi-isonicotinic acid on the Au(111) surface, $150 \times 150\text{nm}^2$ original scan, which has been cropped due to a tip instability. $V = 1.5\text{V}$, $I = 10\text{pA}$	83
5.4	Low Temperature image of bi-isonicotinic acid on Au(111), $50 \times 50\text{nm}^2$, $V = -0.5\text{V}$, $I = 10\text{pA}$	85
5.5	Localised areas obtained from taking localised scans, initially determined from the overview scan as given in Figure 5.4.	86
5.6	An modified view of Figure 5.5d with individual molecules highlighted. The blue molecules are inferred to be in the trans configuration while those in green are inferred to be in the cis configuration.	87
5.7	A diagram of all possible transformations of a molecule with unrestricted motion.	88
5.8	A further analysis of Figures 5.5 and 5.6, highlighting the suggested hydrogen bond relationship between molecules. Carboxyl to carboxyl bonds are coloured blue and carboxyl to nitrogen bonds are coloured magenta.	90
5.9	A molecular view of the highlighted bonds. (a) shows the carboxyl to carboxyl bond. (b) shows a carboxyl to nitrogen bond.	90
5.10	Two close scans of bi-isonicotinic acid on Au(111) showing a size comparison between the features in (a) STM and (b) NC AFM. (c) Shows the molecular structure of the bi-isonicotinic acid molecule for comparison. Left: the trans conformer. Right: the cis conformer.	92
5.11	(a) and (b) are two NC-AFM scans at $2.5 \times 2.5\text{nm}^2$ taken at a greater and closer separation respectively. (c) Shows the bi-isonicotinic acid molecule superimposed onto a scan. The blue colouration of the scan has been chosen provide a better contrast between the scan and the molecule.	93

5.12	A set of $2.5 \times 2.5\text{nm}^2$ scans of bi-isonicotinic acid molecules of opposite chirality. (a) Is an STM scan of the area, (b)–(d) are NC-AFM scans of the same local area. (e) is an NC-AFM scan that focusses on the proximity of two carboxyl groups.	94
5.13	Four NC-AFM scans, $1.4 \times 1.4\text{nm}^2$ of a carboxyl-carboxyl junction in a bi-isonicotinic acid network. (a) – (d) shows a sequential reduction in tip-sample separation.	95
5.14	$100 \times 100\text{nm}^2$, $V = -0.5\text{V}$, $I = 10\text{pA}$	97
5.15	Two images focussing on local areas of interest from Figure 5.14. $8 \times 8\text{nm}^2$, $V = -0.5\text{V}$, $I = 10\text{pA}$	98
5.16	A collection of AFM scans taken in descending vertical height slices to better understand the bonding structure of the molecules. $5 \times 2.5\text{nm}^2$	100
5.17	An NC-AFM scan with the proposed molecular structure overlaid. The green colour is once again to improve visual contrast. $8 \times 2.5\text{nm}^2$	101
5.18	An NC-AFM scan showing the meeting of a step edge network and a typical network, $8 \times 8\text{nm}^2$	102
5.19	A comparison between (left) a simulated NC-AFM image created through the model proposed by Hapala et al., and (right) an experimental NC-AFM image of a typical, aligned network of bi-isonicotinic acid.	103
5.20	An STM scan of bi-isonicotinic acid on a surface of Ag(100), showing a typical regular network. $V = 1.5\text{V}$, $I = 50\text{pA}$, $6 \times 6\text{nm}^2$. . .	104
5.21	Two spectra taken of the tunnel current between the tip and sample when the bias is swept between -1.5 and $+1.5$ V. (a) Shows the current $I(V)$ graph while (b) is its derivative ($\frac{dI}{dV}$)	105
5.22	A scan of the $\frac{dI}{dV}$ signal of a constant height STM scan taken of bi-isonicotinic acid deposited on Ag(100). $V = -1.17\text{V}$, $6 \times 6\text{nm}^2$	106

6.1	An image showing the initial assumptions of a bi-isonicotinic acid tiling model. A comparison of (a) the T1 tecton and (b) the bi-isonicotinic acid molecule showing their similar molecular structures. (c) Shows the overlay of a rhombus on an experimental NC-AFM image.	109
6.2	NC-AFM image of bi-isonicotinic acid molecule with blue lines indicating an offset in alignment between rows of the molecule. . .	111
6.3	A triangular lattice in red is overlaid onto an NC-AFM scan . . .	111
6.4	The proposed molecular model constructed of three rhombi to represent a single bi-isonicotinic acid molecule. A skeletal approximation of the molecule is overlaid for clarity.	112
6.5	Examples of allowed bonding configurations within the simulated networks. (a) Represent a carboxylic to nitrogen hydrogen bond. (b) Represent a carboxylic to carboxylic hydrogen bond.	113
6.6	(a) Shows the representation of a molecule on a triangular lattice, both the skeletal model overlaid on the rhombi, and a representation the key lattice site that defines the position of the molecule. (b) Shows how the key lattice site has six nearest neighbour translation options. (c) Shows the key lattice site highlighted and permitted rotation options available for the molecule.	114
6.7	Unbound final lattice states of concentrations: (a)0.16ML, (b)0.35ML and (c)0.55ML	118
6.8	Phase space maps of different concentrations of molecules showing the number of bonds per molecule N for different values of bond strength, ϵ and temperature, T	120

6.9	A progression of scans at fixed concentration and bond strength but with increasing values of temperature. Each simulated lattice is presented along with its number of bonds per molecule, N . Scans shown are individual results from simulations, whereas the values for N are the statistical average of all final state lattices in the category.	122
6.10	Examples of bound networks from simulation with increasing temperature leading to coarser domains and a higher number of molecules with similarly oriented neighbours.	123
6.11	Phase space maps of different concentrations of molecules showing the preference score, P , for different values of bond strength, ϵ , and temperature, T	124
7.1	An example of a generic neural network structure highlighting the inputs and outputs as the key features and multiple connections of different strengths that are formed within the network.	129
7.2	An illustration of a functionality of a node in a neural network showing a set of inputs, x and a simplified diagram of internal processing resulting in a node's output value, y	131
7.3	An illustration of the flattening of a 2D matrix into a long 1D matrix.	133
7.4	An image taken directly from Goodfellow et al. [60], showing an illustration of a convolution operation between an input and kernel.	135
7.5	An illustration of a max pooling operation conducted on a matrix, taking the maximum value of a group of cells.	135
7.6	A flowchart representing the layers applied within the neural network	141
7.7	Graphs of predicted values of the three simulation parameters against their true values.	142
7.8	A representation of how final state lattices of the different classes appear.	145

7.9	A flowchart representing the layers applied within the neural network.	146
7.10	A confusion matrix showing how the network's predictions of a class correspond with the true class of a final state lattice.	148
B.1	Schematic representation of the DSSC [64].	160
B.2	The three molecules listed in Nazeeruddin et al. [64].	161
B.3	The Blue Dimer molecule.	163
B.4	Water oxidation mechanism for the blue dimer.	164